Title

Optimization of Particle-based Hydrogel Biophysical and Biochemical Properties for Biomedical Applications

Author

Miwa, Hiromi

Publication Date

2022

Peer reviewed|Thesis/dissertation

UNIVERSITY OF CALIFORNIA

Los Angeles

Optimization of Particle-based Hydrogel Biophysical and Biochemical Properties for Biomedical Applications

A dissertation submitted in partial satisfaction of the

requirements for the degree Doctor of Philosophy

in Bioengineering

by

Hiromi Miwa

2022

ABSTRACT OF THE DISSERTATION

Optimization of Particle-based Hydrogel Biophysical and Biochemical Properties for Biomedical Applications

by

Hiromi Miwa

Doctor of Philosophy in Bioengineering

University of California, Los Angeles 2022

Professor Dr. Dino Di Carlo, Chair

Microporous Annealed Particle (MAP) biomaterials provide a solid, 3-D matrix with interconnected microporous networks that facilitate cellular growth and network formation both in vitro and in vivo. Lattices of MAP gel building blocks are annealed to one another via surface functionalities to form an interconnected microporous scaffold either with or without cells present in the interconnected pores. These microgels are now being explored for various biomedical applications, including accelerated wound healing in vivo and drug delivery. Overall, their injectability, modular design, and porosity make them superior to conventional bulk hydrogels.

The potential of the MAP gel platform is not limited to previous applications in wound healing and cell delivery and new applications will require fine-tuning of physical and

biochemical properties of the building blocks. Unfortunately, a minimal amount of research has been conducted on how the biophysical, such as stiffness, and biochemical properties of MAP gels affects the cellular response. We hypothesized that optimized MAP gel platforms would be ideal for vaccines, primary neural cell culture 3D models, and spinal cord injury treatments and tested multiple formulations of MAP gels to modulate different biophysical and biochemical properties (such as stiffness or loading with bioactive cues) to achieve superior performance addressing the vast biomedical application landscape.

Here we reported multiple new applications of the MAP gel platform; 1) MAP gel for translational primary peripheral sensory neuron culture model for investigation of mechanism for neuromodulation-based diabetes treatment, 2) MAP gel for delivery of antigen and modulation of local immune cells by changing the biophysical properties to enhance strong humoral immunity and 3) Hyaluronic acid-based MAP gels for anti-inflammatory effects to treat spinal cord injury. Also, we project the future direction of our on-going projects to get better insight of mechanism of MAP gel function in wound healing and to establish better formulations for human clinical applications.

The dissertation of Hiromi Miwa is approved.

Aaron Meyer

Stephanie Seidlits

Song Li

Dino Di Carlo, Committee Chair

University of California Los Angeles

2022

DEDICATION

This work is dedicated to all the friends and family who have supported me along this long and arduous journey. Most notably, I would like to acknowledge my parents, Mitsuo Miwa and Yumi Miwa. From a young age you taught me to be curious, to embrace new adventures, and to put my best effort into everything that I do. Your constant love and support help me to push myself past my comfort zone every day. Without you I would not have been able to finish this work. Also, I got tremendous support from Jo Haruna as my life partner whole my Ph.D. period. I must say that I am very lucky to have met you in LA.

The countless hours I spent inside the lab in my Ph.D. period would not have been bearable without all of the close friends I made along the way. Each and every member of the Di Carlo lab family has shaped my graduate school experience in a positive way. Through your friendship, and in some cases mentorship, I have learned to become a better researcher and a better person.

Finally, I must acknowledge the tremendous support of my advisor Dr. Dino Di Carlo. I have always been impressed by your abilities as an innovator and as a scientific storyteller. This 5-year period at Dino's lab is one of the best moments of my life. Thank you for taking a chance on me and for helping me reach the finish line. You were a great mentor who I hope will turn into a great friend in the future.

TABLE OF CONTENTS

TABLE OF FIGURES

ACKNOWLEDGMENTS

Chapter 2 is adapted from: V Cotero, H Miwa, J Graf, et.al., (2019). Peripheral Focused Ultrasound Neuromodulations (pFUS), 2020 Jul 15;341:108721 and V Cotero, J Graf, H Miwa et.al., 2022 Nature Biomedical Engineering, 6, 683–705. VC and JG performed animal experiments.

Chapter 3 is adapted from: H Miwa and O Antao et.al., (in submission). Development of VaxMAP platform for prevention of influenza virus infection by effective activation of immune cells. OA performed ELISA, flow assay and influenza challenge experiments.

Chapter 4 is adapted from: J Karam and H Miwa et.al., (in preparation). Micro porous hyaluronic acid-based biomaterial induced macrophage polarization for spinal cord injury treatment. JK performed all in vitro and animal experiments.

Chapter 5 is adapted from: S Butenko, H Miwa et.al., (2022). Engineering immunomodulatory biomaterials to drive skin wounds toward regenerative healing, Cold Spring Harbor perspectives in biology, a041242.

VITA

EDUCATION

B.S. in Chemical Engineering (2017), Keio University, Japan

RESEARCH APPOINTMENTS

Graduate Student Researcher (2017-2022), University of California, Los Angeles

Professor Dino Di Carlo, Department of Bioengineering

PUBLICATIONS

- C Murray, **H Miwa**, M Dhar, D Park, E Pao, J Martinez, S Kaanumale, E Loghin, J Graf, K Rhaddassi, W Kwok, D Hafler, C Puleo, D Di Carlo, Unsupervised capture and profiling of rare immune cells using multi-directional magnetic ratcheting, ***Lab on a Chip***, 18 (16), 2396-2409
- A. Isozaki, Y. Nakagawa, M. H. Loo, Y. Shibata, N. Tanaka, D. L. Setyaningrum, JW Park, Y. Shirasaki, H. Mikami, D. Huang, H. Tsoi, C. Riche, T. Ota, **H. Miwa**, Y. Kanda, T. Ito, K. Yamada, O. Iwata, K. Suzuki, S. Ohnuki, Y. Ohya, Y. Kato, T. Hasunuma, S. Matsusaka, M. Yamagishi, M. Yazawa, S. Uemura, K. Nagasawa, H. Watarai, D. Di Carlo and K. Goda. Sequentially addressable dielectrophoretic array for high-throughput sorting of large-volume biological compartments, ***Science Advances***, 6 (22), eaba6712
- V Cotero, **H Miwa**, J Graf, J Ashe, D Di Carlo and C Puleo, Peripheral Focused Ultrasound Neuromodulations (pFUS), ***Journal of Neuroscience Methods***, 2020 Jul 15;341:108721
- J Fang, J Koh, Q Fang, H Qiu, M Archang, M Sadrabadi, **H Miwa**, X Zhong, R Sievers, D Gao, R Lee, D Di Carlo, and S Li, Injectable Drug-releasing Microporous Annealed Particle Scaffolds for Treating Myocardial Infarction, ***Advanced Functional Materials***, 30 (43), 2004307
- V Cotero, J Graf, **H Miwa**, Z Hirschstein, K Qanud, T. Huerta, N Tai, Y Ding, K Jimenez-Cowell, J Tomaio, W Song, A Devaragan, T Tsaava, R Madhavan, K Wallace, E Loghin, C

Morton, Y Fan, T Kao, K Akhtar, M Damaraju, L Barenboim, T Maietta, J Ashe, K Tracey, T Coleman, D Carlo, D Shin, S Zanos, S. Chavan, R Herzog, C Puleo, Stimulation of the hepatoportal nerve plexus with focused ultrasound restores glucose homoeostasis in diabetic mice, rats and swine, ***Nature Biomedical Engineering,*** 6, 683–705 (2022)

- **H Miwa**, R Dematteo, R Ghosh, J De Rutte, and D Di Carlo, Single-cell sorting based on secreted products for functionally-defined cell therapies, Accepted, ***Microsystems & Nanoengineering***, 8 (1), 1-18
- S Butenko[#], **H Miwa[#]**, Y Liu, M V. Plikus, P Scumpia, W Liu, Engineering immunomodulatory biomaterials to drive skin wounds toward regenerative healing, Accepted, ***Cold Spring Harbor perspectives in biology,*** a041242 ([#] authors contributed equally)
- Jijun Huang, Josh Lee, Christoph Rau, Arash Pezhouman, **Hiromi Miwa**, Matthew Feldman, Matthew Kong, Ziyue Yang, Ivan Pushkarsky, Kyungsoo Kim, Shan Parikh, Shreya Udani, Chen Gao, Bjorn Knollmann, Reza Ardehali, Dino Di Carlo, Yibin Wang Regulation of postnatal cardiomyocyte maturation by an RNA splicing regulator RBFox1, in revision, ***Circulation***
- **H Miwa**[#], O Antao[#], S Baghdasarian, L Shang, P Scumpia, D Di Carlo, J Weinstain, Development of VaxMAP platform for prevention of influenza virus infection by effective activation of immune cells, in submission, ([#] authors contributed equally)
- J Karam, **H Miwa**, B Singer, D Di Carlo, S Seidlits, Micro porous hyaluronic acid-based biomaterial induced macrophage polarization for spinal cord injury treatment, in preparation.
- R Zheng, V Estrada, **H Miwa**, Y Wang, D Di Carlo, R Conder, Single domain Terfenol D micromagnets for programmable single sorting, in preparation, in preparation

Chapter 1. Introduction: MAP Gel as Promising Tool for Biomedical Applications

1.1. Biophysical and chemical properties of biomaterials

It was in the 1990s that the modern concept of biomaterial-based tissue engineering was introduced. Several biomaterials with tunable biophysical and biochemical properties have been developed since then. Scaffolds used for in situ tissue regeneration include monolithic, microporous, nanoparticles, fibrous, hydrogels, and 3D-printed scaffolds. Polymers, ceramics, metals, and composites can be used to fabricate scaffolds. A synthetic, natural, or a combination of these materials must respond to biological signals and interact with the immune system and endogenous cells. As a result of their biophysical and biochemical properties, these biomaterials can interact with the body, which can alter local tissue microenvironments by modulating the immune system and controlling the kinetics and degree for biomedical applications (Figure 1-1).

Through intracellular and intercellular signaling, a biomaterial's biophysical characteristics, such as stiffness, structure, topography, and degradation, can alter the local tissue microenvironments[1,2]. The matrix stiffness dictates the adhesion, spreading, and fate of cells. Mesenchymal stem cells are directed to osteogenic lineages by stiffer surfaces, while stem cells differentiate into chondrogenic lineages by softer surfaces. The scaffold's porosity determines cellular infiltration as interconnected pore networks facilitate nutrients, oxygen, and waste product transport. Angiogenesis is also facilitated by the porosity of scaffolds. In the same way, topological features, such as patterned surfaces (high surface roughness), can promote or suppress cell adhesion and fate. For tissue regeneration, in situ degradation of biomaterials is desirable. For optimal tissue growth, the degradation rate should match the rate at which the

tissue is generated. Collagen or gelatin, for example, can be degraded using cell enzymes for scaffold remodeling and the deposition of new tissue. As a result of the degradation of biomaterials, the newly formed tissue should be able to sustain load transfer due to its mechanical stiffness. Finally, if the biophysical characteristics of the biomaterial are incompatible with those of the tissue, suboptimal healing may lead to poor functionality of regenerated tissue, tissue loss, and implant loosening. The biophysical properties of biomaterials can be tuned to control cellular fate and modulate the microenvironment in vivo.

An important biochemical characteristic of biomaterials is the release of signaling molecules, such as proteins and small molecules, as well as the degradation and dissolution of the scaffold. There are a number of biochemical cues that can be used to activate specific signaling pathways or a set of genes in order to direct and control cellular activity. It has been shown that the release of signaling factors from responsive biomaterials can trigger the activation of cell-receptor proteins, which control a variety of processes within the cell, including transporting proteins into the cell, morphology, and other signaling pathways. As an example, biomaterials can stimulate angiogenesis in vivo[3] by sequestering proangiogenic growth factors within scaffolds[4,5]. Unlike exogenous (unbound) delivery of growth factors, sequential attachment of these signaling molecules to biomaterials can result in sustained activation of cell-surface receptors and subsequent downstream signaling. In addition to releasing signaling ions, biomaterial degradation may also alter the local microenvironment. Calcium, for instance, triggers calcium-sensing receptors, which are important for cell proliferation, differentiation, and chemotaxis[6]. Further, calcium-phosphate-based biomaterials can release ions which can stimulate the differentiation of endogenous cells into bone-forming cells[7,8]. Overall, sequestering

growth factors from biomaterials or releasing mineral ions from them may alter the tissue microenvironment.

It is important to consider and optimize the biophysical and biochemical characteristics of biomaterials for the intended application. A cartilage regeneration procedure requires endogenous cells to assume a round shape, whereas a bone regeneration process requires biomaterials to facilitate cell adhesion and cells to assume a spindle shape. In the same way, angiogenesis is preferred when regenerating vascularized tissues or organs, such as the heart, muscle, kidney, liver, and lung, but it should be suppressed when regenerating avascular tissues, such as cartilage and cornea. Additionally, it is important to take into account the availability of endogenous stem cells and progenitor cells in specific tissue types, which can impact the regenerative process. Consequently, the biomaterial should possess biophysical and biochemical characteristics that target the tissue microenvironment.

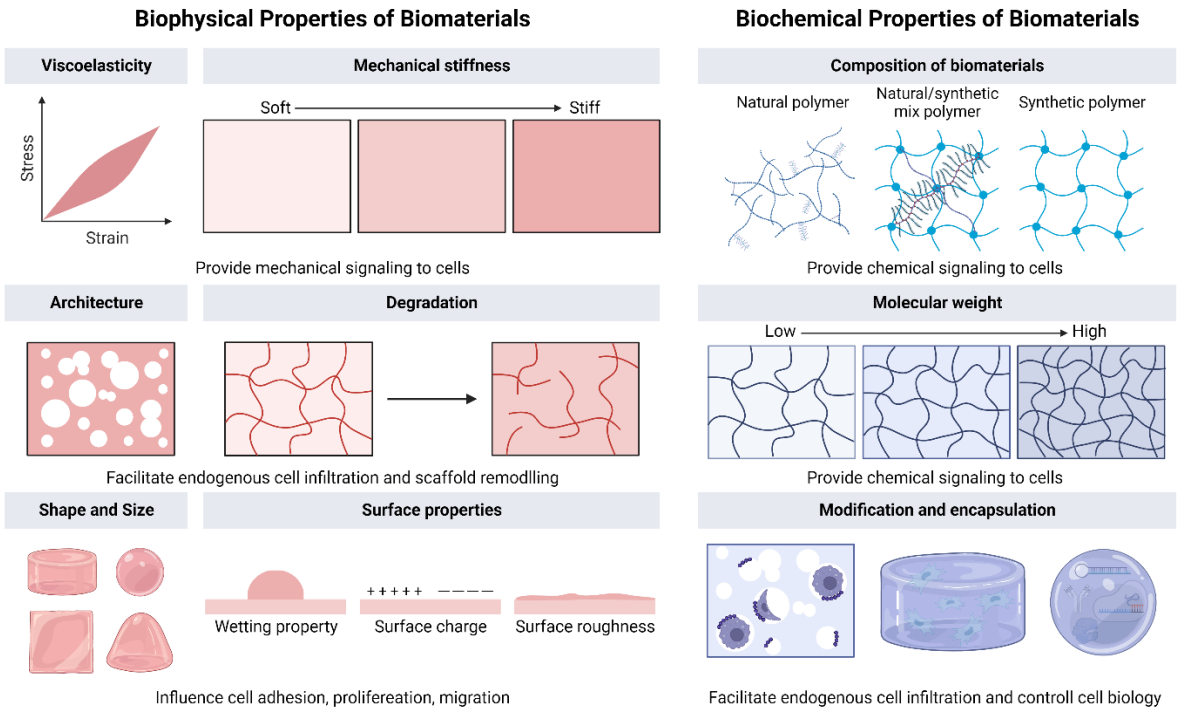

Figure 1-1 Approaches to engineer biomaterials for biomedical applications.
A range of biomaterial has been developed to harnesses the innate regenerative capacity of the body. The characteristics of these biomaterials can be classified as either biophysical or biochemical. Both these characteristics function in synergy to facilitate tissue healing. Biophysical characteristics include bulk properties such as viscoelasticity, stiffness, architecture and degradation, as well as surface properties such as guidance cues, shape and size of nanomaterials, roughness, charge and wetting characteristics of biomaterials. These biophysical characteristics can control a range of cellular functions, including adhesion, migration, proliferation and differentiation. Biochemical characteristics include the chemical structure of biomaterials, as well as the presence of signaling biomolecules, such as proteins, minerals, small-molecule drugs.

1.2. Limitation of existing biomaterials

Traditionally, hydrogels are crosslinked into continuous volumes (bulk hydrogels) with external dimensions of several millimeters or greater and a mesh size of several nanometers to allow molecules to diffuse freely. Although many biophysical and biochemical properties of bulk hydrogels have already been optimized, they are not always suitable for their intended applications, especially when injection is needed. Preformed bulk hydrogels are challenging to

deliver using minimally invasive techniques and must be shaped and implanted, often involving surgical incisions. Usually, bulk hydrogels can only be injected as homogeneous precursor solutions with liquid-like (viscous) rheological properties before gelation must be induced through in situ crosslinking or shear-thinning methods. While hydrogel particles that possess unique functional properties that do not present in bulk hydrogels. For example, hydrogel particle suspensions can be easily delivered through small needles or inhalers for minimally invasive cell and biologic delivery. Hydrogels particle scaffolds that open up new building approaches, including microporosity and scaffold modularity[9–12].

1.3. MAP gel platform as readily tunable biomaterial platform

Past years, we developed microporous annealed particle (MAP) gels as promising biomaterial for biomedical applications, ranging from the therapeutic delivery of cells and drugs to the production of scaffolds with their tunable features. Biologics (cells and drugs) can be encapsulated into MAP gels of predefined shapes and sizes using a variety of fabrication techniques (Figure 1-2). MAP gels can be formulated in suspensions to deliver therapeutics, as aggregates of particles (granular hydrogels) to form microporous scaffolds that promote cell infiltration or embedded within a bulk hydrogel to obtain multiscale behaviors. MAP gels suspensions can be injected for minimally invasive manner. The properties of MAP gels make them promise for numerous biomedical applications, several of which are covered in this section, including cell delivery, drug delivery, scaffold building and translational 3D culture model. To expand the application landscape of MAP gel, further investigation and optimization is needed of both biophysical and biochemical properties for specific applications. My work addresses multiple applications of the MAP gel platform from a clinically translational 3D model for

neuron culture to a vaccination platform. We also aim to further development of MAP gel platform for wound healing and spinal cord injury treatment.

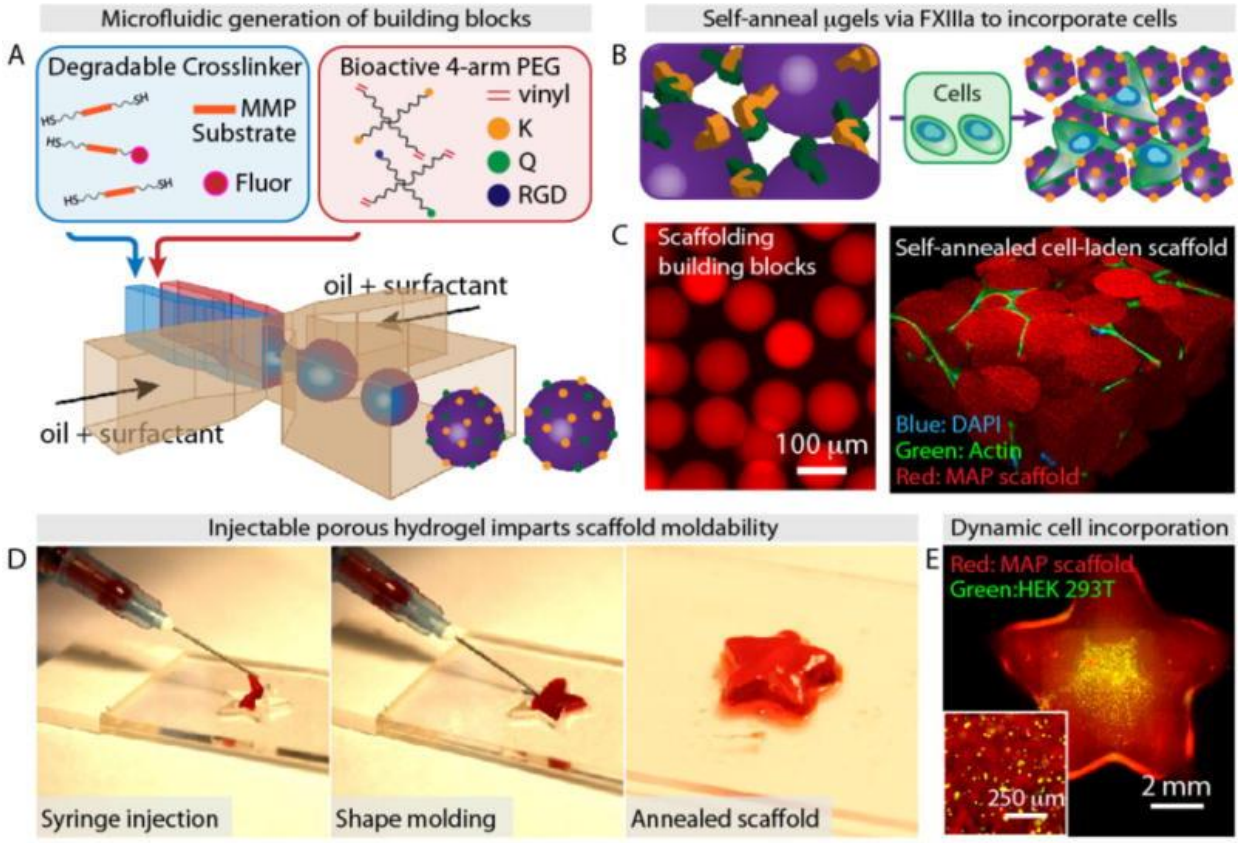

Figure 1-2 Microfluidic generation of microsphere hydrogel building blocks for the creation of Microporous Annealed Particle (MAP) scaffolds.
A–B: Scheme illustrating MAP gel formation using a microfluidic water-in-oil emulsion system. A pre-gel and crosslinker solution are segmented into monodisperse droplets followed by in-droplet mixing and crosslinking via Michael-addition. MAP gels are purified into an aqueous solution and annealed using FXIIIa into a microporous scaffold, either in the presence of cells or as a pure scaffold. C: Fluorescent images showing purified MAP gel building blocks and a subsequent cell-laden MAP scaffold. D–E: MAP scaffolds are moldable to macro-scale shapes and can be injected to form complex shapes that are maintained after annealing. A process that can be performed in the presence of live cells. Figure is adapted from the reference[10]

Chapter 2. Hydrogel based 3D in-vitro Culture System for Characterization of Peripheral Focused Ultrasound Neuromodulation (pFUS)

A fundamental limit to the study of the peripheral nervous system and its effect on organ function is the lack of tools to selectively target and stimulate specific neurons. Traditional implant and electrode-based systems remain too large and invasive for use at the organ or sub-organ level (without stimulating or effecting neighboring organs and tissues). Recent progress in optical and genetic tools (such as optogenetics) has provided a new level of molecular specificity and selectivity to the neurons that are stimulated by bioelectronic devices. However, the modified neurons that result from use of these tools (that can be selectively activated based on expression of light, heat, or stimuli sensitive ion channels) often still require stimulation by implantable devices and face difficult scientific, technical, and regulatory hurdles for clinical translation. Herein, we present a new tool for selective activation of neuronal pathways using anatomical site-specific, peripheral focused ultrasound neuromodulation (pFUS).

We utilize three experimental models to expand upon and further characterize pFUS beyond data outlined to our initial report[13], and further demonstrate its importance as a new investigative and translational tool. First, we utilized an interconnected microporous gel scaffold to culture isolated dorsal root ganglion (DRG) neurons in an interconnected, three-dimensional in vitro culture[10,14]. Using this system, we directly applied ultrasound (US) stimuli and confirmed US activation of peripheral neurons at pressures consistent with recent in vivo observations[15]. Next, we tested the capability of pFUS to activate previously reported nerve pathways at multiple locations within the neural circuit, including primary sensory ganglia (i.e. inferior ganglion of the vagus nerve), peripheral ganglia (i.e. sacral ganglia), and within target end-organs. In addition, we compared selective activation of multiple anatomically overlapping neural pathways (i.e. activation of the

cholinergic anti-inflammatory pathway[16,17] vs. metabolic sensory pathways[18–20] after stimulation of each separate target site. Finally, we utilized an established model of metabolic dysfunction (the LPS-induced inflammation/hyperglycemia model) to demonstrate pFUS capability to stimulate and assess alternative therapeutic stimulation sites (i.e. liver, pancreas, and intestines) in a simple and clinically relevant manner. This is demonstrated by ultrasound induced attenuation of LPS-induced hyperglycemia by stimulation at all three anatomical targets, and mapping of the effect to a specific molecular product of excitable cell types within each stimulus site. The ease-of-use and non-invasive nature of pFUS provides a solution to many of the challenges facing traditional toolsets, such as implantable electrodes and genetic/optogenetic nerve stimulation strategies. The pFUS tool described herein provides a fundamental technology for the future study and manipulation of the peripheral nervous and neuroendocrine systems.

2.1. Introduction

Every organ in the body is innervated by nerves that either send signals to the organ (and effect that organs function) or sense the current state of the organ (and communicate back to the central nervous system)[21–27]. However, until recently our understanding of those interactions was limited, primarily due to the tools available to accurately stimulate and record from neurons communicating with defined anatomical and functional organ locations[21,23,27,28]. Recently, new optical and genetic tools have provided new ways with which to communicate with and experiment on specific nerve pathways (versus use of traditional electronic implant-based devices)[24,25]. With these new tools has come new understanding of the specific roles that nerves play in both the homeostatic and pathological function of the tissues they innervate.

Bioelectronic medicine (BEM) is an emerging field which leverages medical devices to modulate nerve circuits that are found to control important physiological processes[26,27] . Clinical trials now indicate that these nerve circuits may be targeted and stimulated with therapeutic effect. These include a study in which implant-based vagus nerve stimulation (VNS) demonstrated inhibited production of inflammatory cytokines and a positive effect on rheumatoid arthritis (RA) severity scores[29] . Although performed on a limited number of patients, the study demonstrated both response to the electrical stimulation (via DAS28CRP scores) and worsening of disease severity upon withdrawal of the BEM treatment. Additional data in larger studies will be required to assess full clinical efficacy. These initial findings show for the first time that the molecular target of a major class of pharmaceuticals (i.e. TNF inhibitors or anti-TNFs) may be modulated using a medical device.

However, despite recent successes, these BEM tools still have significant scientific, regulatory, and market hurdles to overcome. And full realization of the promise of bioelectronic medicine may require technologies that activate these nerve pathways using less invasive techniques, while providing an increased level of precision (compared to implants that stimulate many neurons within large nerve bundles). Previously, we demonstrated the first study in which peripheral focused ultrasound neuromodulation (pFUS) is utilized to stimulate sub-organ locations containing specific targeted neurons[13]. Results were shown in two different organ systems, including a splenic target (neurons associated with the cholinergic anti-inflammatory pathway[16,17,30] and a hepatic target (neurons associated with metabolic sensing and control[18–20,31–35]. Herein, we expand this concept by 1) confirming direct pFUS nerve activation by applying ultrasound stimuli to an in vitro three-dimensional (3D) nerve culture[10,14] (Figure 2-1 A), 2) demonstrating pFUS activation of neural pathways at multiple strategic peripheral target

locations (in addition to the end-organ targets shown previously; Figure 2-1 A, and 3) demonstrating pFUS capability to affect a specific pathological state (i.e. LPS-induced hyperglycemia) using multiple associated end-organ stimulation targets (i.e. liver, pancreas, and intestines; Figure 2-2 A.

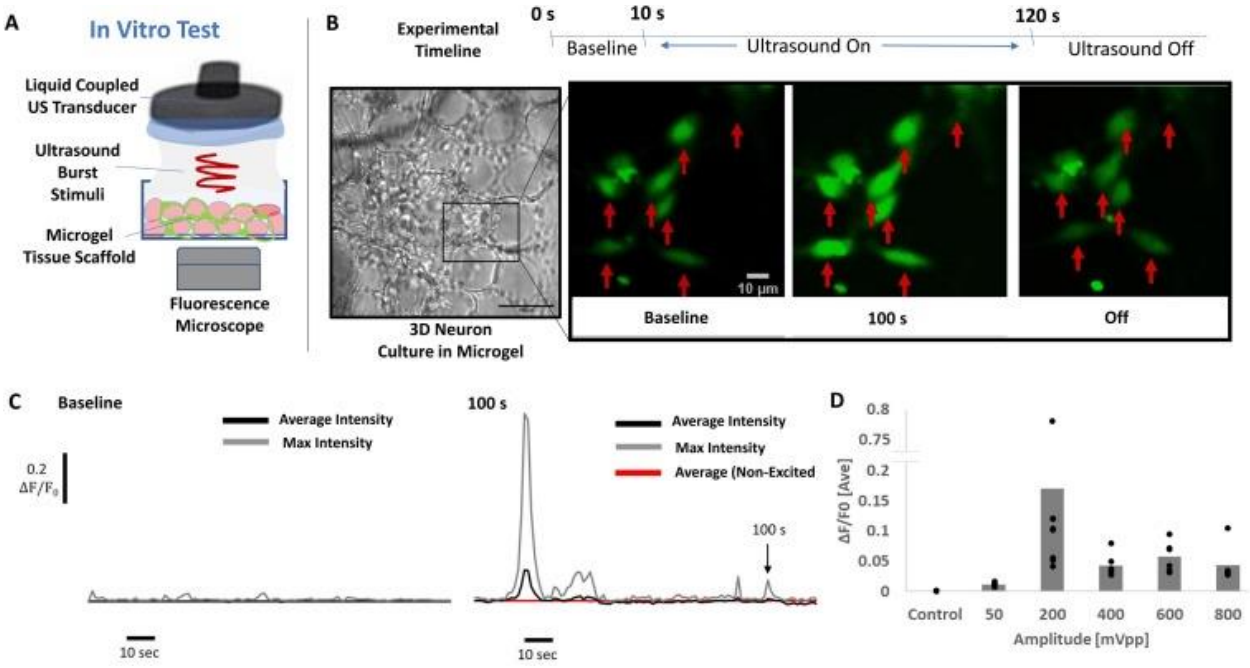

Figure 2-1 A schematic of the 3D in vitro peripheral neuron culture system.
(A) A schematic of the 3D in vitro peripheral neuron culture system. (B) Experimental timeline shown on top of bright field and fluorescence images of DRG neuron cells in 3D hydrogel scaffold. Diameter of hydrogel particles is around 100 µm. DRG neuron cells grow between pores of hydrogel particles three dimensionally. The fluorescence images show a time lapse of calcium (Ca) imaging during pFUS stimulation. pFUS stimulation is on at 10 s from the starting point of observation and turned off again at 120 s. Ultrasound was then turned off for 2 min (allowing post-ultrasound or off images to be taken) prior to re-starting the stimulus. Calcium concentrations of DRG neuron cells were increased after ultrasound firing (as noted by an increase in fluorescence within the imaged neurons). After pFUS simulation, Ca concentration in cells returned to the same level as before stimulation. (C) Data showing average F/F0 value and maximum F/F0 value in each time points for the imaged neurons. F/F0 is unchanged without pFUS stimulation (left). On the other hand, F/F0 is increased during pFUS stimulation (right). (E) Different amplitudes of pFUS were utilized in repeat experiments and 200 mVpp (or 0.83 MPa peak-positive pressure) showed the largest change in fluorescence within the same DRG culture (N > 5 for each group). This corresponds to the same optimal ultrasound pressure for neuromodulation, as shown in previous in vivo studies.

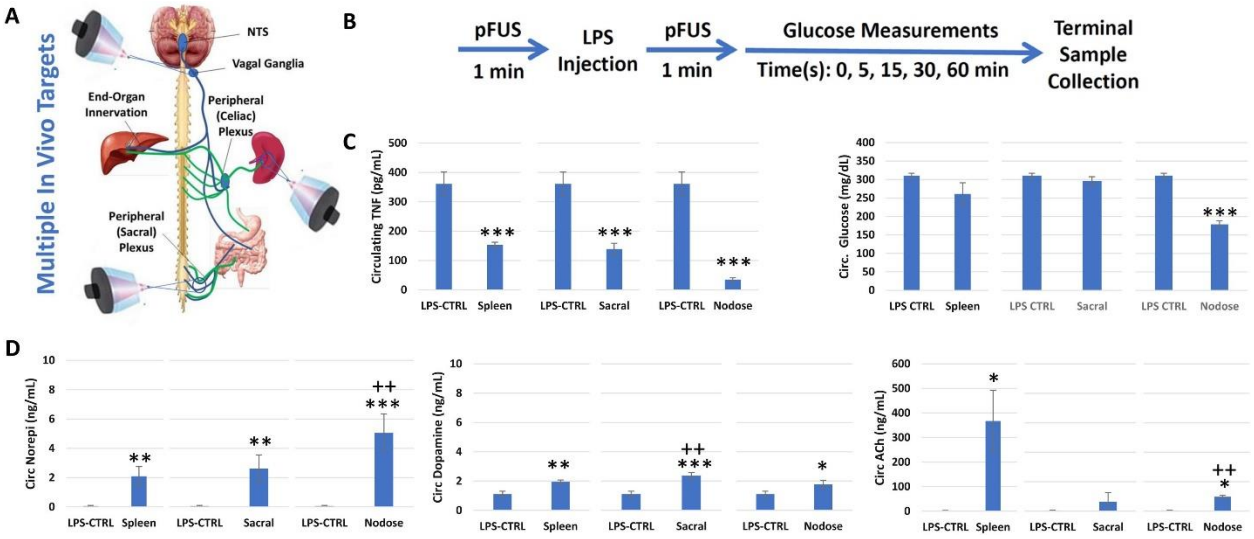

Figure 2-2 A schematic of the 3D in vivo experiments.
(A) A schematic diagram of the use of pFUS to stimulate neurons in both end-organ locations (such as the spleen and liver) and peripheral nerve ganglia (such as the no dose and sacral ganglia). (B) A timeline of the pFUS stimulation and blood sampling performed within the LPS-induced inflammation and hyperglycemia model used throughout this manuscript). (C) Data showing TNF (cytokine) concentrations after pFUS targeted to different anatomical sites within the splenic and enteric cholinergic anti-inflammatory pathway (i.e. spleen, sacral ganglion, and no dose ganglion), compared to LPS alone (i.e. no ultrasound) controls. (D) Data showing blood glucose concentrations after pFUS targeted to the three different anatomical target sites, compared to LPS controls (LPS CTRL). (E) Measures of circulating/blood concentrations of neurotransmitters (i.e. epinephrine, norepinephrine, dopamine, and acetylcholine) after pFUS at the three different anatomical target sites, compared to LPS controls (LPS CTRL). The asterisks mark statistical significance using a one-way ANOVA with follow-up tests that include a Tukey's multiple comparison (using statistical hypothesis testing for previous t-tests). Significance is indicated as *** when $p \leq 0.0005$, indicating a high level of significance compared to LPS-sham controls, ** when $p \leq 0.005$, indicating a moderate level of significance as compared to LPS-Sham controls, or * when $p \leq 0.05$ indicating a minor level of significance as compared to LPS-Sham controls. ++ indicate additional testing with respect to the other stimulation sites (not LPS CTRL). N = 10 for each experimental condition.

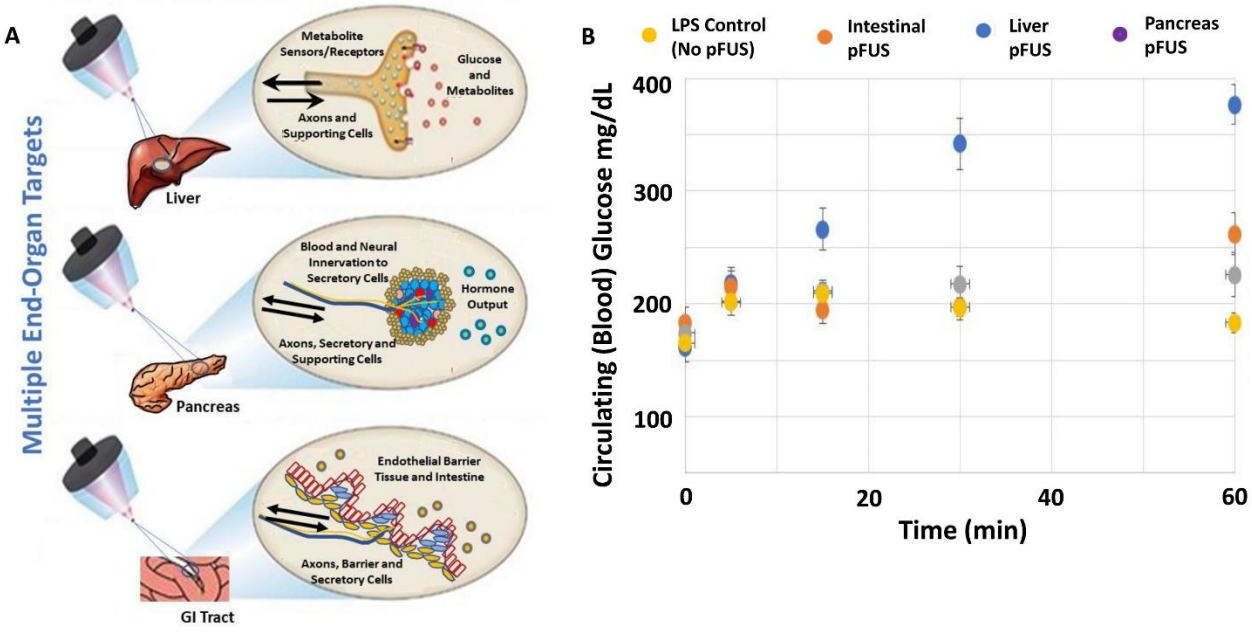

Figure 2-3 Glucose level control with pFUS neuromodulation.
(A) A schematic of pFUS neuromodulation in end-organs, in which innervation points of known axonal or neuroendocrine populations are targeted for stimulation using focused pulsed ultrasound. Targets investigated herein include points of sensory nerve terminals within the liver, the pancreatic tail, and the jejunum area of the small intestine (methods used to locate and target these sites are described in the methods section). (B) Circulating blood glucose concentrations are shown at the 0, 5, 10, 15, 30, and 60-min timepoints for the LPS control (no pFUS, yellow circles), hepatic pFUS (blue circles), pancreatic pFUS (purple circles), and GI pFUS (orange circles) groups. N = 12 for each group.

In our previous report, we demonstrated that sub-organ stimulation of a specific site in the liver (known to harbor glucose and metabolite sensory cells[18–20] modulates systemic metabolism through a hypothalamic pathway[13,34], while stimulation of the spleen (known to harbor neurons that regulate cytokine concentrations in the blood[17,36] modulates inflammation through the cholinergic anti-inflammatory pathway[13]. We demonstrated that these two pathways were stimulated simultaneously when using standard implanted vagus nerve stimulator (VNS) technology, as neurons from both end-organs are stimulated by the implant. However, pFUS enabled separate stimulation of each pathway (i.e. modulation of cytokines/inflammation at the splenic pFUS site without altering blood glucose/metabolism, and modulation of blood glucose

at the liver pFUS site without altering cytokines/inflammation status) (Cotero et al., 2019a). Significant data was obtained suggesting pFUS was acting on these pathways by stimulating neurons within the ultrasound field (including ultrasound-induced neurotransmitter modulation in the spleen, elimination of the splenic effect using reserpine denervation, ultrasound-dependent hypothalamic cFos expression after liver pFUS, and verification of ultrasound-activated afferent nerve pathways using DfMRI)[13]. In addition, two other groups have reported evidence of ultrasound-induced activation of the splenic pathway[37,38]. However, despite this evidence in pre-clinical models, most attempts to directly record action potentials and ultrasound activation in stimulated peripheral nerves have failed in vitro[39–41].

We hypothesized that past challenges in achieving direct measurements of ultrasound-induced peripheral nerve activation can be attributed to the stimulus target. In the recent reports of in vivo ultrasound induced peripheral neuromodulation,[13,37,38] stimulation targets were located directly in end-organs (i.e. neurons, axons, and end-axon terminals within organs). However, in past reports that failed to achieve direct ultrasound-mediated nerve activation, the stimulus target was large myelinated or unmyelinated nerve bundles[39–42]. Further validating this hypothesis are previous ultrasound stimulation studies on central nervous system (i.e. brain tissue) targets that demonstrated successful activation of CNS neurons through an US-induced effect on SNARE-mediated synaptic vesicle exocytosis and synaptic transmission[43,44]. In the PNS these molecular components (i.e. cell soma, SNARE proteins and synaptic connections) are more prevalent in end-organ sites or ganglia (compared to inter-organ nerve/axonal bundles).

Experiments investigating CNS nerve activation often utilize brain-slice experimental preparations, in which excised sections of brain tissue are temporarily maintained at an artificial interface to fluorescence microscopes and electrodes for analysis of nerve activity[43]. However, such experimental in vitro systems for PNS tissue are less common, as peripheral nerves span long lengths in the body and interface with an array of complex tissue types. Typically, PNS experiments have been limited to studying excised axon bundles that have been cut and separated from their soma and synaptic interfaces[39,40,42]. Herein, we first utilize a novel 3D culture system[10,14] (Figure 2-1 A) to provide a more optimal in vitro experimental platform for peripheral nerve investigation compared to traditional excised nerve bundle preparations. We observed formation of complex neural networks within the culture platform and utilized the novel system to couple ultrasound transducers and an observational fluorescence microscope to the neurons. Use of calcium indicator dyes enabled direct observation of neuron activity. Using the system, we verified that the ultrasound pressures used previously for in vivo neuromodulation at end-organs[13,37] results in direct nerve activation in the culture system.

We then expanded in vivo neuromodulation experiments compared to those previously reported by stimulating alternative sites known to contain peripheral nerve soma and synapses, including sensory ganglion (i.e. inferior ganglion of the vagus nerve or no dose ganglion) and peripheral ganglion of mixed (sensory and efferent) innervation (i.e. sacral ganglion). We demonstrate activation of the cholinergic anti-inflammatory pathway[16,17,45] (i.e. modulation in LPS-induced circulating cytokine concentrations after ultrasound stimulation at each site (i.e. end-organ/spleen, no dose, and sacral ganglia) and show that both the magnitude of cytokine reduction and presence of other off-target effects (i.e. simultaneous changes in blood glucose

levels) are stimulation site dependent. Lastly, we show intervention in a specific pathological state (i.e. reduction of LPS-induced hyperglycemia) through stimulation of multiple strategic anatomical locations associated with metabolic control. These exploratory stimulation sites included the hepatic site containing peripheral glucose sensors[13,18–20,34], the pancreas associated with insulin secreting beta cells[46], and an intestinal site containing incretin secreting enteroendocrine cells[47]. We show that ultrasound induced attenuation of hyperglycemia is achieved by stimulation at each of the anatomical targets. However, the magnitude of blood glucose reduction is stimulation site dependent, and the effect is driven by different molecular mechanisms at each site. Together this data demonstrates that ultrasound stimuli are capable of direct peripheral nerve (and other neuroendocrine cell) activation, and that as a new tool pFUS is capable of efficient assessment of the effectiveness of alternative therapeutic BEM stimulation sites.

2.2. Results and Discussion

We transmitted pFUS through columns of liquid culture media (Figure 2-1 A) and the 3D DRG culture[14] described above. DRGs responded well to the 3D culture environment, adhering to the hydrogel microparticle surfaces and projecting neurites into the micropores. Both somal and synaptic nerve features were apparent in the culture, in addition to axonal projections (Figure 2-1 B). Axonal outgrowth resulted in neuron network formation across the micropore gaps formed between the microparticles. By imaging the peripheral neuron networks in media-loaded with Ca2+ indicator (Fluo-4 Direct calcium assay kit) we were able to image Ca transients within regions-of-interest within the culture (Figure 2-1 B). To measure ultrasound-induced changes in Ca-signaling (i.e. ultrasound-induced increases in neural activity) we aligned the ultrasound

transducer (and focal point) to the center of the optical field of view (FOV). Figure 2-1. B and C demonstrates that fluorescence intensity (and thus average Ca concentrations within neurons) across the FOV increased after pulsed ultrasound stimulation (using 1.1 MHz, 136.36 μs pulse length, 0.5 ms pulse repetition period US pulses described previously[13]. The appearance and amplitude of these calcium transients were ultrasound pressure dependent. And, the pressure applied that achieved maximum nerve activation (Figure 2-1. D; 0.83 MPa peak positive pressure or 23 mW/cm2 burst average) corresponded to the optimal pressure shown in both previous in vivo/PNS neuromodulation[13,37,38] and CNS brain slice[43] experiments.

The above in vitro results provide further confirmation that ultrasound stimuli are capable of activating peripheral neurons, in addition to the previous in vivo reports of ultrasound activation of both the splenic cholinergic anti-inflammatory pathway (CAP)[13] and hepatic glucose sensory pathways. We next sought to further explore the potential for pFUS to activate the CAP at multiple locations within the brain-spleen neural pathway. Figure 2-2 A shows a schematic of this strategy, in which pFUS stimuli were focused at multiple locations that contain somal and/or synaptic junctions along the vagal and parasympathetic systems. These include the No Dose ganglion (i.e. location of the soma of a majority of the vagal afferents that project into the brain), the sacral ganglion (i.e. location of mixed sympathetic and parasympathetic soma and synaptic junctions), and the spleen (i.e. locations of CAP specific neurons previously shown activated by pFUS stimuli.

Figure 2-2 B depicts the timeline of in vivo neuromodulation studies performed herein, in which LPS is first introduced to produce an inflammatory and hyperglycemic state (see materials

and methods and previous report for additional details of the LPS protocol). Ultrasound is then applied, and the effect of ultrasound neuromodulation is measured by comparing inflammatory or metabolic markers in the LPS control (i.e. no ultrasound stimulation) versus LPS + ultrasound stimulation cohorts. Figure 2-2 C shows that as described previously[13] splenic neuromodulation and activation of CAP is sufficient to attenuate the LPS response. In addition, as shown previously, the local activation of CAP at the splenic site limits additional (non-CAP or non-target) effects that are typically observed using implant-based VNS CAP activation, such as suppression of LPS-induced hyperglycemia (Figure 2-2 C). pFUS stimulation at both the no dose and sacral ganglion also resulted in attenuated LPS response. In addition, no dose ultrasound neuromodulation attenuated the effects of LPS to a larger extent than stimulation at either the sacral or splenic sites. This agrees with recent studies of the cholinergic anti-inflammatory pathway that have confirmed the importance of vagal afferents in triggering activation of CAP (i.e. neurons entering the CNS through the no dose ganglion), but also expanded the efferent arc of the pathway to include additional vagal and sympathetic neurons[48].

However, despite the increased level of cytokine suppression, stimulation at the no dose ganglion also resulted in suppression of LPS-induced hyperglycemia (Figure 2-2 D). This agrees with previous results using implanted cervical VNS[13,16] in which activation of the entire vagus nerve entering the CNS resulted in activation of both CAP and other non-target neural pathways. Previously, we have shown that targeted or precision ultrasound neuromodulation at the splenic site (reported to contain no vagal afferent neurons) results in separable activation of the CAP versus other non-target pathways (such as the glucose sensing cells in the liver). Herein, we show that separable modulation of inflammatory versus metabolic pathways is also possible at

the sacral stimulation site; however, stimulation of vagal afferents at the no dose ganglion results in activation of multiple pathways (similar to traditional cervical VNS; Figure 2-2 D). In addition, analysis of the change in circulating neurotransmitters after stimulation across the different sites also agrees with an updated systemic view of the CAP pathways. That is, the blood neurotransmitter profile is dominated by acetylcholine (Ach) after targeted stimulation of the splenic site, in agreement with the activation of the abundance of resident choline acetlytransferesase (ChaT) positive T cells. This is accompanied by a moderate increase in catecholamines (compared to no dose stimulation), which is required at the splenic site for activation of the ChaT T cells. In contrast, no dose stimulation resulted in a more moderate increase in Ach, but a larger increase in circulating catecholamines (which would be in agreement with a system-wide activation of multiple efferent CAP arms, i.e. splenic and enteric CAP pathways[48]. Finally, the sacral ganglion stimulation resulted in moderate increases in both Ach and catecholamines (compared to the splenic or no dose stimulation sites, respectively); however, stimulation at this site led to the greatest increase in circulating dopamine, suggesting activation of additional vagal-mediated anti-inflammatory pathways that have been mapped to the adrenal gland[49]. Taken together these results demonstrate that image/anatomical targeted pFUS is capable of activating neurons at multiple locations within mapped reflexes and may be used to assess the level of activation of target versus non-target nerve pathways within the PNS.

Next, we used pFUS to stimulate multiple hypothesized sites of PNS control over systemic metabolism (Figure 2-3 A). In hepatic pFUS experiments, US-image guidance was utilized to target the porta hepatis region of the liver, as described previously (Cotero et al., 2019a). This region of the liver is known to contain glucose (and other metabolite and hormone)

sensitive cells, which communicate with and modulate metabolic control centers within the hypothalamus. As shown previously, increasing blood glucose concentrations occur within 10 min of LPS exposure in the LPS only controls (no ultrasound stimulation) and hepatic pFUS limits the increase in blood glucose due to LPS exposure (60-min blood glucose concentrations limited to ~200 mg/dL versus ~365 mg/dL in the LPS controls). In this report, we show that pFUS modulation of other metabolic tissue targets also has a preventive effect on LPS-induced hyperglycemia (Figure 2-3 A and B). Stimulation of the pancreatic target resulted in a greater difference between 60-min blood glucose concentrations in the stimulated group versus LPS controls (~175 mg/dL 60-min value versus ~200 mg/dL in the hepatic stimulation group). The intestinal target also resulted in a decreased 60-min blood glucose result, the effect at that site was reduced compared to the hepatic and pancreatic groups (~275 mg/dL versus ~200 mg/dL in the hepatic stimulation group).

Previously, we have shown that the protection against LPS-induced hyperglycemia from targeted hepatic pFUS (i.e. at the porta hepatis but not at adjacent lobes) was coincident with changes in hypothalamic and not hepatic measures of insulin signaling and glucose utilization (including changes in insulin receptor substrate (IRS-1) and protein kinase B (pAkt) activation). We further verified that neurons within afferent pathways were modulated because of the hepatic stimulation, using c-Fos staining (in both brainstem and hypothalamic tissue sections taken from ultrasound versus control animals). The hypothalamic sub-nuclei and brainstem ganglia in which cFos expression was altered by ultrasound stimulation were those that are known to modulate glucose homeostasis[13]. In addition, diffusion-weighted functional magnetic resonance imaging (DfMRI) was used to compare the apparent diffusion coefficient (ADC) in brain images before

and after hepatic pFUS. The ADC (a MRI measure that has been shown sensitive to changes in nerve activity driven by external neuromodulators) was also shown to change significantly within the paraventricular nucleus (PVN), which is the nuclei known to carry outgoing signals of peripheral metabolic regulation. This combined data suggests that pFUS activation of afferent neural pathways are resulting in ultrasound modulation of hypothalamic insulin sensitivity, and corresponding changes to hypothalamic metabolic homeostasis and signaling.

Figure 2-4 A shows new measurements from hypothalamic samples collected before and after pFUS targeted to the three different anatomical sites described above (Figure 2-3 A). In agreement with the previous study, hepatic stimulation resulted in increased activity of hypothalamic pAkt. We further report an increase in hypothalamic GLUT-4; all three of these changes are associated with receptor and protein subunits within the insulin signaling pathway that are shown to be dysfunctional or reduced in models of altered glucose and energy homeostasis[34,50,51]. In addition, we observed a significant increase in glucose-6-phosphate, that indicates an increased hypothalamic conversion of glucose (by glucokinase) in the ultrasound stimulated animals. This conversion (thought to occur intracellularly) suggests pFUS mediated increase in glucose uptake in hypothalamic neurons, which is the proposed first step in the mechanistic response of glucose sensing neurons to hyperglycemia. Also, in agreement with our first report NPY levels are shown to be significantly decreased in the hepatic stimulated samples. We further show a significant increase in GABA concentrations; a neurotransmitter that has been shown (through single cell gene expression analysis) to be highly expressed in the hypothalamus and has been proposed as a marker of glucose sensing activity.

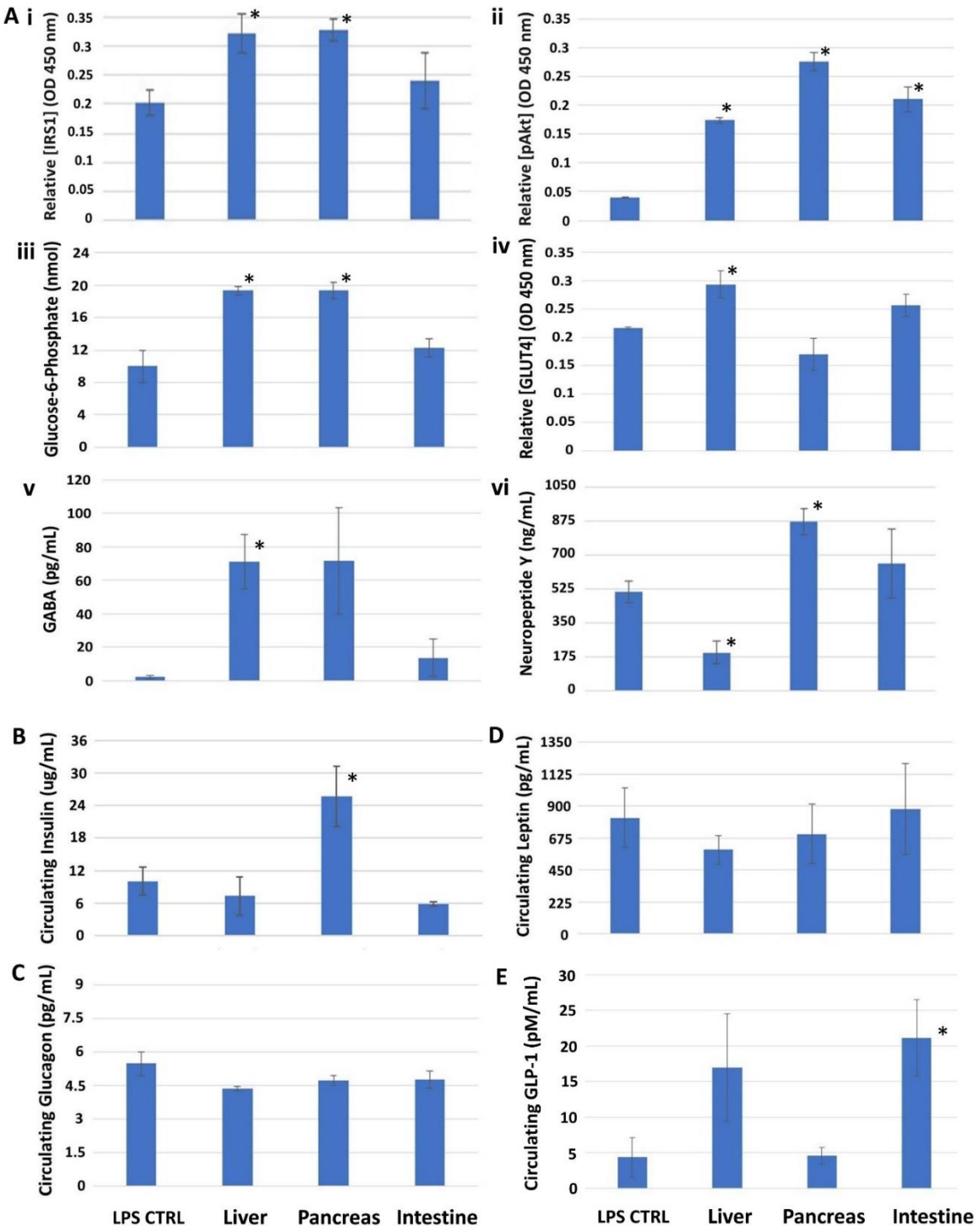

Figure 2-4 A biomarker observation with pFUS activation.
(A) Hypothalamic markers measured after pFUS at each target site. Relative intensities (optical ELISA intensities across matched samples) or sample concentrations (ELISA values compared to standard concentration curves) of molecules associated with insulin signaling and glucose utilization in hypothalamic tissue samples (including insulin receptor substrate 1 (IRS1; i), phosphorylated protein kinase B (pAkt; ii), glucose transporter type 4 (GLUT4; iv), glucose-6-

phophate (G-6-phos; iii), gamma-aminobutyric acid (GABA; v), and neuropeptide Y (NPY; vi). Data is shown for the LPS control (no ultrasound, LPS CTRL), liver pFUS (liver), pancreatic pFUS (pancreas) and intestinal pFUS (GI). (B) ELISA-based concentrations of circulating insulin for controls and each pFUS target site. (C) ELISA-based concentrations of circulating glucagon for controls and each pFUS target site. (D) ELISA-based concentrations of circulating leptin for controls and each pFUS target site. (E) ELISA-based concentration of circulating incretin GLP-1 for controls and each pFUS target site. The asterisks mark statistical significance using a one-way ANOVA with follow-up tests that include a Tukey's multiple comparison (using statistical hypothesis testing for previous t-tests). Significance is indicated as * when $p \leq 0.05$, indicating a moderate level of significance compared to LPS-sham controls, N = 6 for each experimental condition.

Figure 2-4 B also shows agreement with the circulating hormone measurements made in the past hepatic stimulation report[13], that is circulating insulin (along with glucagon and leptin concentrations) remains unchanged in the hepatic pFUS samples. This further supports a hypothalamic[34] (rather than pancreatic[52,53] mediated alteration of peripheral insulin and glucose utilization after the hepatic stimulation. Interestingly, both pancreatic and gastrointestinal pFUS also resulted in prevention or reduction of LPS-induced hyperglycemia (as shown previously in Figure 2-3 B). However, both the hypothalamic and circulating markers suggest that this effect occurs through separate pathways, when compared to the previously reported hepatic stimulation results. Pancreatic stimulation resulted in an increase in circulating insulin (Figure 2-4 B). A similar effect has been reported previously[46], in which ultrasound stimulation was capable of eliciting insulin release from pancreatic beta cells in a calcium-signaling dependent manner. This suggests that ultrasound is capable of activating secretion of insulin stores within the pancreas. Both IRS and pAkt activity was increased in the hypothalamus in the pancreatic stimulated animals (compared to LPS controls); however, unlike the hepatic stimulation animals GLUT4 was not (Figure 2-4A). Unlike other glucose-responsive neurons within the hypothalamus, GLUT4 expressing neurons are thought to be solely responsive to peripheral sensory pathways and nutrient response. Thus, the differences in hypothalamic signaling data corroborates our

previous circulating insulin data, and a direct insulin versus sensory signaling pathway involvement in the pancreatic pFUS effect (versus hepatic pFUS in which the effect involved other hypothalamic signaling pathways).

Intestinal (GI) pFUS also had a significantly different effect on hypothalamic and circulating metabolic markers (Figure 2-4 A and B–E) compared to the hepatic stimulation results. Like the hepatic stimulus, GI stimulation had no effect on circulating insulin (4B), glucagon (4C), or leptin (4D). However, GI stimulation also had no effect on IRS activity or GLUT4 and glucose-6-phosphate levels within the hypothalamus (4A). Thus, unlike the pancreatic or hepatic stimulation, the GI results suggests that a non-insulin signaling pathway is responsible for the GI stimulation effect on LPS-induced hyperglycemia. Still, the increased pAkt activity in the GI stimulated hypothalamic samples suggests there is a hypothalamic involvement in this other pathway, either directly or as an indirect effect. Figure 2-4 E suggests that GI stimulation results in modulation of the circulating incretin, glucagon-like peptide 1 (GLP-1)[47] secretion pathway within the small intestine. This is supported by an observed increase in hypothalamic GLP (data not shown) after GI pFUS, and previous literature demonstrating that electrical GI stimulation can affect these hormonal pathways[54]. Previous reports have shown that GLP1 receptor mRNA is densely expressed within the hypothalamus, where it may exert an effect on glucose regulation by altering both gastric emptying, glucose tolerance and insulin sensitivity[47]. Further investigation of the mechanisms associated with each of these pathways will be the subject of future work from our research group.

It is interesting to note that liver pFUS resulted in an increase in circulating norepinephrine, while pancreatic stimulation resulted in no apparent change in neurotransmitter concentrations and intestinal stimulation resulted in a dopamine specific change in neurotransmitter profile (Figure 2-5). Sympathetic nerves are known to be co-located at the porta hepatis with glucose and fatty acid sensing afferents fibers; these nerves are thought to provide a mechanism for hepatic vasoconstriction and modulation of blood pressure[55]. Dopaminergic neurons are known to be present in the intestine (but to a lesser extent in the liver or pancreas), these nerves are co-localized with the neuroendocrine cells that produce GLP and serve as an additional regulatory component in metabolic control and homeostasis[56]. In addition, the lack of catecholamine concentration changes upon ultrasound stimulation and the presence of non-neuronal SNARE-mediated secretory granules in both beta cells (i.e. pancreatic cells responsible for insulin secretion) and intestinal neuroendocrine cells (i.e. intestinal cells responsible for GLP secretion) suggest that ultrasound is capable of stimulating secretion from more than just neurons. Still, the data herein demonstrates that pFUS can be applied to rapidly screen for potential therapeutic stimulation sites (of both neural and neuroendocrine origin), and that local, precision stimulation of specific anatomical targets provides a new method of modulating and further understanding physiological systems.

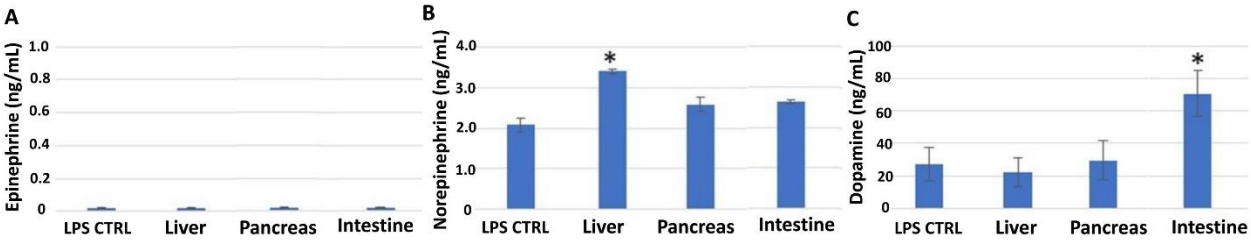

Figure 2-4 LPS study with pFUS neuromodulation.
(A) Circulating concentrations of epinephrine after pFUS at each target stimulus site and LPS/no pFUS controls (LPS CTRL). (B) Circulating concentrations of norepinephrine after pFUS at each target stimulus site and LPS/no pFUS controls (LPS CTRL). (C) Circulating concentrations

of dopamine after pFUS at each target stimulus site and LPS/no pFUS controls (LPS CTRL). The asterisks mark statistical significance using a one-way ANOVA with follow-up tests that include a Tukey's multiple comparison (using statistical hypothesis testing for previous t-tests). Significance is indicated as * when $p \leq 0.05$, indicating a moderate level of significance compared to LPS-sham controls, N = 6 for each experimental condition.

We have previously shown that low-intensity mechanical ultrasound stimuli are capable of site-specific nerve modulation in both in vivo and in vitro models[13,15,57–60]. Here, the mechanical origin of ultrasound neuromodulation was further confirmed using a purely mechanical stimulus (that is, replacing the ultrasound transducer with a mechanical piston-based stimulator; figure 2-5, and demonstrating the dependence of ultrasound nerve activation on specific families of mechano-sensitive ion channels[15,61] (figure 2-6).

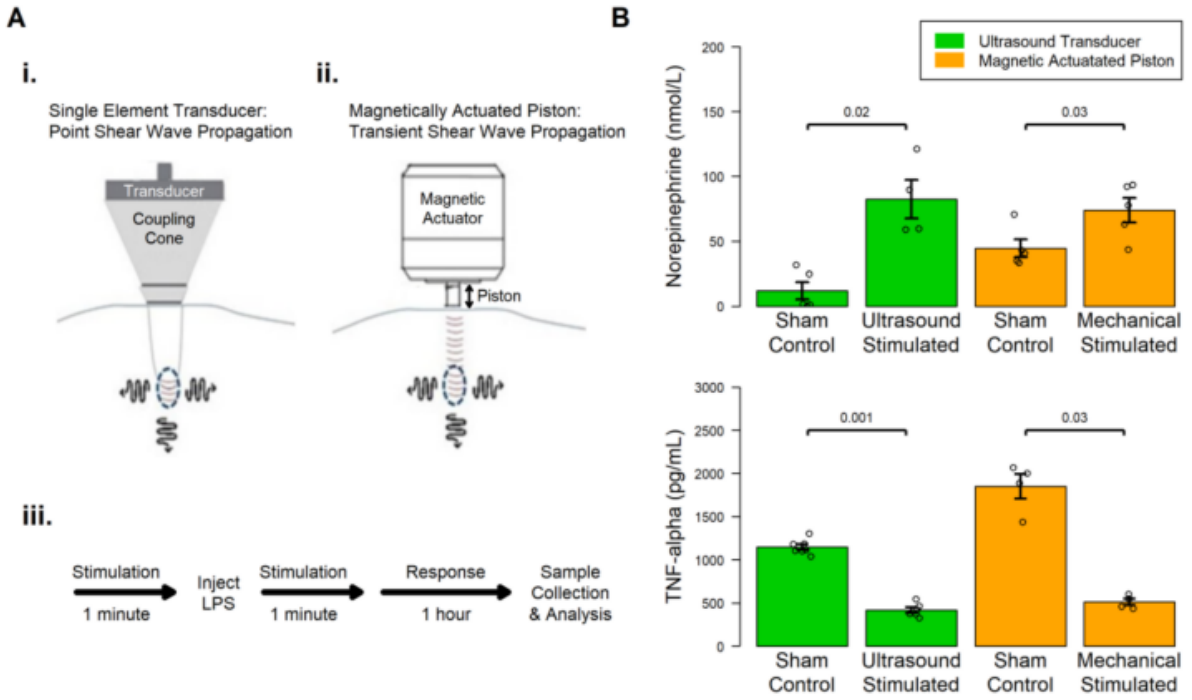

Figure 2-5 pFUS effect is dependent on the activity of mechanically activated ion channels in both in vitro and in vivo models.
A. Activation and neuromodulation of the splenic cholinergic anti-inflammatory pathway (CAP) using both an ultrasound and a mechanical piston-based transducer.15 We have previously demonstrated use of pFUS to activate the splenic cholinergic anti-inflammatory pathway. In this figure, we demonstrate that pulsed mechanical ultrasound and direct mechanical pulsed stimuli

(at similar pulse repetition frequencies) result in nerve activation and neuromodulation of CAP. This data enabled focused investigation of ion channel blockers that have previously been shown to inhibit channels affected by mechanical stimuli (such as TRPA1). i. A schematic of the ultrasound transducer described previously (and its acoustic coupling to the animal using the water-filled coupling cone). As described above, the transducer provides an ultrasound-based stimulus with a mechanical component based on point shear wave propagation at the focal point of the ultrasound stimuli.15,130,131 ii. A schematic of the non-ultrasonic, magnetically actuated piston described above to provide a mechanical stimulus when directly coupled to the animal (based on 1D transient shear wave propagation from the pistontissue interface).131 iii. The timeline of ultrasonic or mechanical neuromodulation experiments performed in the LPS-induced inflammation model.15 B. (left) Concentration of splenic norepinephrine (NE, top) and TNF alpha (bottom) with and without ultrasound stimulation in LPS-treated animals versus sham controls. (right) Concentration of splenic norepinephrine (NE, top) and TNF alpha (bottom) with and without mechanical-piston based stimulation in LPS-treated animals versus sham controls. In evaluating CAP response to the mechanical-piston stimulus to ultrasound-based stimulation (as measured by CAPrelated neurotransmitter (NE) and cytokine (TNF alpha) concentrations),15 the mechanical piston-based stimulation resulted in nearly identical elevation of NE and reduction of splenic TNF in response to the piston versus ultrasound transducer-based stimulus. All p-values shown are derived using nonparametric Wilcoxon rank-sum test (two-sided). Norepinephrine measurements are n=4 using the ultrasound transducer and n=5 using the magnetic piston. TNF measurements are n=6 for ultrasound transducer and n=4 for mechanical transducer. Data shown as mean ± s.e.

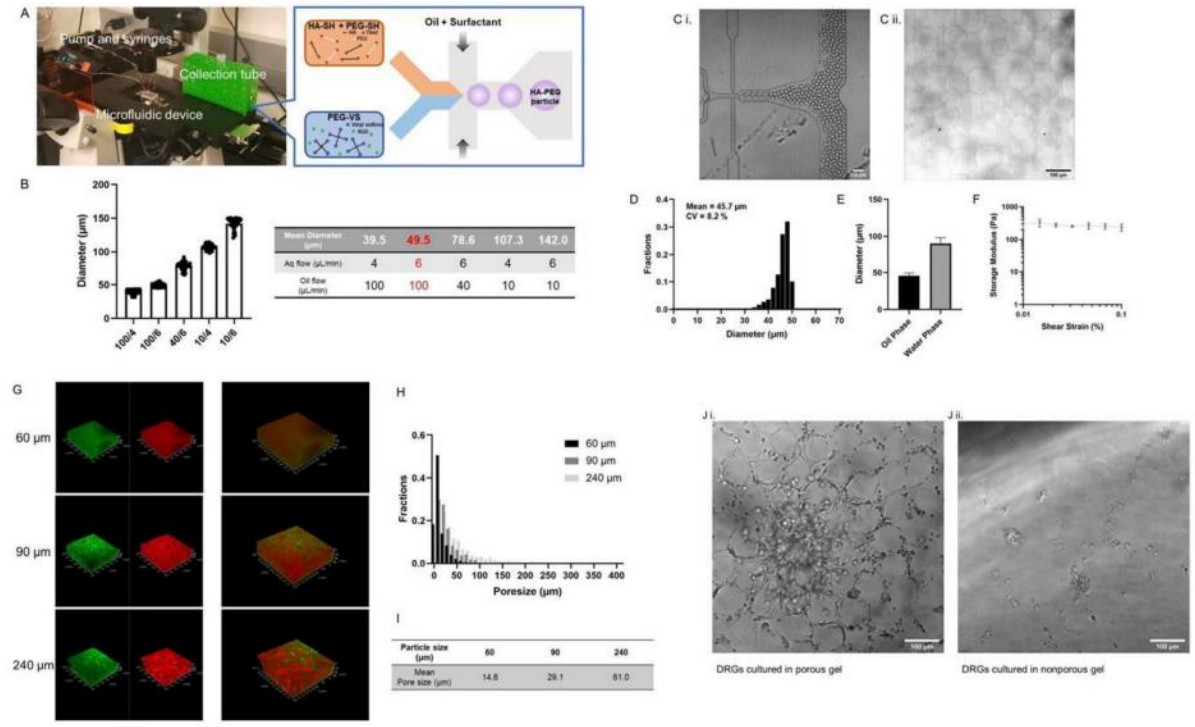

Figure 2-6 Material characterization of HA based MAP gel platform.
A. Photograph of the setup for microparticle fabrication and scheme illustrating microgel formation that is utilized to provide an optimal growth environment for three-dimensional culture of neurons using a microfluidic water-in-oil emulsion system. A pre-gel and crosslinker solution are segmented into monodisperse droplets followed by in-droplet mixing and crosslinking via Michael addition. B. The operational regime for microfluidic microgel generation has a large dynamic range, spanning almost an order of magnitude in size while maintaining tight control at each condition, with Coefficient of Variation (CVs) < 7% in all cases (n = more than 33 (n<100/4> = 105, n<100/6> = 171, n<40/6> = 68, n<10/4> = 45; data shown as mean ± SD). We use 50-100 μm microparticles for experiments as this provided the best pore size for neuron culture. C.i. Representative images of microgel droplets in flow after generation, which are utilized to fabricate the three-dimenstional neuron culture. C.ii. Representative images of cross-linked microgels after phase transfer. D. Generation of HA microgel particles with highly defintes sizes. E. HA microgel particles made with 50 μm diameter, when surrounded by oil swell in buffer after aqueous extraction from the oil phase (n=11; data shown as mean ± SD). F. Storage moduli of hydrogels. (n=3; data shown as mean ± SD). HA microgel particles were manufactured with an ideal storage modulus tuned for neuron culture (< 500 Pa). G. Confocal reconstructions of HA microgel-based neuron culture84 scaffolds after incubation with high molecular weight (Mw = 500 kDa) FITC-dextran indicates interconnectivity of the void spaces through the scaffold. In all cases, FITC dextran is represented in green and HA microparticles are represented in red. Different size of particles yield different void spaces. H. and I. Different building-block sizes allow deterministic control over resultant microporous network characteristics. 30 μm, 50 μm and 100 μm diameter microgel particles yield 15 μm, 25 μm, and 60 μm mean pore size respectively. Since dissociated neurons are around 10 ~ 30 μm, we chose

50-100 µm microgel particles for further cell culture experiments. J i. Bright field image of 3D culture of neuron cells within an HA-based microporous gel. J. ii. Bright field image of 3D culture of neuron cells within a HA- based nanoporous gel (i.e., cell directly embedded in the gel).

Three-dimensional (3D) in vitro cultures of dorsal root ganglia sensory neurons were activated (as measured by calcium indicator dye) using ultrasound pulse parameters and pressures that correspond to those from our in vivo experiments[62,63]. Blocking of N-type calcium channels (ω-conotoxin) or voltage-gated sodium channels (tetrodotoxin) did not attenuate the response to pFUS (Figure 2-7). In contrast, blockade using a non-selective mechano-sensitive ion-channel blocker (that is, GxMTx4) or a specific blocker of transient receptor potential (TRPA1; that is, HC-030031) channel inhibited the pFUS effect (Figure 2-7). To determine whether TRPA1 was also required to achieve the glucose-lowering effect of hepatic pFUS in vivo, GTT studies were repeated after a single local injection of the specific TRPA1 blocker (HC-030031; 8 mg kg−1) at the porta hepatis in a fasted ZDF rat. Confirming the important contribution of this channel, blocking TRPA1 indeed abolished the ability of pFUS treatments to lower blood glucose levels during GTT (Figure 2-7). It is noteworthy that ion channels within the TRP family are expressed on afferent neurons and have been reported to be required for functional glucose and metabolite sensing[64–68]. Furthermore, it was previously shown that activation of TRPA1 (target of HC-030031) by allyl isothiocyanate improves glucose uptake and insulin signalling in multiple models of T2D by an unknown mechanism[69], while ablation of TRPV1 and TRPA1 expression (targets of GxMTx4) results in severe insulin or leptin resistance[66,70].

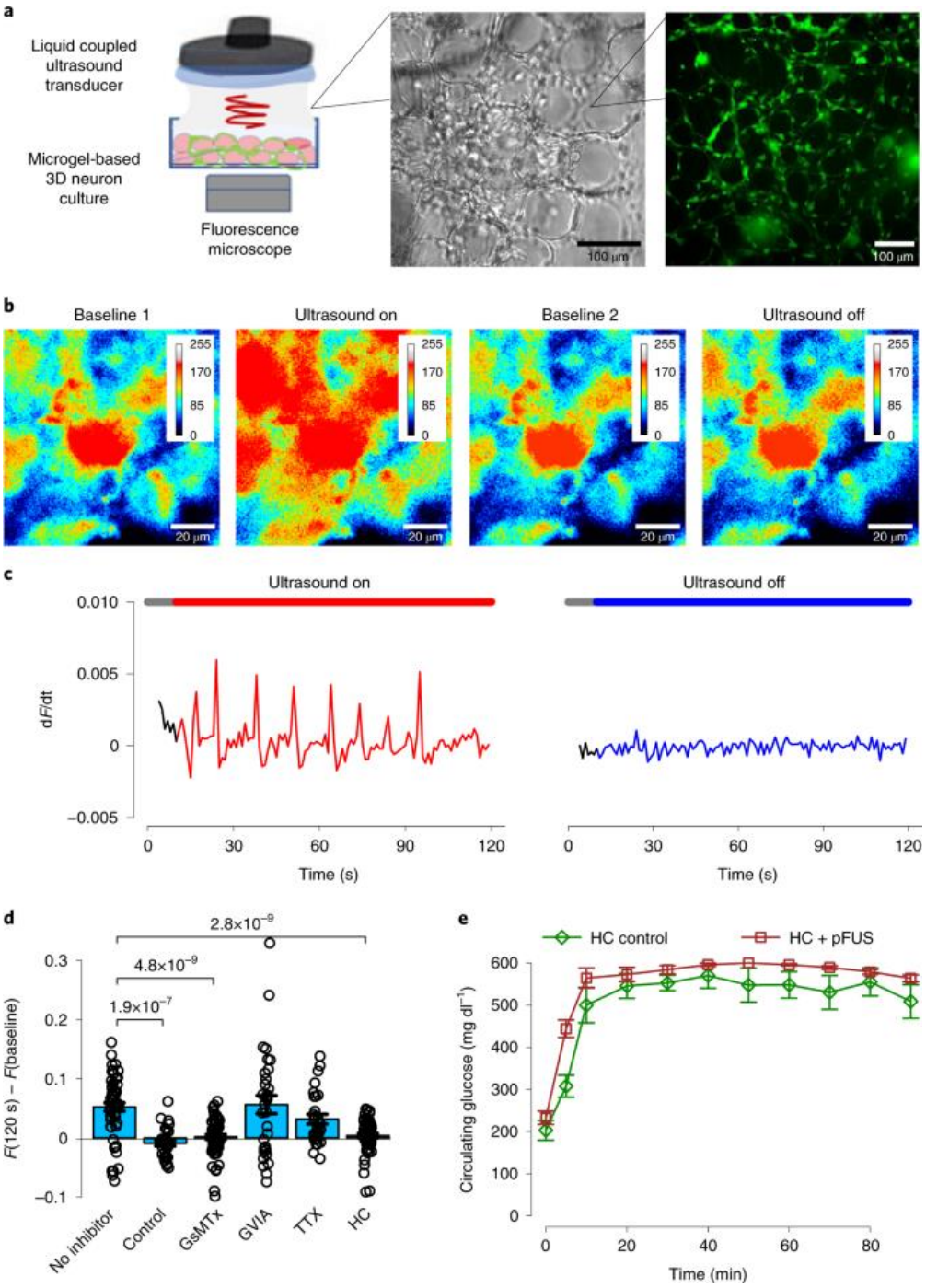

Figure 2-7 pFUS effect is dependent on the activity of mechanically activated ion channels in both in vitro and in vivo models.

a, Schematic of the 3D peripheral neuron culture system, and experimental setup (left; details in Methods) used to capture images of DRG neuron cells before and after pFUS stimulation. The DRG neuron culture has previously been shown18,79 to create active axonal networks through the pores formed between hydrogel particles (bright-field (middle) and fluorescence (right) images are shown). b, The zoomed-in fluorescence images show a time lapse of calcium (Ca2+)

imaging during pFUS stimulation (colour bars, fluorescence intensity units). pFUS stimulation was turned on at 10 s (ultrasound on) following a brief period of time for collecting baseline images (baseline 1) and turned off again at 120 s. The ultrasound remained off for 2 min before retaking a second baseline (baseline 2) and measurement period (ultrasound off). Calcium concentrations of DRG neurons increased after ultrasound stimulation and returned to baseline levels upon pFUS cessation. c, pFUS excitation of DRG neurons led to large changes in Ca2+-dependent fluorescence (F). The rate of change, dF/dt, remained small without application of ultrasound stimulus (ultrasound off) compared with the significant dF/dt increases shown during pFUS stimulation (ultrasound on; at 0.83 MPa peak-positive pressure without any ion-channel blocker added to the culture with N > 30 cells per condition). d, Observed fluorescence change before/after ultrasound stimulation using multiple ion-channel blockers (N > 30 cells per condition). TTX is a specific inhibitor of voltage‐gated sodium channels involved in action potential propagation, ω‐conotoxin‐GVIA is an N‐type Ca2+ channel inhibitor, and HC-030031 (HC) is a sensitive TRPA1 channel inhibitor. When piezo- or TRP-family blockers GsMTx and HC-030031 were added to the culture, pFUS-induced activity was significantly suppressed. e, HC-030031 is shown to inhibit the pFUS effect on glucose in vivo when locally injected at the porta hepatis in ZDF rats (n = 4 per group; GTT performed after overnight fast at age 65 d). The GTT was performed in both pFUS-treated (HC + pFUS) and control animals given the HC injection but no pFUS (HC sham control). Unlike ZDF rats without HC treatment, no statistical difference in circulating blood glucose was observed in animals treated with the TRPA1 blocker. All P values shown were derived using nonparametric Wilcoxon rank-sum test (two-sided). Data shown are mean ± s.e.m.

2.3. Conclusion

In our previous report, we compared the hepatic pFUS effect on LPS-induced hyperglycemia to that using standard vagus nerve stimulation (VNS; i.e. an implantable cervical vagus nerve stimulation cuff or electrode)[13]. In that report, we noted that the effect of VNS on hyperglycemia was first observed as a side-effect in studies seeking to stimulate the cholinergic anti-inflammatory pathway (CAP), a vagus nerve mediated reflex culminating at neuroimmune synapses and connection within the spleen[16]. In addition, we showed that this side-effect of targeted CAP activation (i.e. the additional activation of metabolism associated pathways) was inseparable using the standard implant-based tools. But, in contrast, separate modulation of inflammation only (i.e. the splenic CAP pathways) versus metabolism only (i.e. the hepatic metabolic sensory pathway) was possible using the pFUS technique. In this context, we

demonstrated that unlike implant-based VNS, pFUS neuromodulation was capable of separately effecting different parts of the peripheral nervous system involved with separate and distinct physiological functions.

Herein, we further advance this concept and show that pFUS can be used to parse out the contribution of signaling from multiple points within a single physiological system (i.e. the cholinergic anti-inflammatory pathway and the metabolic control system. We showed that both direct end-organ stimulation and stimulation of peripheral ganglion (in communication with those end-organ sties) enable activation of specific neural pathways (i.e. cytokine reduction via activation of CAP). We also showed that stimulation at different sties (i.e. end-organ vs. peripheral ganglia) resulted in a site-dependent level of pathway activation versus activation of other non-target nerve pathways (i.e. cytokine reduction versus modulation of blood glucose levels). We also showed that like hepatic pFUS, ultrasound-based stimulation of the pancreas and gastrointestinal tract led to significant reduction in LPS-induced hyperglycemia. Then, we demonstrated that pFUS stimulation of the different sites drove changes in glucose utilization via distinct signaling pathways. Unlike other nerve targeting tools (such as optical and genetic nerve selection tools the pFUS technique required no complex surgeries or genetic manipulation. Instead, pFUS targeting was achieved by selecting organ and sub-organ targets functionally related to the area of study (i.e. metabolism and metabolic dysfunction) and then targeting pFUS to the natural anatomical collections of nerve endings or neuroendocrine cells at those sites. Thus, this pFUS method, which utilizes the natural hierarchical structure and organization within the nervous system at the organ level, is in stark contrast to the current implant[22,23] and genetic[25] methods that seek to gain physiological specificity by achieving neuron level stimulation within

large nerve bundles (far away from organ innervation and the site of organ function and modulation).

In this report, we also verify that ultrasound (at the same applied acoustic frequency, pressure, and pulse parameters used for in vivo modulation enables direct peripheral nerve activation in a controlled in vitro culture. Our results herein, combined with other groups reports on observations of ultrasound activation of both neuronal and non-neuronal (i.e. excitable endocrine and secretory cells) cells suggest a new and potentially impactful use of ultrasound. In the context of drugs and pharmaceutical therapies it is difficult to administer a drug through normal routes (i.e. systemic ingestion or infusion) and yield therapeutically relevant concentrations of that drug only at specific, local anatomical locations. In contrast, pFUS can be used to rapidly alter local neurotransmitter and hormone concentrations, essentially driving therapeutic interventions with local drug targets (such as cytokine, insulin, incretins, and neurotransmitters).

The results herein (and the spleen and liver pFUS results reported previously) suggest that precision organ-based ultrasound neuromodulation may provide a new tool to stimulate the peripheral nervous system and map its effect on organ function. The insulin signaling and glucose utilization markers (IRS1, pAKT, glucose-6-phospate, and GABA) shown activated by hepatic pFUS herein, represent the same markers that are currently being investigated to map out the brain's role in homeostatic regulation of energy and glucose metabolism. The hypothalamus is now known to integrate many metabolic inputs from the periphery (including nutrient sensory signals, gut-derived satiety signals and adiposity-related hormones), and then modulate various

aspects of peripheral metabolism (including food intake, energy expenditure, insulin secretion, hepatic glucose production, and glucose/fatty acid metabolism in adipose and skeletal muscle). It is also now known that defective crosstalk between the brain and peripheral organs (along these control pathways) contributes to the development of chronic diseases, such as obesity and type II diabetes). However, the exact mechanisms by which the neural pathways are involved in these highly coordinated interactions (and their pathological dysregulation) has remained difficult to discern using standard chemical and pharmaceutical approaches (i.e. blocking or antagonizing molecular components of the pathways systemically through oral and injectable agents). In contrast, our results herein demonstrate a potential new method of precisely modulating individual components of such complex physiological control systems. That is, the use of pFUS for spatially distinct and anatomically defined bursts of molecular and cellular activity with sub-organ precision.

Future reports from our group will test pFUS in chronic models of disease (including pre-clinical models of diabetes and obesity) and seek to translate these techniques to clinical studies. As with any new experimental and therapeutic concept, clinical translation will hold challenges. However, while there are differences in the duration of ultrasound exposure for pFUS (Cotero et al., 2019b) (compared to standard clinical imaging ultrasound), the pFUS stimulation parameters have the potential to fall within standard clinical (MI (mechanical index) and TI (thermal index)) limits used to assess the potential for heating (TI) and cavitation-based (MI) adverse bioeffects. Looking forward, pFUS may be used across other physiological systems (i.e. non-metabolic related organ and tissue processes) and used to reveal the extent of the nervous system involvement in maintenance or dysregulation of normal function. Our group plans to continue to

work with the larger clinical and scientific community to safely perform the tests to determine the answers to these questions, and the extent that pFUS may be used to advance the field of bioelectronic medicine.

2.4. Materials and Methods

Focused ultrasound system

The system used for both in vitro and in vivo pFUS stimulation consisted of a 1.1 MHz single element transducer (Sonic Concepts H106), a matching network (Sonic Concepts), an RF power amplifier (ENI 350L) and a function generator (Agilent 333120A). The 70 mm diameter transducer had a spherical face with a 65 mm radius of curvature. The transducer had a 20 mm diameter hole in the center into which an imaging transducer is inserted during transducer alignment and anatomical targeting. The numerically simulated pressure profile had a full width at half maximum (FWHM) amplitude of 1.8 mm laterally and 12 mm in the depth direction. Acoustic coupling to the animal or culture plate was accomplished using a 6 cm cone filled with degassed water (coupled using either ultrasound gel for in vivo experiments or a column of culture media for in vitro experiments). The function generator was used to produce pulsed sinusoidal waveforms that are amplified by the RF amplifier and sent to the impedance-matching network. Experiments in this manuscript used a pulse repetition period of 0.5 ms (corresponding to a pulse repetition frequency of 2000 Hz), a pulse amplitude of 23 W/cm^2 (burst average) and a burst duration of 136 microseconds (corresponding to a duty cycle of 0.27). Experiments determining these parameters as optimal (for in vivo peripheral neuromodulation) have been reported previously, and replicated by separate laboratories, which were previously shown to

provide optimal activation of both splenic and hepatic nerve pathways. The voltage-to-pressure calibration of the transducer was performed and reported previously using a needle hydrophone.

Ultrasound targeting

For in vivo experiments, a vivid E9 or 11 L ultrasound system and probe (GE Healthcare) was used for imaging the anatomical target prior to pFUS neuromodulation. The pFUS transducer was then placed on the target area based on this initial image. A second ultrasound scan was also performed using a smaller imaging probe (3S; GE Healthcare), which is placed in the opening of the pFUS transducer and coupling cone. The imaging beam of the 3S probe was aligned with the pFUS transducer, and enabled confirmation of the organ and anatomical target of interest. Ultrasound stand-offs were utilized as needed to adjust the depth of the pFUS transducer focus. Anatomical markers were used to locate and align the ultrasound stimulus to each target stimulation site: The anatomical markers used to locate the no dose ganglion include the internal carotid artery (as the vagus runs along it toward the skull) and the posterior lacerated foramen where the ganglion is known to exist as a somal swelling of the vagus nerve at the base of the skull. For the sacral ganglia, the four sacral vertebrae were located, and the ultrasound transducer was aligned in the direction of the sacral foramina. The anatomical marker used for the liver stimulation experiments was the porta hepatis as reported previously[13]. For the pancreas, the splenic vein (imaged via the left lateral side through the spleen as to avoid nonspecific hepatic stimulation) was used as an anatomical marker for the pancreatic tail. The pancreatic tail was selected as it is known to contain dense population of islet cells and is distal from the duodenum. Imaging of the upper left quadrant of the peritoneal cavity was used to identify the jejunum

region of the small intestine, which under diagnostic imaging with Doppler ultrasound appears as a highly vascularized folded structure bearing multitude of folds.

Neuron culture and calcium imaging for in vitro ultrasound stimulation

We mixed isolated peripheral neurons (i.e. dorsal root ganglion cells), DRGs) with hydrogel microparticles2,3 and co-injected into a culture plate. After injection, the microparticle hydrogels were annealed, leaving a nerve cell-laden heterogeneous scaffold that provides both a mechanically stiff growth surface for nerve cell adhesion and interconnected micropores for neurite outgrowth.3 DRG neurons are cultured in 200 μL of NbActiv with 25 ng/mL NGF in the incubator with 37 $^{\circ}$C and 5% CO2 concentration. 50% of Culture media was changed every 3 days. DRG neurons were incubated with Fluo-4 Direct calcium assay kit with 250 × 10−3 M stock solution of probenecid for Ca imaging. Briefly, 5 mL of calcium assay buffer was mixed and vortexed with 100 μL of probenecid stock solution to create a 2× loading dye solution. The dye solution was then added to the cells with media in a 1:1 ratio and incubated for 1 h before imaging to allow sufficient diffusion through the hydrogels.

Animal model and ultrasound stimulation

All experiments were performed under protocols approved by the Institutional Animal Care and Use Committee of GE Global Research. Adult male Sprague–Dawly rats 8–12 weeks old (250−300 g; Charles River Laboratories) were housed on 12-h light/dark cycles and acclimatized for 1 week before experiments were conducted. Housing was maintained at 25 °C and water and regular rodent chow were available ad libitum. Lipopolysaccharide (LPS) from Escherichia coli

(0111: B4; Sigma Aldrich) was used to produce inflammation and metabolic dysfunction (i.e. hyperglycemia). 10 mg/kg of LPS was administered by intraperitoneal injection, and after LPS administration blood was collected from the tail vein at 0, 5, 15, 30, and 60-min timepoints. LPS induced cytokine storm and insulin resistance is well-documented in literature, and these timepoints correspond to the onset and advancement of hyperinsulemia/hyperglycemia within the model. Blood glucose concentration were measured by a OneTouch Elite glucometer (LifeScan; Johnson and Johnson). Following the 60 min timepoint the brain was removed and dissected with particular interest to collection of hypothalamic tissue samples. Hypothalamic tissues were homogenized in a solution of phosphate-buffered saline (PBS) containing phosphatase (0.2 mM phenylmethylsulfonyl fluoride, 5 μg/mL aprotinin, 1 mM benzamidine, 1 mM sodium orthovandate, and 2 μM cantharidin) and protease inhibitors (1 μL to 20 mg of tissue as per Roche Diagnostic instructions). Additional tissue samples (e.g. ganglia, spleen, liver, and intestinal tissue) were also obtained at 60 min and flash frozen in liquid nitrogen for later analysis. Blood samples collected throughout the study were stored with disodium (ethylenedinitrilo)tetraacetic acid (EDTA) anti-coagulant. All sample were stored at −80 °C prior to analysis. Tissue and terminal blood samples were analyzed by enzyme-linked immunosorbent assay (ELISA) for TNF (tumor necrosis factor; Invitrogen), metabolic hormone or signaling molecules: including insulin (Crystal Chem), glucagon (Aviva Systems Biology), leptin (Aviva Systems Biology), IRS1 (insulin receptor substrate 1; Santa Cruz), phos-Akt (phosphorylated protein kinase B; MyBioSource), GLUT4 (glucose transporter type 4; Lifespan Biosciences), nd glucose-6-phosphate (G-6-phos; Lifespan Biosciences), according to manufactures instructions.

Catecholamines concentrations were measured from tissue samples using a HPLC protocol; briefly, Serum samples were injected directly into the machine with no pre-treatment. Tissue homogenates were initially homogenized with 0.1-M perchloric acid and centrifuged for 15 min, after which the supernatant was separated, and the sample injected into the HPLC. Catecholamines norepinephrine and epinephrine were analyzed by HPLC with inline ultraviolet detector. The test column used in this analysis was a Supelco Discovery C18 (15 cm × 4.6 mm inside diameter, 5-μm particle size). A biphasic mobile phase comprised of [A] acetonitrile: [B] 50 = mM KH2PO4, set to pH 3 (with phosphoric acid). The solution was then buffered with 100-mg/L EDTA and 200-mg/L 1-octane-sulfonic acid. Final concentration of mobile phase mixture was set to 5:95, A:B. A flow rate of 1 mL/min was used to improve overall peak resolution while the column was held to a consistent 20 °C to minimize pressure compaction of the column resulting from the viscosity of the utilized mobile phase. The UV detector was maintained at a 254-nm wavelength, which is known to capture the absorption for catecholamines including norepinephrine, epinephrine, and dopamine.

For ultrasound stimulation, animals were anesthetized with 2–4 % isoflurane and laid on a water circulating warming pad to prevent hyperthermia during the procedure. Prior to neuromodulation, the area above the anatomical area of interest was shaved with a disposable razor and animal hair clippers. After targeting (as described above), the ultrasound stimulus was applied for a duration of 1 min. The LPS was then administered immediately following the first ultrasound stimulus (as described above). A second 1-min ultrasound stimulus was then applied following the LPS administration for a total duration of 2 min. The animal was then allowed to

incubate under anesthesia, and blood samples were taken as described above. After incubation, the animal was euthanized, and tissue and blood samples were taken as described above.

Chapter 3. VaxMAP Platform for Influenza Vaccination

New vaccine platforms that properly activate humoral immunity to generate optimal neutralizing antibodies are required to combat emerging and re-emerging pathogens, such as influenza virus. Biomaterial scaffolds with macroscale porosity have demonstrated tremendous promise in regenerative medicine where they have been shown to allow immune cell infiltration and subsequent activation, but whether these types of materials can serve as an immunization platform has not been evaluated in detail. We developed an injectable immunization platform that uses a slurry of antigen-loaded hydrogel microparticles that anneal to form a porous scaffold with high surface area for antigen uptake by infiltrating immune cells that can maximize humoral immunity. Antigen-loaded-microgels elicited a robust cellular humoral immune response, with increased CD4+ T follicular helper (Tfh) cells and prolonged germinal center (GC) B cells comparable to the commonly used adjuvant, aluminum hydroxide (alum). Furthermore, immunization with the antigen-loaded-microgels promoted titers of antigen-specific high affinity antibodies similar to alum. By simply increasing the weight fraction of polymer material in the antigen-loaded hydrogel particles, we further increased antigen-specific high affinity antibody titers. Vaccinating mice with inactivated influenza virus loaded into this more highly crosslinked formulation provided protection against a high dose viral challenge and elicited a strong antibody response against influenza. This vaccine material platform achieves protection without the addition of traditional adjuvants and is highly modular in physical and chemical properties. The tunability of biomaterial physical and chemical properties for immunization against important antigens or inactivated pathogens enables innate and adaptive immune cell programming for generating high affinity antibodies, ultimately promising long-lasting protection against specific pathogens.

3.1. Introduction

Despite tremendous advances in our understanding of immunology over the past decades, this knowledge has not translated into comparable advances in new vaccine material platforms for delivery of traditional protein/subunit or inactivated vaccines to extend and enhance the versatility of immunity generated. Successful vaccines have been developed against non-mutating pathogens like measles, poliovirus, and smallpox. However, the rapid evolution of mutating viruses including influenza virus and SARS-CoV-2 still results in huge socio-economic and public health challenges[71–73]. Like many RNA viruses, influenza virus has a much higher mutation rate than DNA viruses, making the development of a universal vaccine challenging[74]. Many vaccine strategies against influenza A virus have been implemented, including inactivated, live-attenuated and recombinant, to provide protection primarily by eliciting neutralizing antibodies[75], however, these types of vaccines often fail to elicit adequate protection against an emergent strain with new mutations[76]. Contributing to the lack of long-term protection, antibody titers diminish after their peak at seroconversion, a few weeks after vaccination[77], and titers decline significantly by 180 days following vaccination in older adults[78] and return to pre-vaccination levels after one year[79].

To sustain antibody-mediated protection against a viral infection, a vaccine needs to elicit an antibody response against the correct epitope of the viral attachment protein that binds to host cells. To accomplish this, antigen-primed dendritic cells (DCs) from the immunization site migrate into in secondary lymphoid organs where they prime CD4+ T follicular helper (Tfh) cells. These Tfh cells then instruct and select the best activated, antigen-specific B cells to undergo affinity maturation within germinal centers (GC)[80–82]. The formation of GCs is critical

for the evolution of antibodies to properly target neutralizing epitopes of key viral antigens. Vaccine adjuvants, often provide danger or other signals to prime immune responses to co-delivered antigens to recruit specific immune cell subpopulations and sustain the productive development of specific humoral or cellular immunity. There are currently only seven approved traditional vaccine adjuvant materials (including the newly approved Matrix M), many of which have limited control over the immune cell types that are activated, modest effects on activating these cells, and therefore do not promote a superior vaccine response for GC development[83,84]. Ultimately, current adjuvant materials result in limited quantity, affinity, and breadth of GC-derived antibodies they can elicit, which negatively impacts the ability to neutralize current target antigens and future antigen variants following mutation. A new generation of highly tunable, immune-cell selective vaccine materials may help address these challenges.

Recent studies have reported that the physical properties of the vaccine delivery material are critical to controlling the activity of vaccines[85–90]. When optimized, the antigen delivery material can prolong the time for antigen uptake, improve the bioaccumulation in lymphoid organs, effectively target specific immune cells based on the type of danger signal elicited, and overall elicit optimal immune responses. Polymeric microspheres and aluminum hydroxide, for example, have been widely investigated as vaccine carriers that provide sustained release[91,92]. Continuous release of antigen over time allows them to enhance the duration of the interaction between the antigen and the immune system[93] and enhance the germinal center response and antibody levels[94]. Importantly, material stiffness cues in the microenvironment may directly polarize antigen-presenting cells (APCs) such as DCs involved in humoral immunity[95–97]. Stiffer substrates alter macrophage proinflammatory responses and polarize them towards an

inflammatory, phenotype[11,98,99]. Also, DCs grown in vitro on substrates with physiological stiffness were found to have reduced proliferation, activation, and cytokine production compared with cells grown on stiffer substrates. Still vaccine materials have not taken full advantage of material physical properties, and are usually formulated with cytokines, growth factors, and pathogen associated molecular patterns to specifically recruit, target, and activate immune cells to elicit optimal immune responses[100–102]. The development of an antigen-releasing biomaterial that, through its physical properties, can provide proper immune activation signals for Tfh cells and GC B cell signals can overcome some of the supply chain, stability, and quality control challenges with these current approaches.

We have previously reported Microporous Annealed Particle (MAP) gels – an injectable biomaterial platform in which hydrogel microparticles are linked in situ to form a porous scaffold[10–12,103]. This hydrogel provides porosity at the scale of cells (tens of micrometers), preventing a foreign body response and fibrous encapsulation. Recently, we found that treating skin wounds with a formulation of MAP where the chirality of amino acids within the crosslinking peptides was changed from L- to D-chirality (D-MAP) resulted in robust antibody responses to the antigenic D-amino acid-containing peptides and hair follicle regeneration in wounded skin[11]. Both recruitment of macrophages and hair follicle regeneration required an intact humoral immune response, suggesting that macroscale biomaterial scaffolds can directly influence humoral immunity and generate antibody responses to antigens contained within them[104,105].

We hypothesize that MAP can serve as a macroscale biomaterial-based vaccine platform that can be specifically tuned to activate the proper immune cells to achieve long-lasting and protective immunity against a viral pathogen without additional adjuvants. Herein, we test whether we can create vaccine-MAP scaffolds (VaxMAP), in which antigens or inactivated viral particles are embedded in the microgels during fabrication. We found that the VaxMAP platform activated an adaptive immune response and generated protective antigen-specific antibodies against a model antigen and inactivated influenza particles. By simply increasing the weight percentage of PEG within the microgels, which resulted in a more heavily cross-linked, and therefore stiffer hydrogel, we induced greater Tfh cell expansion, prolonged GC B cell development, and greatly enhanced high affinity antibody responses. The inactivated influenza virus particles (iIVP)-MAP elicited antibody responses against hemagglutinin and protected against a lethal influenza virus infection. Thus, VaxMAP represents a tunable, injectable biomaterial platform to enhance humoral immunity for traditional vaccines.

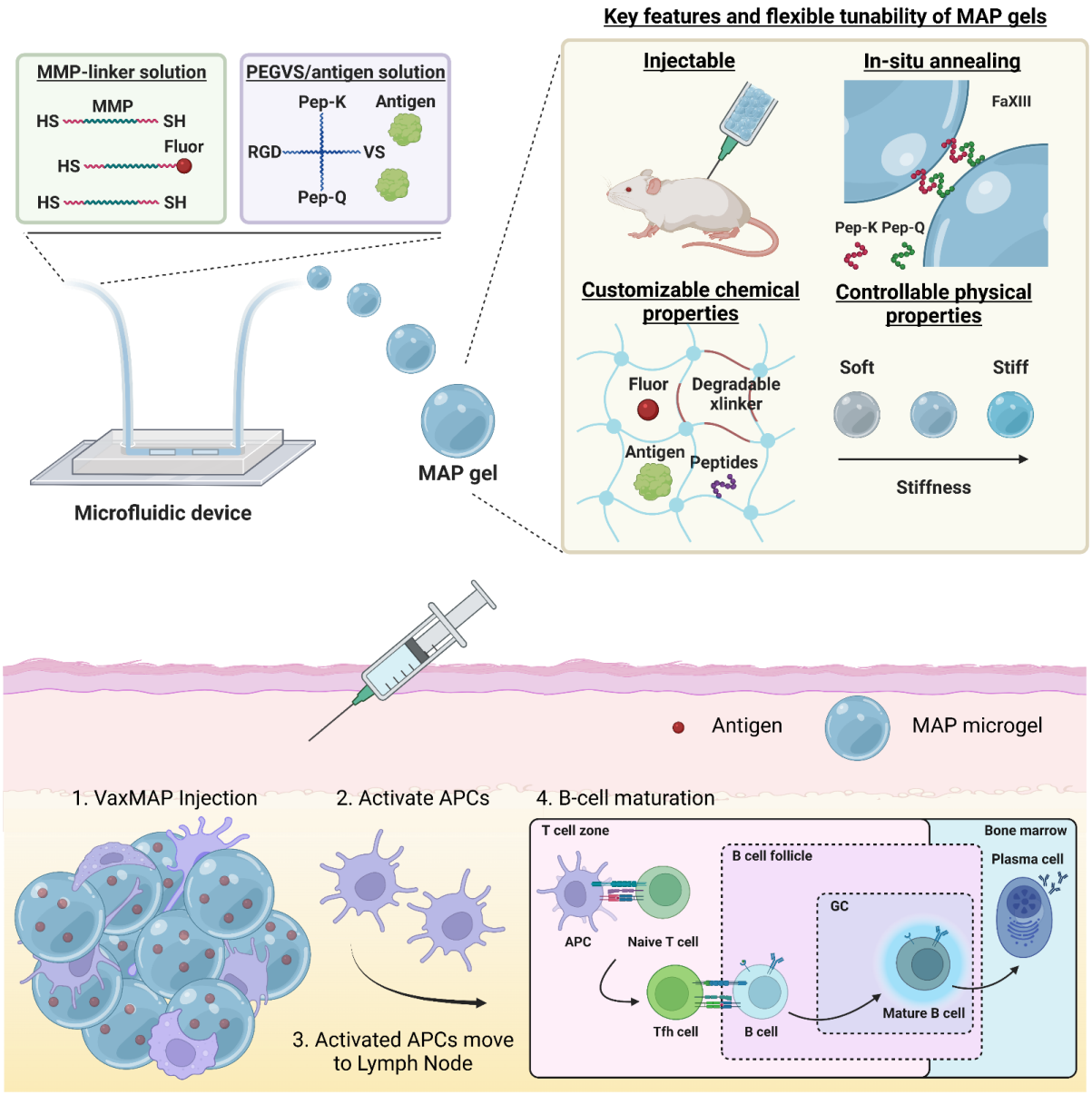

Figure 3-1 Scheme illustrating the microfluidic generation of VaxMAP scaffolds for vaccination.

A) MAP microgels are manufactured using microfluidic droplet emulsion polymerization from pre-gel solutions containing 4-arm PEG-vinylsulfone (PEG-VS) via thiol-ene reactions to encapsulate antigen in the dense gel mesh. Matrix metalloproteinase (MMP) degradable peptide linkers enable gel degradation. RGD peptides are present on the microgels to facilitate cell infiltration into the void spaces between gels, maximizing surface area for cell-biomaterial contact. The MAP microgel slurry is easily injectable and K and Q peptides enable linkage of microgels to tissue and each other by activated Factor XIII once injected. Microgel stiffness is controlled independently of cell-scale porosity. B) Pores between spherical gels allow immediate cellular infiltration. Gels are degraded and antigen is released by antigen presenting cells

(APCs), which then direct an adaptive immune response. Tfh cell development is initiated in the T cell zone where naïve T cell differentiation is instructed by antigen-primed dendritic cells. Newly formed Tfh cells and antigen-activated B cells meet at the border of the T cell zone and B cell follicle and following productive interactions, enter the follicle to form a germinal center (GC). Within the GCs, B cells undergo selection and differentiate into plasma cells.

3.2. Results and Discussion

Microfluidic emulsion generation-based polymerization allows the manufacture of highly customizable microparticles (Figure 3-1A). VaxMAP is composed of matrix metalloproteinase (MMP) sensitive polyethylene glycol (PEG)-based microgel beads decorated with K and Q peptides that are substrates for transglutaminases and allow the linkage of the microgels to each other and surrounding tissue. Monodispersed VaxMAP microgels (77.1±4.6 μm diameter average) were produced using a microfluidic droplet generator with consistent swelling ratios from particles with a total diameter ranging from 50 to 110 μm (Figure 3-2 A). The concentration of encapsulated antigen was controlled by changing the initial antigen concentration within pre-gel solutions (Figure 3-2 B). We also examined the influence of PEG concentration on the mechanical stiffness of MAP gels to investigate potential effects on immune modulation *in vivo*[106,107]. By increasing the PEG concentration from 5% to 7.5% the microgels had a higher crosslinking density and an increased hydrogel stiffness, resulting in a storage modulus that increased from ~1000 Pa to ~4000 Pa (Figure 3-2 C). A scaffold of packed microgel particles also resulted in cell-sized interconnected voids that led to higher convective flux of fluid (Figure 3-2 D, E). Despite only limited permeation occurring in the nonporous bulk hydrogel, the interconnected porosity of annealed MAP hydrogels derived from both 5% and 7.5% PEG microgels resulted in a more than 100-fold enhancement in fluid conductivity (Figure 3-2 F and Figure 3-3). We incorporated 4-hydroxy-3-nitrophenylacetyl hapten conjugated to ovalbumin (NP-OVA) antigen (MW = 45kD) into the gel matrix at various concentrations during

manufacture, without affecting the manufacturing process and found the NP-OVA would remain entrapped over at least a 3-day period (Figure 3-2 G). We also found that upon exposure to degradative enzymes *in vitro*, the NP-OVA was slowly released as the microgel particles swelled (Figure 3-2 G). In addition, *in vitro* culture of macrophages and dendritic cells with fluorescently-conjugated MAP gel resulted in fluorescently-labeled components accumulating within the cells after 1 day of culture and increasing over 7 days of culture with macrophages being able to take up more fluorescent label than DCs following breakdown of the material (Figure 3-2 H and Figure 3-4).

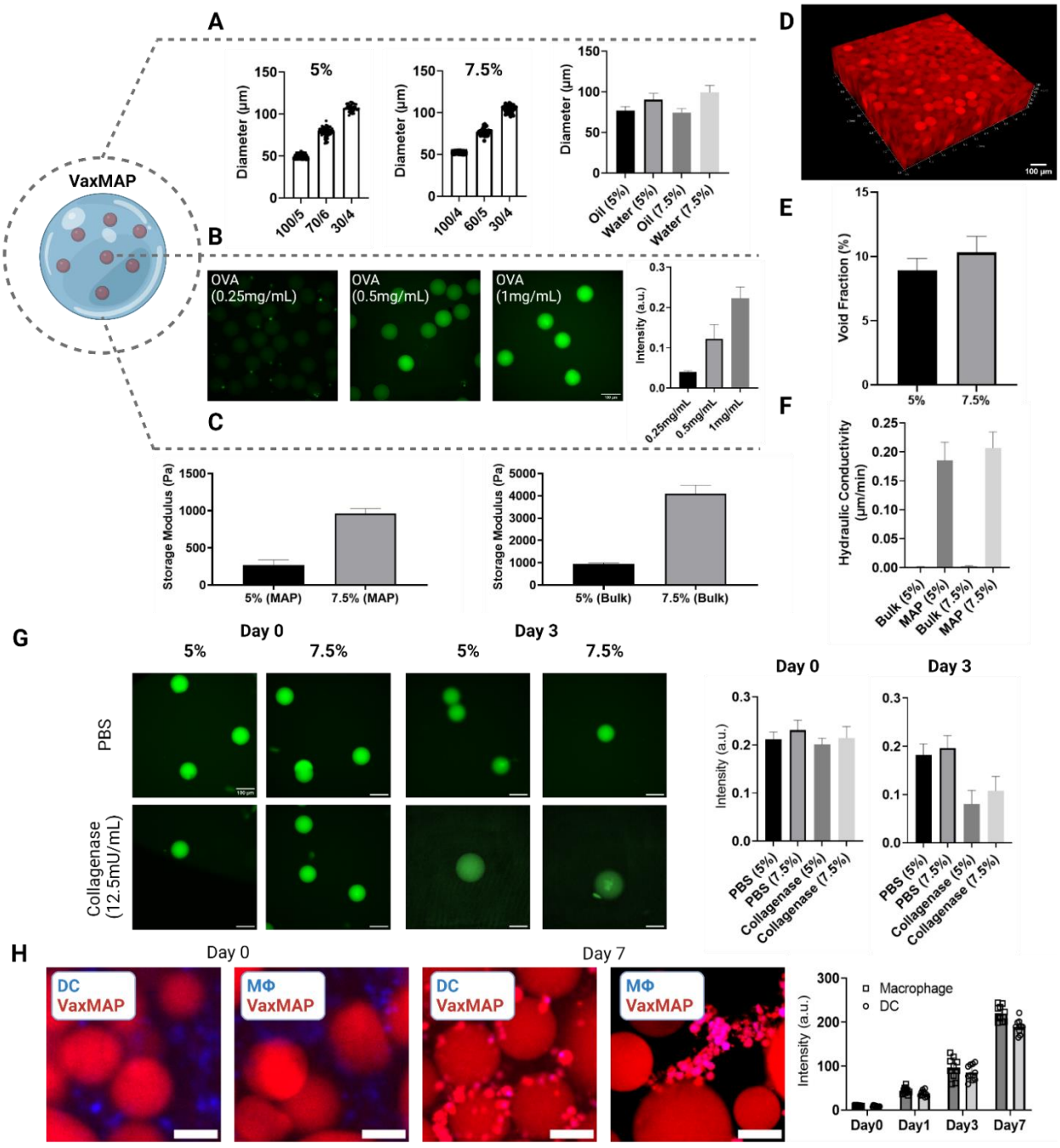

Figure 3-2 Scheme Characterization of VaxMAP building blocks and annealed scaffolds. A) Generation of VaxMAP building blocks with highly defined sizes by altering the aqueous flow rate. Particle size distributions are shown for different ratios of oil to pre-polymer for 5% and 7.5% PEG microgels. VaxMAP building blocks were made with an aqueous flow rate of 6 or 5 μL min−1 for 5% and 7.5% PEG gels respectively, and swollen in buffer after aqueous extraction from the oil phase. B) Representative images of VaxMAP gels loaded with increasing amounts of fluorescently-labeled OVA. With increasing OVA concentration, the fluorescence

signal correspondingly increased. Scale bar: 100 μm C) Stiffness of VaxMAP hydrogels formed in bulk and annealed MAP gel form. Polymer concentration contributes to an increment in stiffness. D) Fluorescence confocal image of a scaffold assembled from monodisperse fluorescently-labeled MAP building blocks. Scale bar: 100 μm. E) Void fraction of annealed MAP scaffolds. F) Hydraulic conductivity of PBS through a nonporous bulk scaffold and annealed MAP scaffold at atmospheric pressure. G) Fluorescent OVA antigen is imaged in microgels over 3 days. Average microgel intensity remains stable in PBS but decreases with collagenase treatment as microgels also swell in size. The scale bar is 100 μm. H) Mouse bone marrow-derived primary macrophages and dendritic cells co-cultured with Alexa Fluor 555-conjugated MAP scaffolds. Over 7 days of culture cells uptake MAP components and cell-associated Alexa Fluor 555 signal increased. Blue: DAPI stain, Red: Alexa Fluor 555. The scale bar is 100 μm. Data are shown as mean ± SD.

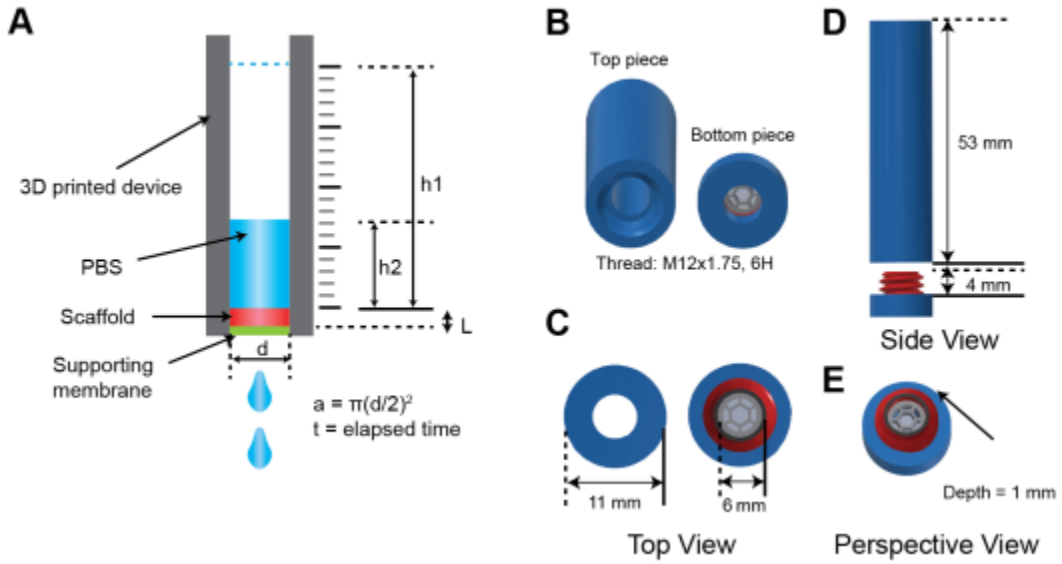

Figure 3-3 Hydraulic conductivity measurement apparatus.
A) Schematic of the hydraulic conductivity measurement using a 3D-printed device. The initial height (h1) and final height (h2) of PBS that flows through the scaffold over an elapsed time were recorded to calculate the overall volumetric flow rate and the conductivity. B) Two components of the 3D-printed device viewed from C) top, D) side and E) perspective.

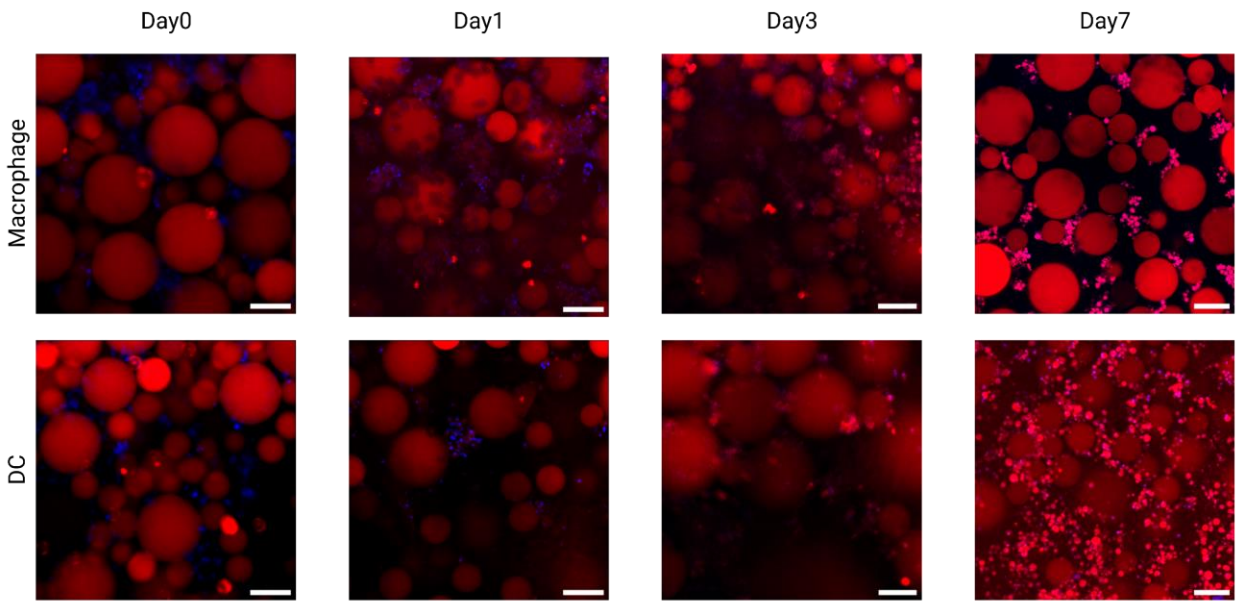

Figure 3-4 In vitro culture of mouse bone marrow derived macrophages and dendritic cells (DCs)
Cells are cultured within 3D MAP scaffolds without antigen over 7 days. As the incubation period increased, MAP-derived fluorescence signal (Alexa Fluor 555-maleimide) accumulated in the cells. Blue: DAPI stain, Red: Alexa Fluor 555. Scale bars are 100 μm.

We found that MAP gels injected and annealed *in vivo* in mice led to activation of $CD4^+$ T cells and B cells resulting in the generation of antigen-specific antibodies, a hallmark of an effective vaccine response. We incorporated NP-OVA, a classical immunological antigen, into MAP to characterize T and B cell responses, including high affinity antigen specific immune responses. C57Bl/6 mice were immunized subcutaneously (s.c.) with MAP microgels (5% PEG) loaded with NP-OVA (MAP-NP-OVA), or the standard aluminum hydroxide-based adjuvant, alum loaded with NP-OVA (Alum-NP-OVA)[106] and compared to unimmunized, PBS injected mice, and activated T and B cells in lymph nodes were assessed 12 days later. MAP-NP-OVA immunization induced similar percentages of activated $CD4^+$ T cells ($CD4^+CD44^{hi}$) and B cells ($B220^+IgD^{lo}$) compared to Alum-NP-OVA (Figure 3-5 B and C). To assess if MAP immunization induces NP-specific antibody responses, we performed anti-NP ELISAs from sera

collected at day 12 after immunization. In general, while both antigen-specific IgG1 and IgG2c antibodies increase following immunization in C57Bl/6 mice, antibodies in mice class-switched to IgG1 correlate with type 2 immune polarization (Th2-biased) of antigen-specific immune cells, while IgG2c responses in C57Bl/6 mice strongly suggest type 1 immune polarization (Th1-biased) of immune cells[107]. MAP-NP-OVA immunized mice displayed modestly higher titers of total anti-NP IgG1 compared to Alum-NP-OVA whereas PBS controls did not display detectable anti-NP antibodies (Figure 3-5 D). Since the immune response following alum immunization typically resolves by 28 days[108], we examined whether the anti-NP antibody responses remained elevated 28 days following immunization with MAP-NP-OVA, Alum-NP-OVA or PBS. Total anti-NP specific antibody titers remained modestly elevated in MAP-NP-OVA immunized mice compared to Alum-NP-OVA (Figure 3-5 E). Neither MAP-NP-OVA or Alum-NP-OVA induced significant anti-NP specific IgG2c responses, consistent with Th2 polarization of antibody responses. In concert, these data demonstrate that vaccination with MAP-NP-OVA induces T and B cell activation and anti-NP antibody responses at least as well an Alum-NP-OVA immunization. Thus, immunization with MAP activates B and T cells to generate and antibody response towards delivered antigens.

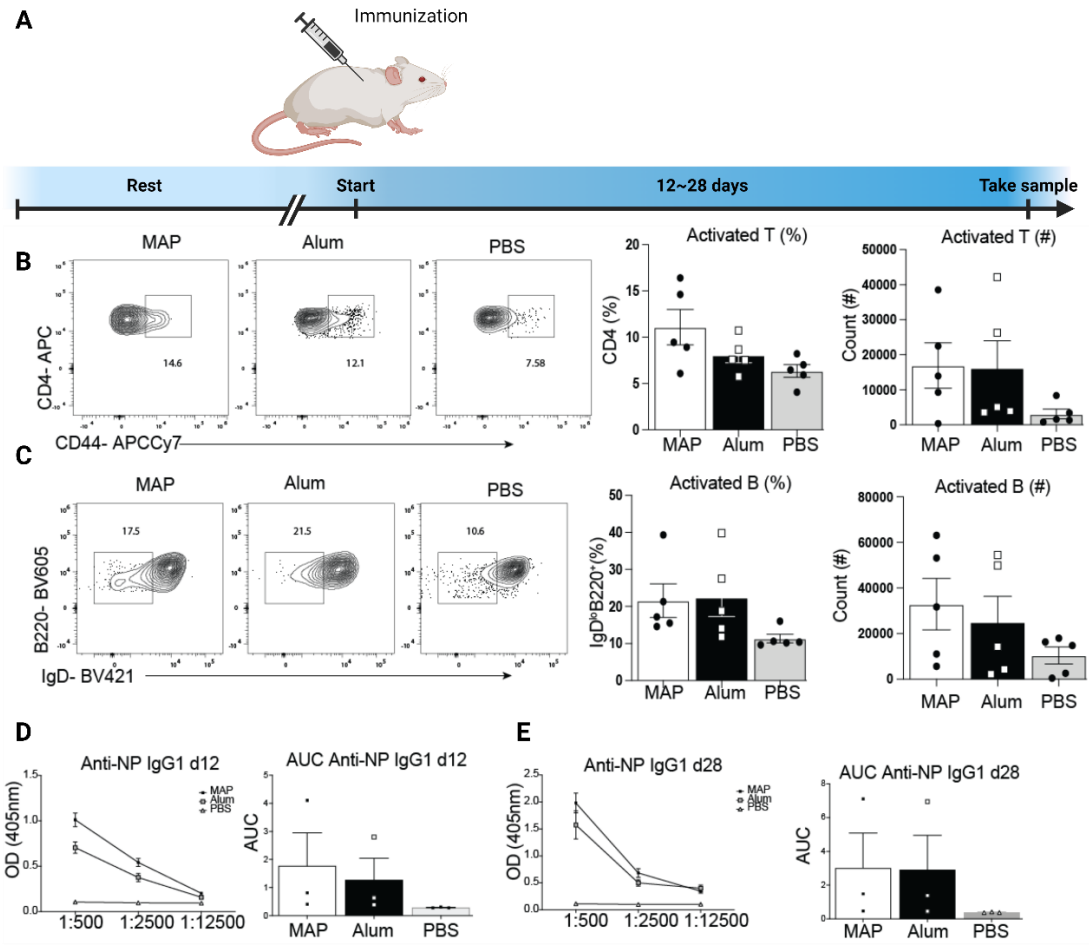

Figure 3-5 MAP vaccination induces robust T cell and B cell activation and anti-NP antibody production.
A) Experimental timeline. B) Representative FACS plots and graphs of percentages and counts of activated CD4+ T cells. C) Representative FACS plots and graphs of percentages and counts of activated B cells. D) Optical Density and Area Under the Curve of anti-NP IgG1 antibodies at 12 days post immunization. E) Optical density and area under the curve of anti-NP IgG1 antibodies at day 28 post immunization.

We next found that MAP-NP-OVA generated high affinity antigen-specific antibody responses that require the development of specific activated Tfh and GC B cells following vaccination. To examine if Tfh and GC B cells develop following MAP injection, C57Bl/6 mice were immunized s.c. with MAP-NP-OVA, Alum-NP-OVA, and PBS and assessed 12 days later.

The percentage and numbers of Tfh cells in draining lymph nodes (LN) trended higher in MAP-NP-OVA immunized mice compared to Alum and PBS injected mice (Figure 3-6 A). In accordance with elevated Tfh cells, the percentage of GC B cells were increased in MAP-OVA immunized mice compared to Alum and PBS injected mice (Figure 3-6 B). Furthermore, consistent with slower antigen release, Tfh and GC B cells remain elevated at 28 days post immunization with MAP-NP-OVA compared to Alum and PBS immunized mice (Figure 3-7). To assess whether the increase in Tfh and GC B cells observed in MAP-NP-OVA injected mice resulted in elevated high-affinity antigen-specific antibodies, we measured the levels of high affinity anti-NP IgG1 antibodies from immunized mice at days 12 and 28. While high affinity antibodies were lower in MAP-NP-OVA immunized mice compared to Alum at day 12 (Figure 3-6 C), the former had elevated titers of high affinity anti-NP IgG1 antibodies by day 28 post immunization (Figure 3-6 D), consistent with a prolonged GC response. Thus, VaxMAP generated a prolonged immune response compared to a traditional vaccine platform.

We next examined whether MAP elicited innate immune cell activation through traditional pathogen- or danger- associated molecular pattern (PAMP or DAMP, respectively) pathways. Since activation of all TLR and inflammasome-interleukin (IL) 1 receptor (IL-1R) pathways require signaling through the adaptors Myeloid differentiation primary response 88 (MyD88) and/or Toll-IL-1R domain (TIR)-containing adapter-inducing interferon-□ (Trif), we immunized B6 and *Myd88*$^{-/-}$*Trif*$^{-/-}$ double knockout (DKO) mice with MAP-NP-OVA. We found that DKO mice displayed a dramatic reduction in antigen specific total and high affinity IgG1 antibodies (Figure 3-8). Since MAP fabrication is done under aseptic techniques but is difficult to keep completely sterile throughout the manufacturing process, we next confirmed that endotoxin contamination did not contribute to the immune response elicited by VaxMAP. We had a low

suspicion of the possibility of endotoxin contamination as contributing to the immune enhancing effects of MAP given that endotoxin activation of TLR4 generally leads to Th1 polarization and IgG2c antibody formation rather than IgG1[109–111]. Nevertheless, we immunized TLR4-mutant C3H/HeJ mice, along with TLR4-wildtype C3H/HeOuJ and C57Bl/6 mice. We observed that unlike DKO mice, C3H/HeJ mice displayed increased antigen-specific IgG1 antibody responses compared to B6 mice, and slightly lower antigen-specific IgG1 when compared to C3H/HeOuJ mice (Figure 3-8). We also routinely find no endotoxin contamination in MAP formulations using other assays (Figure 3-9). Overall, these data illustrate that MAP elicits antibody responses by activating PAMP/DAMP signaling which results in polarizing antibody responses to type 2 antibodies (IgG1).

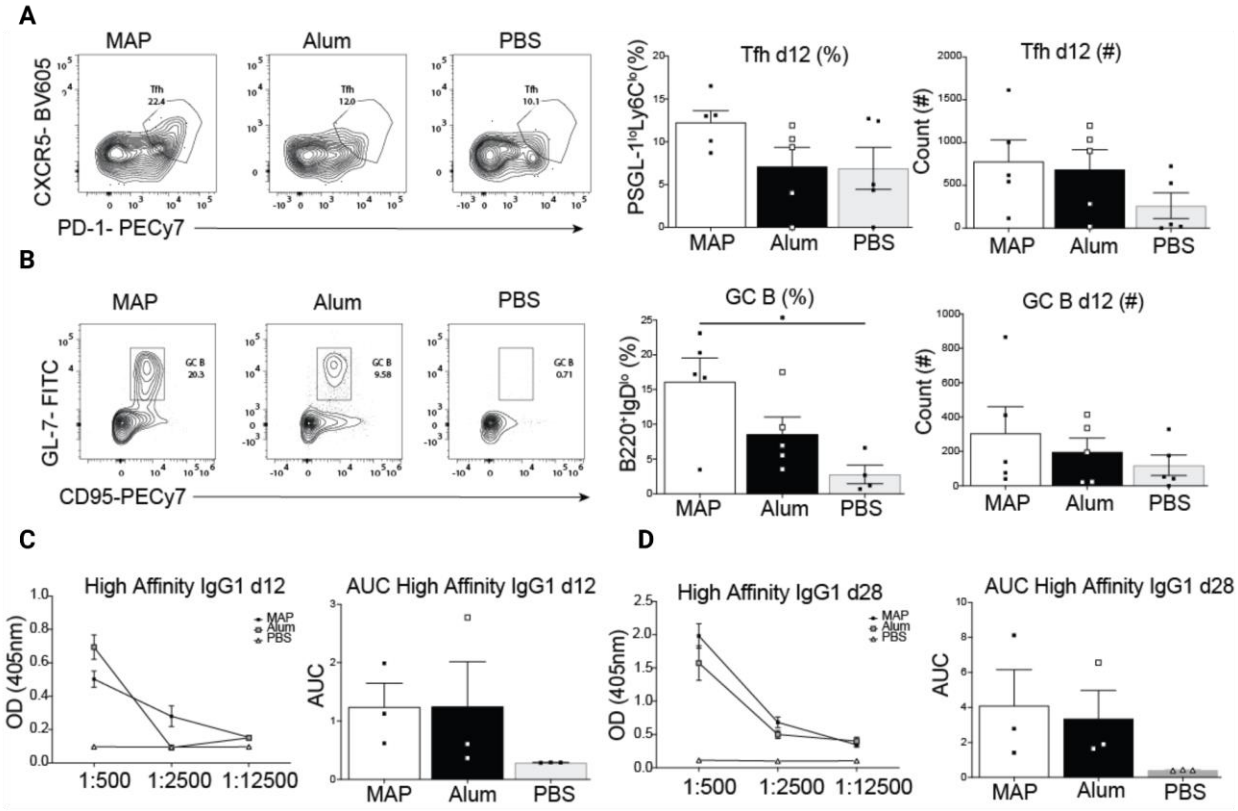

Figure 3-6 MAP vaccination induces Tfh and GC B cell development and production of high affinity antibodies.

A) Representative FACS plots, percentages and counts of Tfh cells at day 12 post immunization. B) Representative FACS plots, percentages and counts of GC B cells at day 12 post immunization. C) Optical density and area under the curve for high affinity anti-NP IgG1 antibodies at day 12 post immunization. D) Optical density and area under the curve of high affinity IgG1 antibodies at day 28 post immunization.

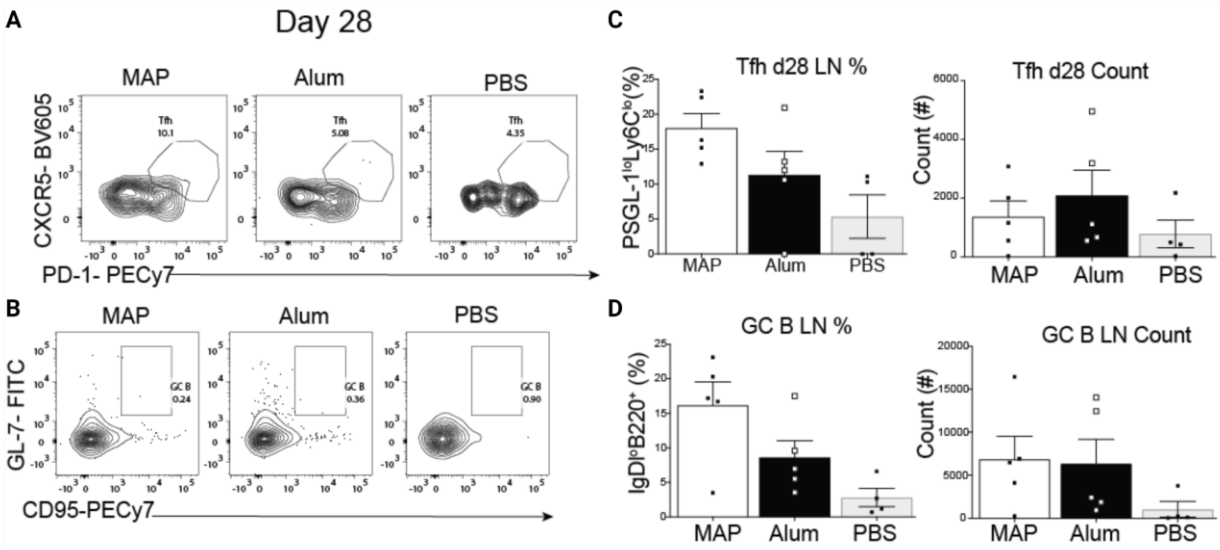

Figure 3-7 Tfh and GC B cell responses at day 28 post immunization from 5% VaxMAP injection.

A-B) Representative FACS plots, percentages and counts of Tfh cells. C-D) Representative FACS plots, percentages and counts of GC B cells.

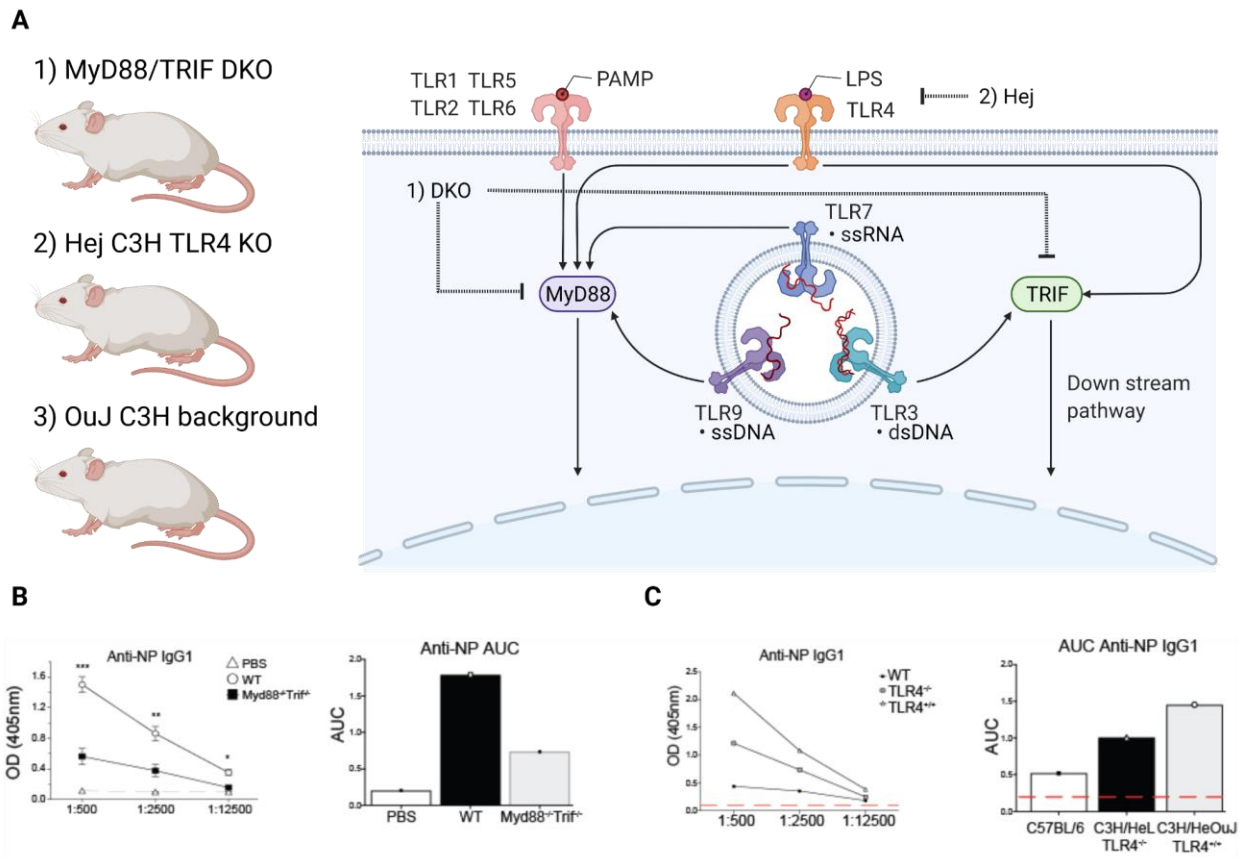

Figure 3-8 MyD88/TRIF DKO, TLR4 KO mice experiments.
A) Schematic of signaling pathway of importance in innate immunity. B) We immunized WT and Myd88-/-Trif-/- mice with NP-OVA MAP. The Myd88-/-Trif-/- mice are devoid of all toll-like-receptor (TLR) and inflammasome signaling as they lack the major adaptors downstream of all TLRs and interleukin-1R. Indeed, Myd88-/-Trif-/- mice demonstrated diminished, but not absent, antibody responses against NP-OVA MAP. C) We tested our VaxMAP in TLR4 mutant C3H/HeJ and WT C3H/HeOuJ mice, since we did not incorporate any known TLR4 agonists into our hydrogel and wished to ensure any adjuvant effect of MAP was not due to endotoxin contamination. Indeed, TLR4 mutant C3H/HeJ mice retained similar levels of anti-NP antibodies to WT mice, confirming that the adjuvant effects of MAP were due to activation of a specific pathogen-associated molecular patterns / pattern recognition receptor (PAMP/PRR) innate immune pathway other than TLR4. Our results suggest that while TLR and/or inflammasome PRR pathways contribute to innate immune responses, other pathways that can be influenced by materials, such mechanosensing pathways, may also contribute and/or fine tune innate immune cell activation to drive antigen-dependent immunity elicited by VaxMAP.

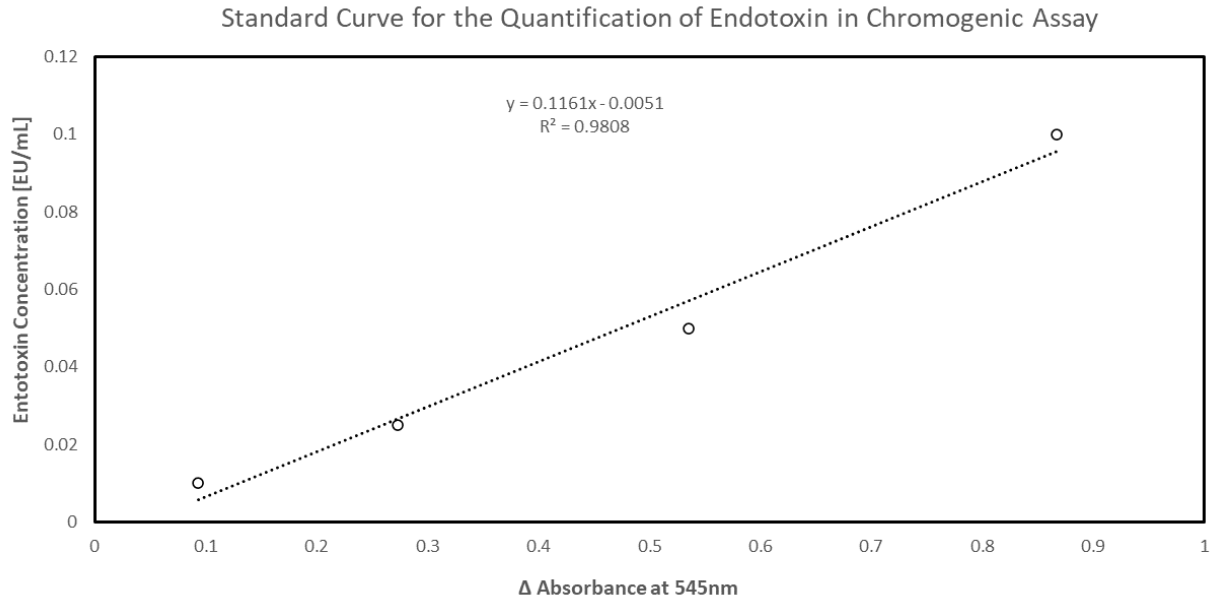

Figure 3-9 Endotoxin assay.
VaxMAP is tested for concentration of endotoxin using an assay kit (Genscript ToxinSensor™ Chromogenic LAL Endotoxin Assay Kit). Fabricated VaxMAPs are mixed with ToxinSensor reagents and absorbance at 545nm is measured to confirm endotoxin concentration was less than 0.01 EU/mL before animal testing. Standard curve is shown to calibrate threshold levels.

We next modulated hydrogel crosslinking density and stiffness to tune the subsequent quality of the antigen-specific antibody response. To examine if more highly crosslinked MAP formulations regulate the immune response, we immunized C57Bl/6 mice with either 5% or 7.5% MAP-NP-OVA and assessed T and B cells and antibody responses 12 days post injection. The stiffer 7.5% MAP gel induced enhanced $CD4^+$ T cell activation as well as Tfh cell development compared to the 5% MAP formulation (Figures 3-10 A and B). Despite the 7.5% MAP gel having reduced activated B cell percentages (Figures 3-10 C), GC B cells were increased compared to the 5% MAP (Figures 3-10 D). We next tested whether the different MAP formulations altered low and high affinity anti-NP IgG1 antibody titers. The 7.5% MAP formulation induced significantly higher levels of both total and high affinity anti-NP IgG1 antibodies compared to 5% MAP (Figures 3-10 E and F).

We next wished to determine whether enhancing the stiffness of the hydrogel further could further enhance the antibody response. To accomplish this, we increased cross-linking density further by incorporating NP-OVA into 7.5% MAP cross-linked with a PEG-diothiol crosslinker rather than an MMP cross-linker. This resulted in an increased stiffness when compared to the 7.5% MAP with MMP crosslinker (Figure 3-11). When mice were immunized with this MAP formulation, we found that both total and high affinity anti-NP specific antibody production was further enhanced, but only slightly. While the PEG crosslinked hydrogel led to slightly better antibody responses, three of the mice developed scratching behavior and ulcerations over the injection site, either due to the uncomfortable nature of the stiffer hydrogel or possibly due to the more intense immune response in the area. Given their ability to induce a nearly maximal antigen-specific antibody production without causing any obvious undesired side effects, the 7.5% MMP crosslinked gels were chosen as the preferred formulation for future studies.

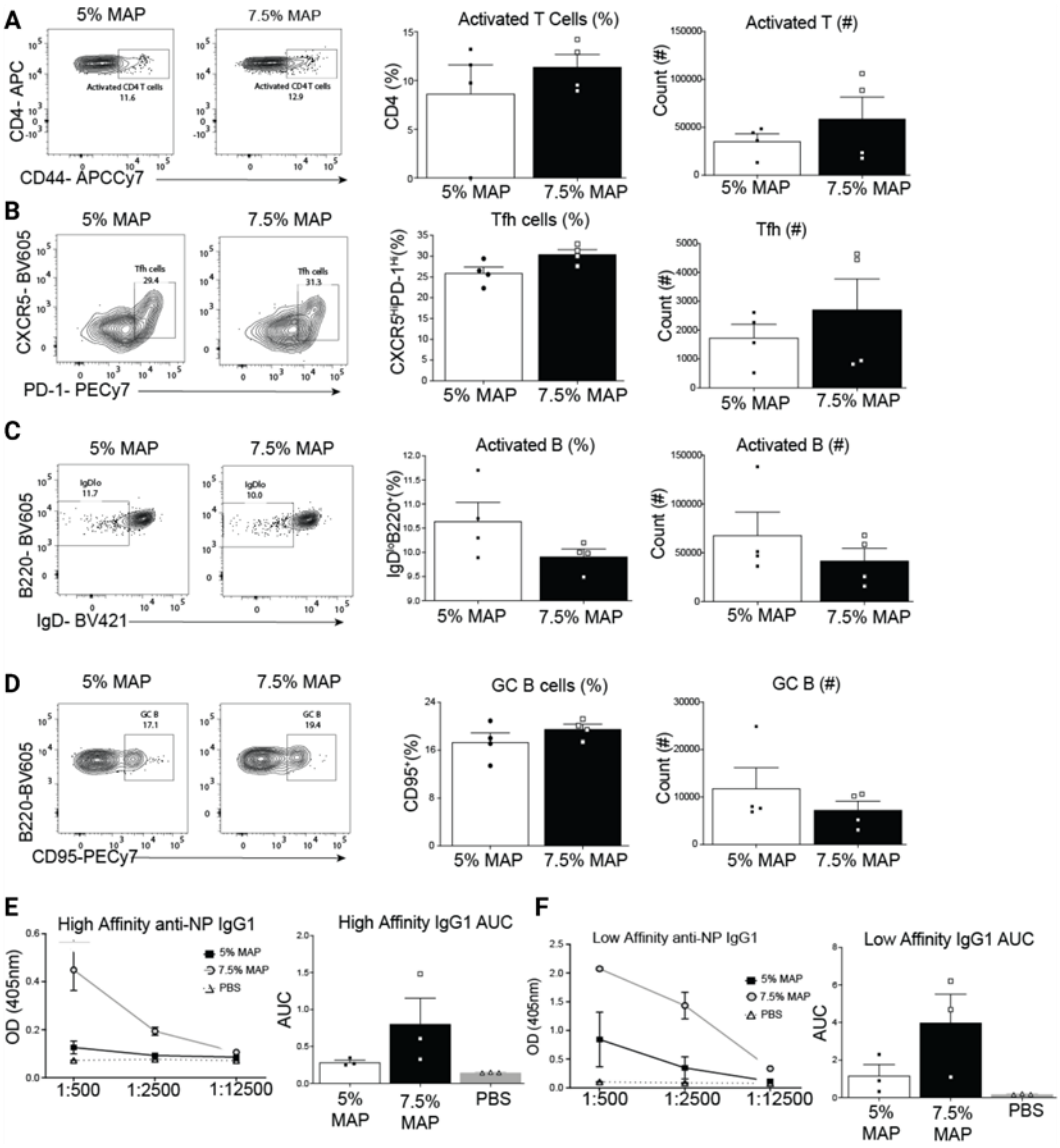

Figure 3-10 Stiffer VaxMAP formulation induces a more robust adaptive immune response 12 days after immunization.

A) Representative FACS plots, percentages and counts of activated T cells between 5% and 7.5% MAP formulations. B) Representative FACS plots, percentages and counts of activated B cells between 5% and 7.5% MAP formulations. C) Representative FACS plots, percentages and counts of Tfh cells between 5% and 7.5% MAP formulations. D) Representative FACS plots, percentages and counts of GC B cells between 5% and 7.5% MAP formulations. E) Optical density and area under the curve of high affinity anti-NP IgG1 antibodies. F) Optical density and area under the curve for low affinity anti-NP IgG1 antibodies.

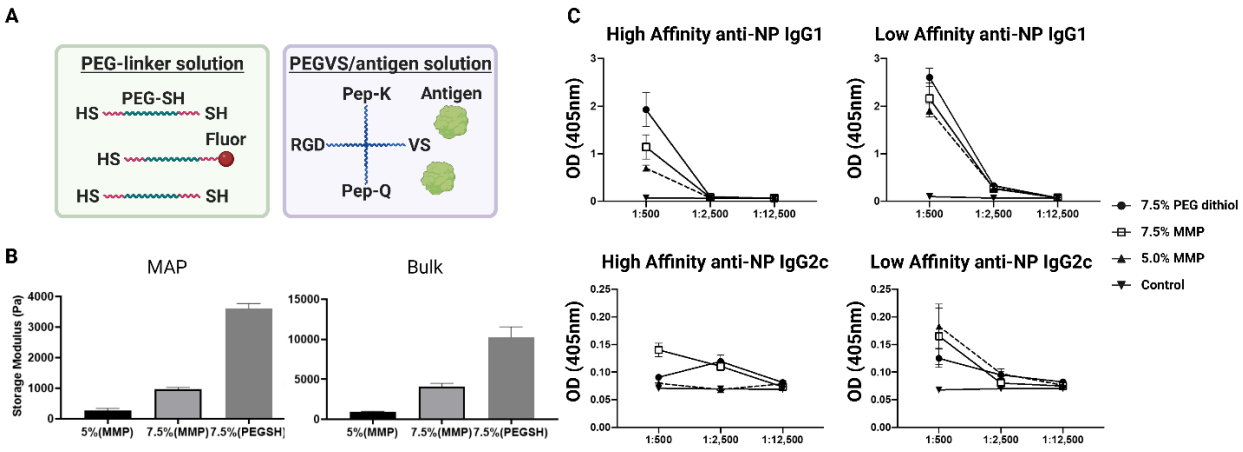

Figure 3-11 Effect of MAP gel formulation on high and low affinity antibody titers. A) MAP microgels produced with 4-arm PEG-vinylsulfone (PEG-VS) via thiol-ene reactions to encapsulate antigen in the dense gel mesh. PEG dithiol was used as a crosslinker to enable microparticle formulations with higher stiffness than MMP crosslinkers. B) Stiffness of PEG dithiol crosslinked gels formed in bulk and annealed MAP gel form. PEG dithiol crosslinking resulted in more than 2-fold increased stiffness than the 7.5% MMP crosslinked condition. C) Optical density of high affinity (NP-9) and low affinity (NP-27) anti-NP IgG1 and IgG2c antibodies at 14 days post immunization. PEG represents PEG dithiol crosslinked condition. PEG dithiol was crosslinked with 7.5% of PEG-VS. 7.5% and 5% MAP represented MMP crosslinked conditions.

While NP-OVA is an advantageous system for dissecting immune responses, it is not naturally expressed by pathogens and does not reflect the ability to confer protection against infection. Using the 7.5% MAP formulation, which led to increased antibody titers, we next evaluated the ability to introduce whole inactivated virus from the mouse-adapted influenza strain (PR8) into MAP (MAP-flu), compared to the same particles delivered in Alum (Alum-flu) or PBS (PBS-flu). C57Bl/6 mice were immunized with MAP-flu, Alum-flu, or PBS-flu as a control and immune responses were examined 12 days following injection. We found that MAP-flu drove the development of activated T cells greater than PBS controls (Figure 3-12 B). Additionally, MAP-flu induced a significantly higher percentage of Tfh cells than Alum-flu or PBS-flu immunized mice (Figure 3-12 C). In a similar manner, MAP-flu immunization induced

modest activation of B cells and GC B cell development (Figures 3-12 D and E). Anti-hemagglutinin (HA) IgG antibody responses were increased in mice receiving MAP-flu compared to PBS immunized controls (Figure 3-12 F). To assess if MAP-flu immunization elicits protection against influenza infection, C57Bl/6 mice were immunized with either MAP-flu, Alum-flu, PBS-flu, or PBS alone. Sixty days later, these mice were challenged with a high dose of PR8 influenza. Mice immunized with MAP-flu failed to lose weight and demonstrated enhanced survival relative to PBS-flu and PBS immunized mice (Figures 3-12 G). Overall, these data demonstrate that MAP-flu immunization elicit protection against a subsequent influenza infection.

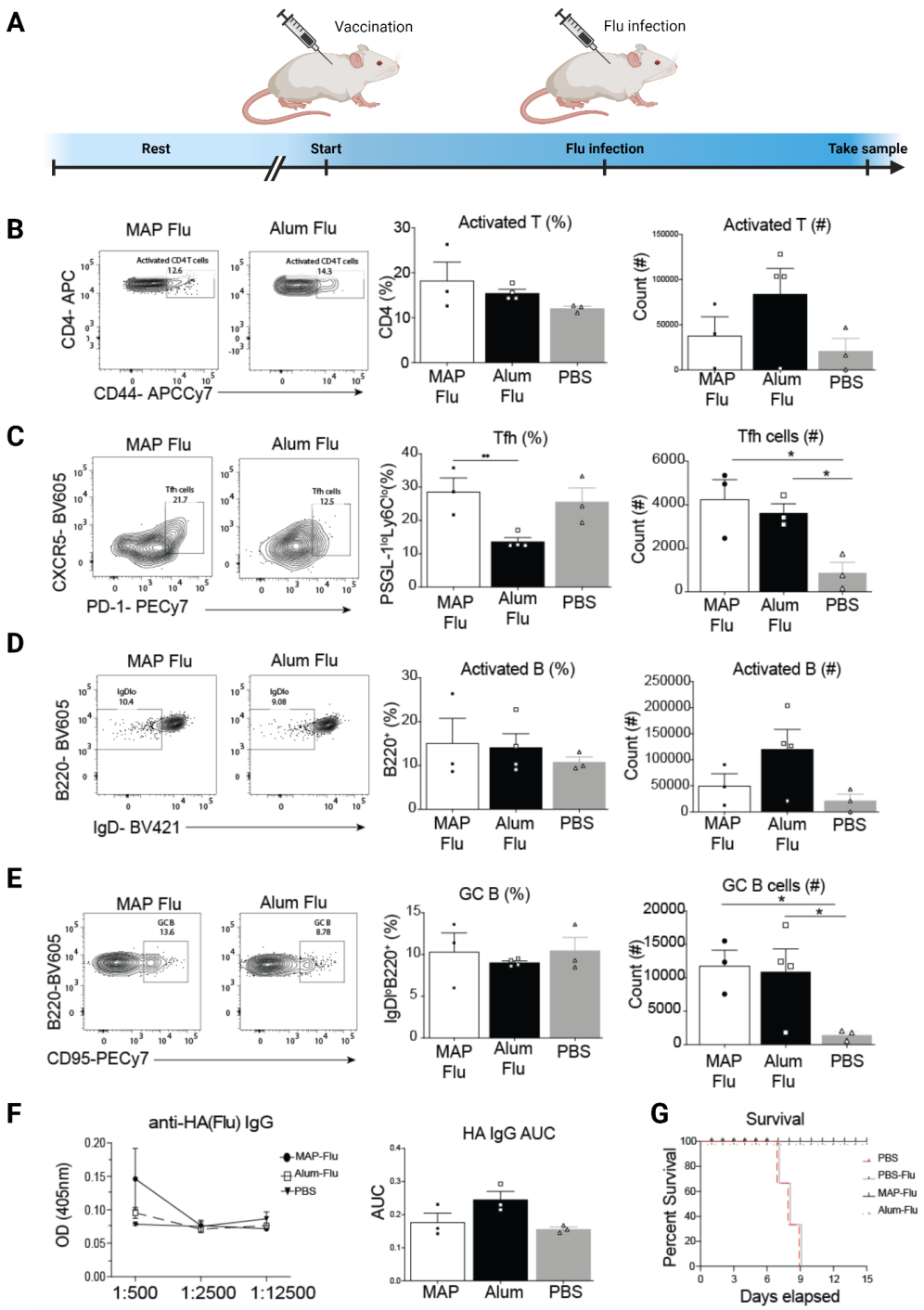

Figure 3-12 MAP is an effective vaccination platform against PR8 influenza infection.
A) Experimental timeline. B) Representative FACS plots, percentages and counts of activated T cells of immunized mice. C) Representative FACS plots, percentages and counts of Tfh cells of immunized mice. D) Representative FACS plots, percentages and counts of activated B cells. E) Representative FACS plots, percentages and counts of GC B cells. F) Optical density and area

under the curve of anti HA IgG antibodies. G) Survival curve of immunized mice following PR8 influenza rechallenge 60 days following immunization.

3.3. Conclusion

In this study, we demonstrate that in comparison to Alum, VaxMAP can function as a robust immunization platform for either protein-based or inactivated pathogen-based immunogens, two traditional vaccine types commonly used to vaccinate patients against a variety of viral and bacterial pathogens. Further, by simply changing the weight % of PEG and/or changing the crosslinking peptides, without adding cytokines, growth factors, or PAMPs, DAMPs or other adjuvants, we were able to fine-tune immune responses leading to improved antigen specific antibody responses, without affecting polarization of immunity from type 2 to type 1 immune responses. Immunization with VaxMAP drives activation of CD4+ T cells and B cells, as well as their differentiation to Tfh and GC B cells, respectively. These immune cells are critical regulators of germinal center responses, which lead to the generation of long-lived memory B cells and plasma cells, required for long-lived protection against pathogens. Finally, we show that immunizing mice with 7.5% VaxMAP loaded with inactivated influenza virus completely protected mice against a lethal influenza viral challenge 60 days after vaccination, demonstrating VaxMAP-based immunizations can serve as functional vaccines.

Immunologically instructive biomaterials have shown potential as novel vaccination platforms. Most vaccine adjuvant platforms, including the promising mesoporous silica nanoparticle platform and the recently FDA-approved Matrix M platform, are based on nanoparticles that do not have cell-scale porosity[112–114] . Biomaterials with macroscale porosity that allow rapid cellular infiltration are being recognized for their potential to modulate immune

responses in tissue regeneration, cancer immunotherapy, and immune-tolerance applications, but their ability to generate immune responses in traditional vaccine settings remains incompletely explored. Super et al. recently demonstrated the ciVAX platform using mesoporous silica particles coupled with the TLR4 agonist lipid A and a Fc-mannose-binding lectin to bind bacterial components to protect mice from bacterial infections[100]. This platform demonstrated the ability to promote antibody production, decrease bacterial burden, and prevent mortality, but whether the protective effects could be produced by the biomaterial itself, or the numerous factors added to the biomaterial is unknown. Our work provides evidence that a biomaterial alone can provide the necessary signals to induce Tfh and GC B cells, protective antibodies, and protection against lethal infection. In fact, the biomaterial-induced immune response is tunable, and we demonstrate that altering material crosslinking density is sufficient to generate more robust antibody responses. Future studies may uncover whether modulation of other material cues, such as adhesion peptide concentration, adhesion peptide sequence tuned to recruit specific immune cells[115] or biomaterial composition alter response to type 1 immune polarization rather than type 2 immune polarization[116]. Thus, our study provides support for the use of a modular injectable biomaterial to directly induce protective immune responses for vaccine applications.

3.4. Materials and Methods

Microfluidic Device Fabrication

Droplet generating microfluidic devices were fabricated by soft lithography as previously described[10]. Briefly, master molds were fabricated on silicon wafers (University wafer) using two-layer photolithography with KMPR 1050 photoresist (Microchem Corp). The height for the droplet formation channel was 50 μm, and the height for the collection channel was 150 μm.

Devices were molded from the masters using poly(dimethyl)siloxane (PDMS) (Sylgard 184 kit, Dow Corning). The base and crosslinker were mixed at a 10:1 mass ratio, poured over the mold and degassed before curing overnight at 65 °C. Channels were sealed by treating the PDMS mold and a glass microscope slide (VWR) with oxygen plasma (Plasma Cleaner, Harrick Plasma) at 500 mTorr and 80 W for 30 s. Thereafter, the channels were functionalized by injecting 100 μL of Aquapel (88625-47100, Aquapel) and reacting for 30 s until washed by Novec 7500 (9802122937, 3M). The channels were dried by air suction and kept in the oven at 65 °C until used.

Microgel Production

Monodisperse microgels were produced as follows. Two aqueous solutions were prepared: i) 4 Arm-PEG VS (PTE-200VS, JenKem) at 10% and 15% (w/v) in 0.3 M triethyloamine (TEOA) pH8.5, pre-reacted with K-peptide (Ac-FKGGERCG-NH2), Q-peptide (Ac-NQEQVSPLGGERCG-NH2) and with RGD peptide (Ac-RGDSPGERCG-NH2) with 1mg/mL NP-ova and ii) an di-cysteine modified matrix metallo-protease sensitive peptide (MMP) (Ac-GCRDGPQGIWGQDRCG-NH2) (Genscript). These pre-gel solutions were sterile-filtered through a 0.2 μm polyethersulfone (PES) membrane in a luer-lok syringe filter, injected into the microfluidic device and pinched off by oil phase (0.1% Pico-Surf in Novec 7500, SF-000149, Sphere Fluidics) (Figure S1, Supporting Information). The flow rate for aqueous solutions was 4–6 μL min−1 and for oil solutions was 30–100 μL min−1 to fine-tune the size of droplets. Gels were collected from the device into a tube in oil phase, incubated overnight at room temperature in dark. Microgels in oil phase were vortexed with 20% 1H,1H,2H,2H-Perfluoro-1-octanol (PFO) (370 533-25G, Sigma-Aldrich) in Novec 7500 for 10 s. Microgels were then mixed with

1:1 mixture of HEPES buffer (100 × 10−3m HEPES, 40 × 10−3m NaCl pH 7.4) and hexane followed by centrifugation at 10,000 rpm to separate microgels from oil for five times. Microgels were incubated in sterile-filtered 70% ethanol solution at 4 °C at least overnight for sterilization. Before in vivo or in vitro experiments, microgels were washed with a HEPES buffer with 10 × 10−3m CaCl2 for five times.

Annealing of Microgels

Equal volumes of two microgel solutions were incubated in HEPES-buffered saline (pH 7.4) containing FXIII (10 U mL−1) or thrombin (2 U mL−1) respectively at 4 °C overnight. The two solutions were centrifuged at 10,000 rpm for 5 min and supernatants were removed to concentrate the microgels. These concentrated solutions were thoroughly mixed with each other by pipetting up and down, pipetted into a desired location and kept at 37 °C for 90 min to anneal the microgels into a MAP scaffold.

Rheology Techniques for Measuring the Storage Modulus of MAP Blocks

The storage modulus of an 8 mm disc gel was measured using an Anton paar physica mcr 301 Rheometer. 40 μL of pre-gel solutions (20 μL of PEG with peptides, 20 μL of crosslinker) were pipetted onto sterile siliconized (Sigmacote; SL2-25ML, Sigma-Aldrich) slide glass, covered with another glass with 1 mm spacer and incubated at 37 °C for 2 h. Disc gels were swollen to equilibrium in PBS overnight before being measured. An amplitude sweep (0.01–10% strain) was performed to find the linear amplitude range for each. An amplitude within the linear range was chosen to run a frequency sweep (0.5–5 Hz). At least four disc-gels were measured for each condition.

Void Fraction of MAP Scaffolds

Fully swollen and equilibrated MAP building blocks (20 μL) were activated by with 5 U mL−1 FXIIIa (Sigma) and 1 U mL−1 thrombin, and the mixture was pipetted into a 3 mm diameter PDMS well on a glass coverslip and annealed in a humidified incubator at 37 °C for 1.5 h to form porous MAP scaffolds. Thereafter, the scaffolds were placed into HEPES buffer (pH 7.4) with 70 kDa dextran-FITC (FD70S-100MG, Sigma-Aldrich) overnight to reach equilibrium. Samples were 3D imaged using a Leica TCS SP8 confocal microscope with 10× objective.

Hydraulic Conductivity Measurement in the Scaffold

A custom-designed device was designed using Autodesk Inventor 3D CAD software and printed in Watershed XC 11 122 Normal-Resolution Stereolithography built in 0.004” layers from Proto Labs, Inc. (Figure S2, Supporting Information). For the MAP scaffold, 25 μL of microgel building blocks (5 or 7.5 wt% crosslinked with MMP-cleavable dithiol) was casted on top of a 5 μm pore size cellulose membrane (SMWP01300, Fisher Scientific) in the bottom plane of the device and annealed followed by the overnight incubation in PBS. For the nonporous scaffold, 10 μL of pre-gel solution was casted on top of the membrane in the device and incubated at 37°C for 2 h followed by the overnight incubation in PBS. Then 1 mL of PBS with blue food dye was injected into the device and the permeated volume over time was measured. The hydraulic conductivity was calculated based on Darcy’s law.

Antigen release from MAP gel

FITC conjugated Ovalbumin (Invitrogen) as surrogates for hydrogel degradation and antigen release from hydrogels after a 3-day incubation in PBS and collagenase solution at the different concentrations.

Bone Marrow Derived Macrophage and Dendritic Cell Culture in MAP scaffold

Bone marrow was harvested from C57BL/6J (B6) mice. Macrophages were differentiated using CMG media. Dendritic Cells were differentiated using 20 ng/mL Recombinant Murine GM-CSF (Peprotech) and 10 ng/mL IL-4 (Peprotech). Cells were collected at Day 6 for in vitro assays. Collected cells were mix with MAP gel scaffold and co-cultured for a week. Before microscope observation, cells were stained by Hoechst 33342 Solution (Thermo Fisher Scientific).

Mice

Mice were housed in pathogen-free conditions at the Rutgers New Jersey Medical School or UCLA. C57BL/6J (B6) were purchased from NCI managed colony at Charles River or Jackson Laboratories. All animals were ages 6–12 weeks during the course of the study, with approval for procedures given by the Institutional Animal Care of Rutgers New Jersey Medical School or UCLA. Both male and female mice were used in these studies.

VaxMAP Injection

For VaxMAP injection the same volume of HEPES buffer is mixed with MAP microgels. Excess supernatant is removed as much as possible. A Factor XIII and thrombin solution in the ratio of 6U Factor XIII/1.2 U thrombin solution is made in 200 µL HEPES buffer and added to MAP microgels in the ratio of 1mL gel to 200µL Factor XIII/Thrombin. Final MAP microgel solution

is loaded into a Hamilton GasTight syringe and injected s.c. at the base of the tail with a 25G needle.

Flow Cytometry and Cell Sorting

Tissues were homogenized by crushing with the head of a 1-ml syringe in a Petri dish followed by straining through a 40-µm nylon filter. Ammonium–chloride–potassium buffer was used for red blood cell lysis. To determine cell counts, count beads were used at a concentration of 10,000 beads/10μL and added directly to samples following staining. Cell count is normalized by dividing input bead count by cytometer bead count, and multiplied by the dilution factor. Antibodies used for flow cytometry staining are listed in Table S1. Staining for CXCR5 was performed at room temperature (25°C) with 30 min of incubation. Stained and rinsed cells were analyzed using a multilaser cytometer (LSRII; BD Biosciences or Attune; Invitrogen).

Influenza Infections

Mice were anesthetized with 87.5mg/kg Ketamine/ 12.5 mg/kg Xylazine cocktail in 200µL of PBS prior to infection. Mice were infected intranasally with 30µL of 0.5LD50 influenza PR8 in PBS using a p200 pipette. Animals were sacrificed at indicated time points p.i. and harvested organs were processed for flow cytometry.

ELISA Assays

Anti-NP antibodies in mouse sera were measured on Nunc PolySorp 96 well plates (Thermo Fisher) coated with NP-9 or NP-27 protein in carbonate buffer (Sigma). Alkaline phosphatase-conjugated anti-mouse IgG antibodies (Southern Biotech) and phosphatase substrate (Sigma)

were used for detection. ODs were read at 405 nm on a SpectraMax Microplate Reader (Molecular Devices).

Statistical Analysis

Data were analyzed using Student's t-test, Mann-Whitney unpaired t-test, and Pearson correlation coefficient with GraphPad Prism 8 Software.

Chapter 4. Effects of Hyaluronic Acid Molecular Weight on Cells Involved in Neural Repair and Neuroinflammation

Tissue in the CNS lacks the ability to heal properly after SCI due to the complex pathophysiology. The combination of chronic inflammation, glial scarring, and BSCB permeability create an inhibitory environment for regeneration. Any successful therapeutic for SCI must address these issues by promoting angiogenesis, resolving chronic inflammation, regenerating neural tissue, and integrating with host tissue. Hydrogels have been employed to accomplish those goals. However, in order for them to accomplish them, there are a few design criteria that need to be considered including injectability, biocompatibility, biodegradability, interactivity, porosity, and swelling. With that in mind, HA is an ideal base for hydrogels because it is nonimmunogenic and has multiple chemical groups that can be easily functionalized using aqueous, biocompatible chemistries to create crosslinking sites[117]. Despite these encouraging findings, these studies also found poor integration of implanted HA hydrogels with host tissues, including sparse infiltration of regenerating axons[118,119]. However, Ehsanipour et al. developed a HA-based hydrogel platform with cell-scale macropores that promoted robust cell infiltration and increased host tissue integration[120]. These microporous annealed HA microparticle scaffolds will be employed in the studies presented in this dissertation. While HA-based hydrogels have shown promising results for SCI treatment, there is still one major gap in the knowledge base. HA exhibits a MW-dependent bioactivity in vivo that is not yet fully understood or characterized. In this section, we characterized HA dependent tissue regeneration.

4.1. Introduction

As mentioned in previous chapters, there is currently no treatment for spinal cord injury (SCI) that can fully restore function. One promising approach, however, is the use of hyaluronic acid (HA)-based hydrogels[117,121]. HA hydrogels have been widely studied and have low immunogenicity, maintain high water content (>90%), have tunable mechanical properties that can mimic nerve tissue (1-10 kPa Young's modulus), and are compatible with injection into the spinal cord[118,122],. Injectable hydrogels are optimal for SCI as the injuries are often incomplete, requiring a minimally invasive approach to spare surviving neural tissue[120,123,124]. Additionally, HA-based hydrogels have been shown to significantly reduce secondary injury, specifically inflammation and glial scar deposition, while also promoting neural stem cell (NSC) survival, proliferation, and migration, wound healing, and angiogenesis[125,126]. This chapter will focus primarily on the ability of HA-based hydrogels to promote angiogenesis. After SCI, some repair occurs in the lesion site, however, it is severely limited by the hostile and inhibitory environment that is created in the chronic phase by events during the acute/subacute phases including the lack of a blood-spinal-cord-barrier (BSCB,) such as ischemia, immune cell infiltration, accumulation of reactive oxygen species, and edema as a result of hemorrhaging[127–129]. Promoting angiogenesis, the formation of new blood vessels through endothelial cell (EC) sprouting from pre-existing vessels, has been shown to improve outcomes after SCI. Re-vascularization of the lesion site provides a conducive microenvironment essential for nerve repair. By re-establishing BSCB integrity and restoring blood supply to the injury site, secondary damage can be attenuated[129] which is the primary goal of these therapeutic strategy. Several studies have shown the ability of HA-based hydrogels to promote angiogenesis after CNS injury. Wen et al. used a tubular HA hydrogel mixed with poly(lactic-co-glycolic acid) (PLGA) microspheres loaded with brain-derived neurotrophic factor (BDNF) and vascular endothelial growth factor (VEGF) to

treat rats with a thoracic dorsal hemisection SCI and found a large number of new blood vessels within the injury site[126]. Lu et al. found that an HA-based hydrogel immobilized with the VEGF-mimetic peptide KLT enhanced angiogenesis in a traumatic brain injury model in rats. While the angiogenic ability of HA-based hydrogels has been highlighted before, one key variable that has yet to be fully explored is how the molecular weight (MW)-dependent bioactivity of HA influences the regenerative capacity of HA-based hydrogels. As mentioned in previous chapters, HA exhibits a MW-dependent bioactivity. The protective role of HMW HA, as well as its ability to promote more stable tube formation, in human cerebral microvascular endothelial cells (HCMVECs) was highlighted. Additionally, the data presented also suggests CD44 clustering as a potential mediator of this MW-dependent bioactivity. In this chapter, the role of HA MW in HA-based hydrogels will be investigated, specifically through CD44 clustering and angiogenesis in HCMVEC cultures. This study highlights the importance of considering HA MW in the design of HA-based biomaterials, demonstrating that the MW-dependent bioactivity is conserved after chemical modification and crosslinking into biomaterials.

4.2. Result and Discussion

To characterize the effects of HA MW on HCMVEC cell health, we evaluated the viability, apoptosis, and proliferation of HCMVECs 24 hours after treatment with 1 mg/ml HA of varied MW. For viability and apoptosis, the ApoLive-Glo™ Multiplex Assay was used to obtain measurements of the relative fluorescent and luminescent signals, respectively. Data is reported as the ratio of relative fluorescent units (RFU), or viability signal, to relative luminescent units (RLU), or apoptotic signal (Fig 1A). The ratio of viable-to-apoptotic cells (RVAC) decreases as HA MW decreases, and all conditions have a much lower ratio than the

positive ECMC control. Since ECMC includes the endothelial cell growth supplement (ECGS), and other conditions do not, this difference is not surprising. Using a Kruskal-Wallis test and Dunn's multiple comparisons test, we report that 1M HA promotes a statistically significant ($p < 0.05$) increase in RVAC compared to 40K, 10K, and No HA conditions (Figure 4-1 A). Interestingly, after measuring the percentage of cells that are proliferative using an EdU assay, we found no statistically significant differences between any of the HA MW conditions or controls (Figure 4-1 B). This data together suggests a possible protective role for HMW HA in the microvasculature of the CNS. Conventionally, it is thought that LMW HA promotes EC proliferation and angiogenesis and that these functions are specifically inhibited by HMW HA. Lokeshwar et al. showed that this response is origin dependent as lung microvascular ECs were more proliferative in the presence of HMW HA. In the data presented, there were no significant differences in proliferation of HCMVECs in the presence of varying HA MWs. It would be beneficial in future studies to investigate the differences in HA MW-dependent bioactivity of microvascular ECs originating from different tissues. Furthermore, Al-Ahmad et al. showed that ultra-LMW HA (<6.5 kDa) decreased cell viability and density in response to HMW HA (>950 kDa). Given the prominence of HMW HA in the central nervous system (CNS) ECM and the blood-spinal-cord-barrier (BSCB) glyocalyx, the reported data suggests a protective role for HMW HA in HCMVECs.

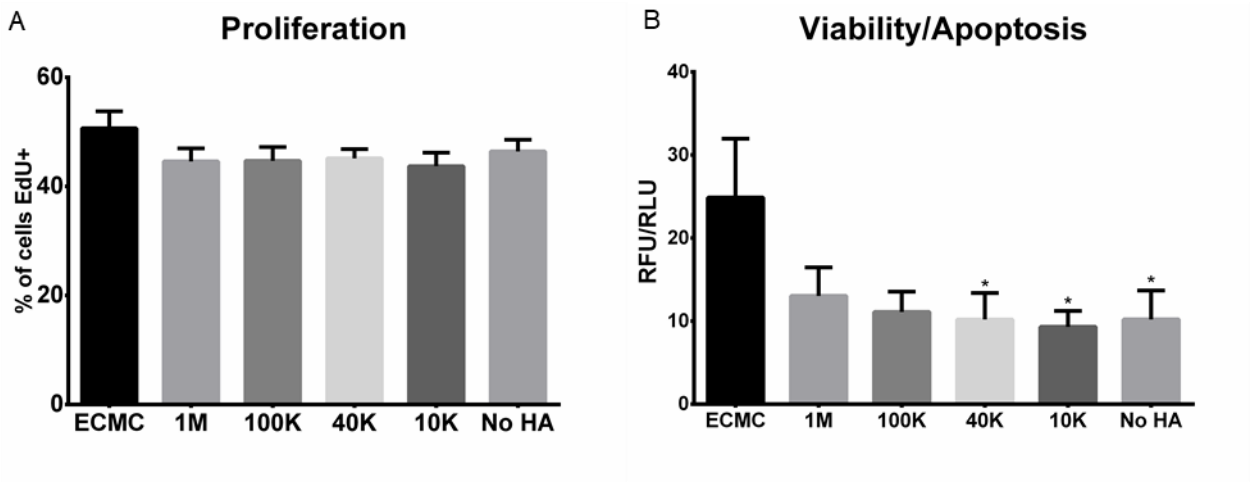

Figure 4-1 HCMVECs in different MW HA
Human cerebral microvascular endothelial cells (HCMVECs) were treated with 1 mg/ml HA with MW ranges of 750-1000 kDa (1M), 100-150 kDa (100K), 41-65 kDa (40K), or 10-20 kDa (10K). As a positive control, HCMVECs were cultured in endothelial cell media complete with an endothelial cell growth supplement (ECMC) or endothelial cell media without the growth supplement or HA (No HA). Cell health was characterized by proliferation (A) and the ratio of viable to apoptotic cells (B). All graphs are showing mean with standard deviation. Fig 1A has n=9 for all conditions. Fig 1B has n=33 for ECMC, 40K, and 10K, n=35 for 1M and 100K, and n=32 for No HA. One-way ANOVA and Kruskal-Willis test were performed. The "*" symbol is used to denote significance compared to 1M.

The primary function of ECs is to form and maintain functional blood vessels. In order to understand the effects of HA MW on the angiogenic behavior of ECs, the ability to form tubular structures must be characterized. Using a Geltrex™ tube formation assay and time lapse microscopy, we were able to track tube formation of HCMVECs, measured as total tube length which is the straight-line length of all tubes combined. The data reported shows the ability of 1M HA to promote more stable tube formation in HCMVECs, as the total tube length value decreased at a slower rate than other conditions (Figure 4-2). In tracking tube formation from 400 to 1020 minutes, the 1M HA treated cells maintained the largest total tube length values along with 10K HA (Figure 4-2). However, after interrogating specific time points (8, 12, and 16 hours), only the mean tube length of 1M HA treated cells had statistically significant differences

compared to other HA MW conditions using a Dunnett's multiple comparisons test. At 480 minutes, or 8 hours, 1M HA treated cells had the largest mean tube length values, showing statistical significance over ECMC and 100K HA conditions (Figure 4-2 B-E). At 720 minutes, or 12 hours, 1M HA treated cells maintained the largest mean tube length values, showing significance over all conditions except 10K (Figure 4-2 F-I). Last, at 960 minutes, or 16 hours, the differences between conditions begin to lessen. 1M still showed the large mean tube length value, but only showed significance compared to ECMC (Figure 4-2 J-M). This data again suggests that the previously established ideas of the MW-dependent bioactivity of HA in endothelial cells and angiogenesis are not universal. For example, Ibrahim and Ramamurthi found contradicting effects of differentially sized HAs in rat aortic ECs, where LMW HA stimulated greater tube formation than HMW HA. Additionally, Wang et al. showed similar effects in HUVECs where LMW HA was able to stimulate tube formation. The dependence of angiogenic activities of ECs with varying, tissue-associated subtypes is not fully understood, necessitating further interrogation of the effects of HA MW in a larger range of EC subtype. The reported data suggests the 1M HA stimulates greater tube formation than LMW HA contrary to past studies in different EC subtypes.

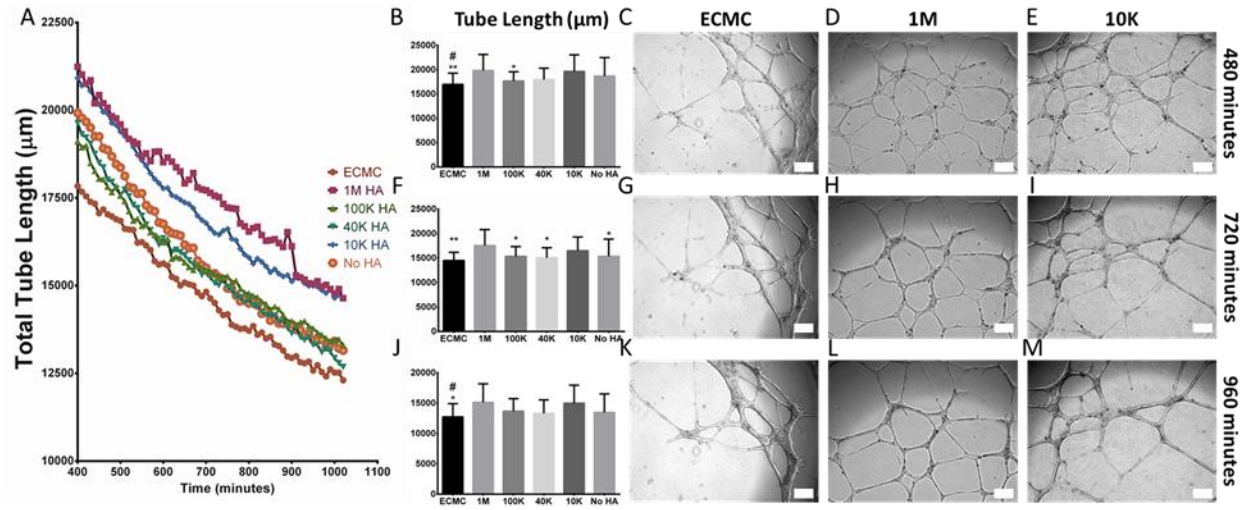

Figure 4-2 HCMVECs cultured on HA
Human cerebral microvascular endothelial cells (HCMVECs) were treated with 1 mg/ml HA with MW ranges of 750-1000 kDa (1M), 100-150 kDa (100K), 41-65 kDa (40K), or 10-20 kDa (10K). As a positive control, HCMVECs were cultured in endothelial cell media complete with an endothelial cell growth supplement (ECMC) or endothelial cell media without the growth supplement or HA (No HA). Tube formation was monitored using time-lapse microscopy, and analyzed for total tube length, the total length of all tubes formed if in a straight line. For all conditions n=21 wells from 3 biological repeats. Two-way ANOVA and Dunnett's multiple comparisons tests were performed to test for statistical significance. The following symbols were used to denote statistical significance: "*" vs 1M and "#" vs 10K. Scale bar is 200 µm.

Data suggests that 1M HA is protective for HCMVECs as they exhibited a significantly increased RVAC but exhibited no significant differences in proliferation when compared to 100K, 40K, and 10K HA. This trend persists when culturing HCMVECs in 3D AMMS (Figure 4-3). The data reported shows no significant differences in EdU+ cells and, thus, there is no increase in HCMVEC proliferation when exposed to lower MW HA chains (Figure 4-3 A). However, when analyzing the RVAC, there is still statistical significance between 1M and 40K HA (Figure 4-3 B). This data suggests that 1M HA maintains a protective role after chemical modification and subsequent cross-linking. One thing to note, the overall values of the ratios are decreased in 3D experiments, when compared to the 2D experiments due to adjustments in signal detection. Since 3D cultures require greater cell number to maintain similar seeding density, the gains for both the

fluorescent and luminescent readings on the BioTek Synergy H1 hybrid multimode plate reader had to be decreased. To account for this, HCMVECs cultured in 2D with ECMC were used a positive control as in the previous chapter.

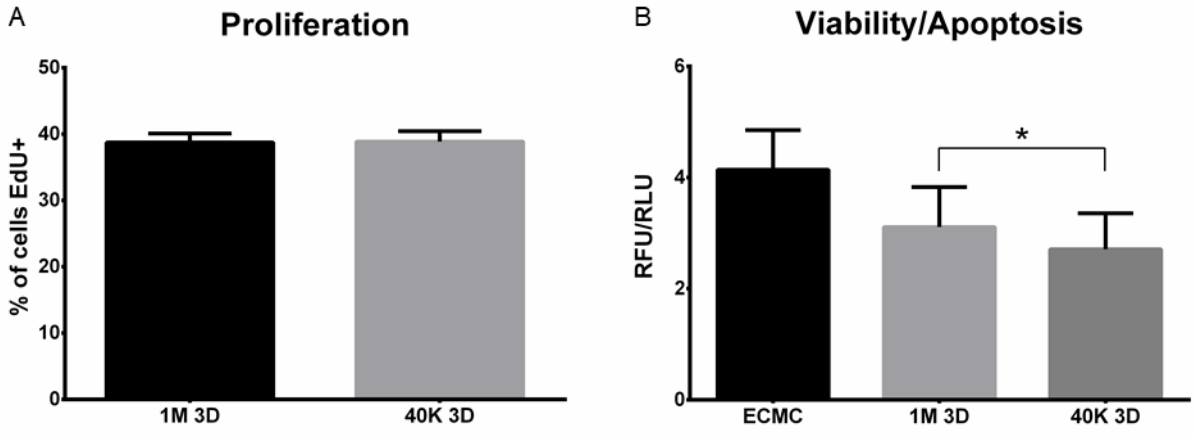

Figure 4-3 Human cerebral microvascular endothelial cells (HCMVECs) were cultured in AMMS made with 1M HA (1M 3D) and AMMS made with 40K HA (40K 3D).
Cell health was characterized by proliferation and the ratio of viable to apoptotic cells. Given the increased cell number required for 3D cultures, the gains had to be reduced for fluorescent and luminescent readings and thus HCMVECs were cultured in 2D with ECMC as a positive control for the ApoLive-Glo™ assay. All graphs are showing mean with standard deviation. Fig 4A has n=9 for all conditions. Fig 4B has n=36 for all conditions. Kruskal-Willis test and Dunn's multiple comparisons test were performed. "*$p<0.05$; significant differences compared to 1M 3D condition.".

Re-vascularization is critical and is often the limiting factor in any biomaterial-based therapeutic. Promoting adequate vascularization after implantation can greatly improve outcomes after SCI[126,130,131], as well as promote wound healing in general[132–134]. This trend persists when culturing HCMVECs in AMMS. After 48 hours, HCMVECs cultured in AMMS made with 1M HA exhibited more mature vessel formation, as inferred by greater branching and interconnectedness of multi-nucleated vessel-like structures in between AMMS particles (Figure 4-4). HCMVECs cultured in AMMS made with 40K HA did not produce branching vessel-like structures, and HCMVECs seem to grow on the surface of particles instead of in between them

like in 1M HA AMMS. This data matches Figure 2 showing that 1M HA promotes greater and more stable tube formation than LMW HA in 3D cultures (Figure 4-4). This result contradicts the conventional thought in the literature that HMW HA is anti-angiogenic, which is based off studies not performed in microvascular ECs[135–137]. This further highlights the need to investigate the MW-dependent bioactivity of HA in a larger range of EC subtypes, as well as a large range of cell types in general.

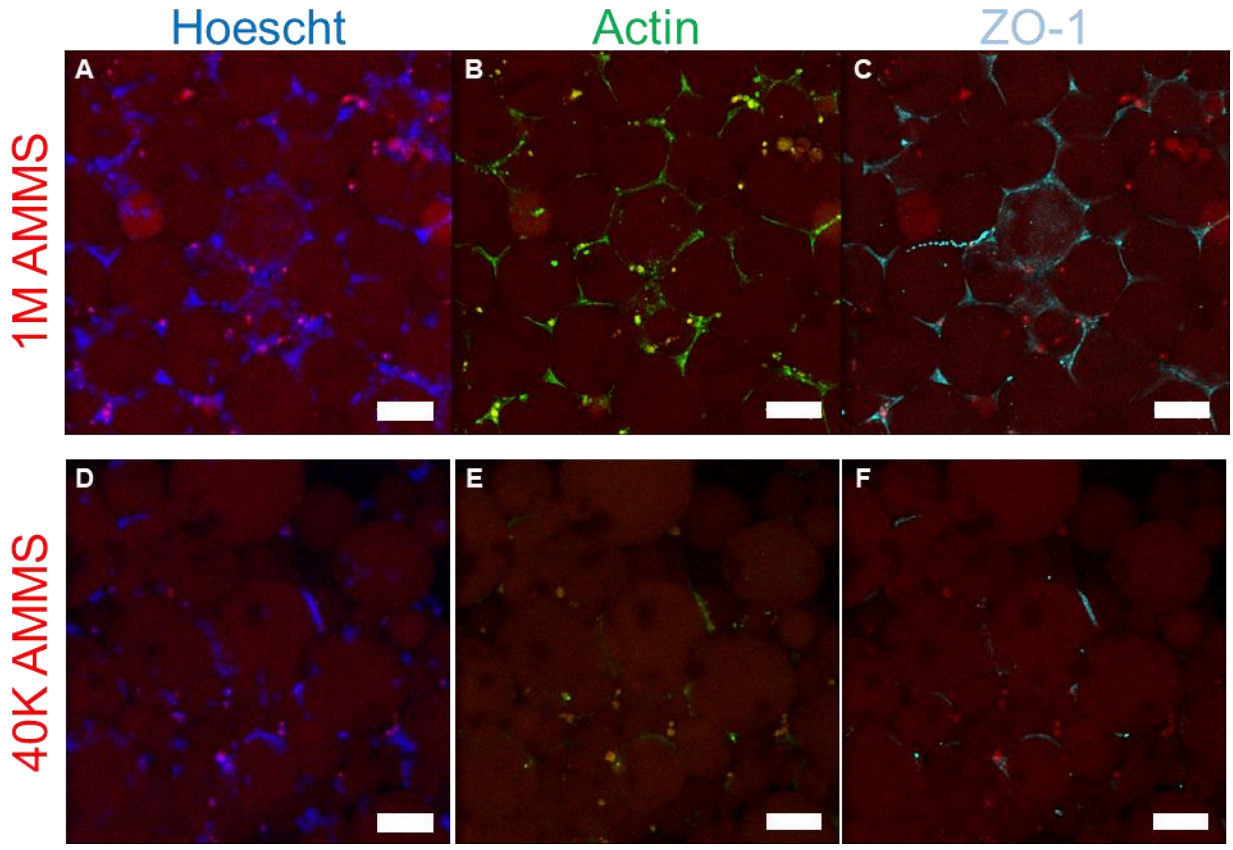

Figure 4-4 Human cerebral microvascular endothelial cells (HCMVECs) were cultured in AMMS made with 1M HA (1M 3D) and 40K HA (40K 3D).
After 48 hours, cultured were fixed, permeabilized, and stained for actin (Fig 5B and 5E) and the tight junction protein, ZO-1 (Fig 5C and 5F). Hoescht was used as counter-stain to label nuclei (Fig 5A and 5D). AMMS can be seen in red in the images. Images are max projections of z-stacks with slices 2 µm apart. Scale bar is 100 µm..

AMMS were injected into the mammary fat pads of mice. After 9 days, the fat pads were explanted, fixed, sectioned, and stained for laminin to visualize blood vessels and CD44. 20x images were tiled and stitched together to visualize the entire fat pad section (**Figure 4-5**). A ROI was drawn around the injection site to exclude the signal from peripheral muscle and fat, and the fluorescent intensity sum was measured in relative fluorescent units (RFU). These intensity sums were then normalized to the area of the ROI. Data is presented in RFU/μm^2. Using at least 2 sections from 3 separate animals, a Mann-Whitney test was used to calculate statistical significance (p<0.001). The data presented shows that mice injected with 1M AMMS had significantly greater levels of CD44 and laminin in the injection site. In the previous figures, 1M HA has been shown to promote vessel formation in both 2D and 3D *in vitro*. This data shows this effect is also seen *in vivo*. This further highlights the need for consideration of HA MW in the design of any HA-based biomaterials for therapeutic application. We hypothesize that the MW-dependent bioactivity of HA involves clustering of its main receptor, CD44. CD44 has been shown to cluster in response to HMW HA, but not LMW HA[138–140]. To test this hypothesis, we used a previously published method of antibody-mediated crosslinking of CD44 to induce clustering[139]. Using the ApoLive-Glo™ Multiplex Assay as in Fig 1 and Fig 3, the RVAC of HCMVECs was measured in both 2D and 3D (Figure 4-6). In 2D solubilized 1 mg/ml HA experiments, the RVAC trend is reversed compared to the non-crosslinked CD44 data (Fig 1). Here, 40K HA treated HCMVECs exhibited a statistically significant increase in RVAC compared to HCMVECs treated with 1M (p<0.01) and 100K (p<0.01). Interestingly, this trend is not conserved in 3D experiments where HCMVECs in AMMS made with 1M exhibited a similar RVAC to HCMVECs in AMMS made with 40K. This data together supports our hypothesis that CD44 clustering is involved in the MW-dependent bioactivity of HA as the MW-dependent RVAC of HCMVECs was essentially

eliminated after crosslinking CD44. While the RVAC of HCMVECs treated with 40K HA was increased compared to other HA MWs in 2D, it does not dispute our hypothesis. However, future studies may benefit from exploring this phenomenon further. To further test our hypothesis, HCMVECs were cultured in AMMS to characterize vessel formation. 3D AMMS experiments were performed as before with the non-crosslinked CD44 HCMVECs. Confocal microscopy was used to capture z-stacks of these cultures. The data shown are maximum intensity projection images. By staining for actin, the morphology of the HCMVECs in culture can be visualized. As with the previously shown RVAC data, both cultures look very similar with HCMVECs forming vessel networks that are interconnected with multiple branches growing through the AMMS. This data, together with the RVAC data, support our hypothesis that CD44 clustering is involved in the MW-dependent bioactivity. Our data shows that CD44 clustering is necessary for the HMW HA response in HCMVECs. Future studies exploring the response after knocking out or silencing CD44 to test whether CD44 clustering alone is sufficient for this response.

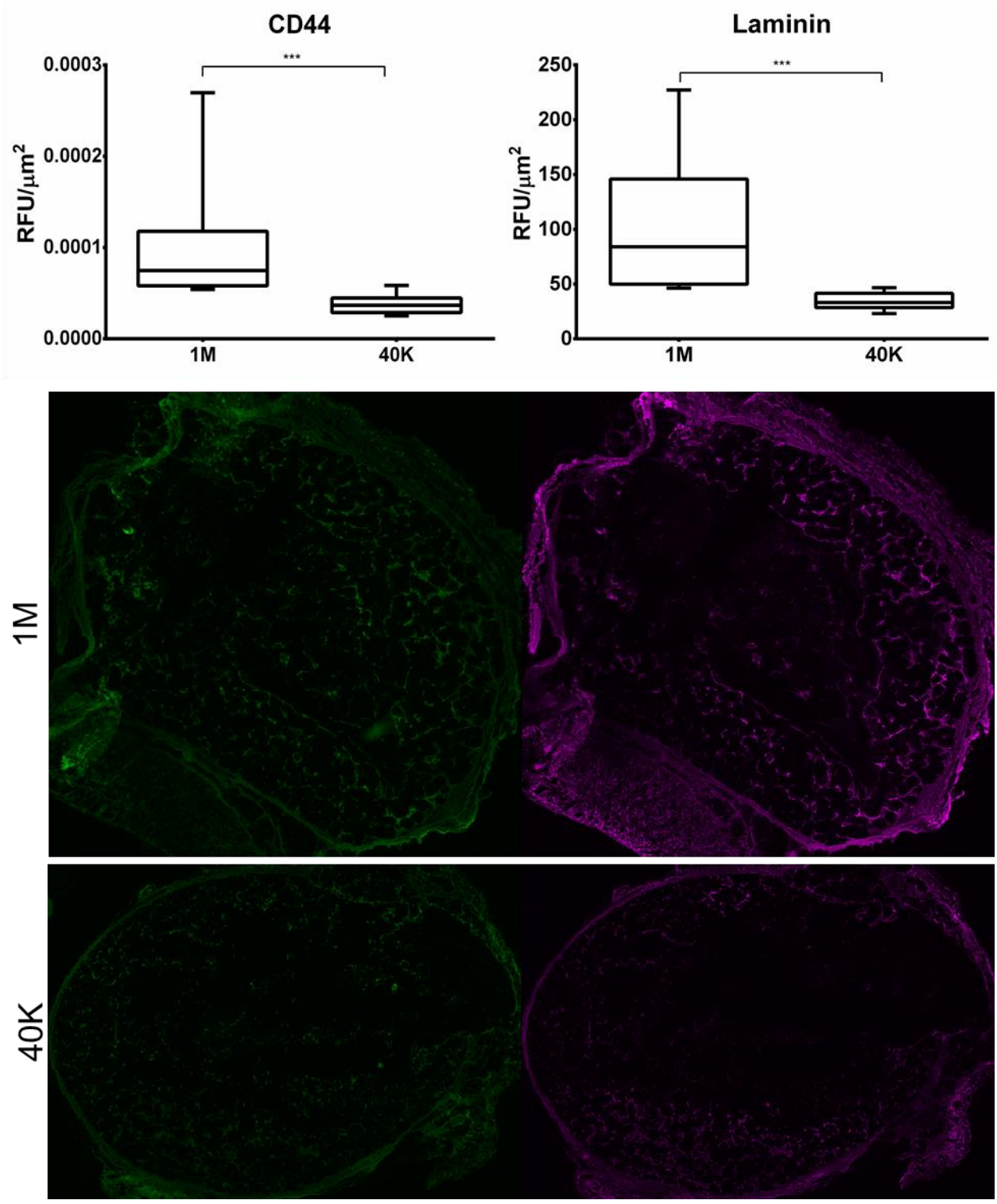

Figure 4-5 AMMS were injected into the mammary fat pad of mice.
After 9 days, fat pad injections were explanted and stained for laminin (blood vessels) and CD44. Images were quantified by measuring the sum of the fluorescent intensity inside the injection site ROI and normalizing to the area of the ROI. Data is reported as the ratio of relative

fluorescent units (RFU) to area of the ROI (µm2). A Mann-Whitney test was used to calculate statistical significance (***p<0.001). At least 2 sections were used from 3 separate animals for quantification. Representative images of CD44 (Fig 6C and 6E) and laminin (Fig 6D and 6F) staining are shown. Scale bar = 1000 µm.

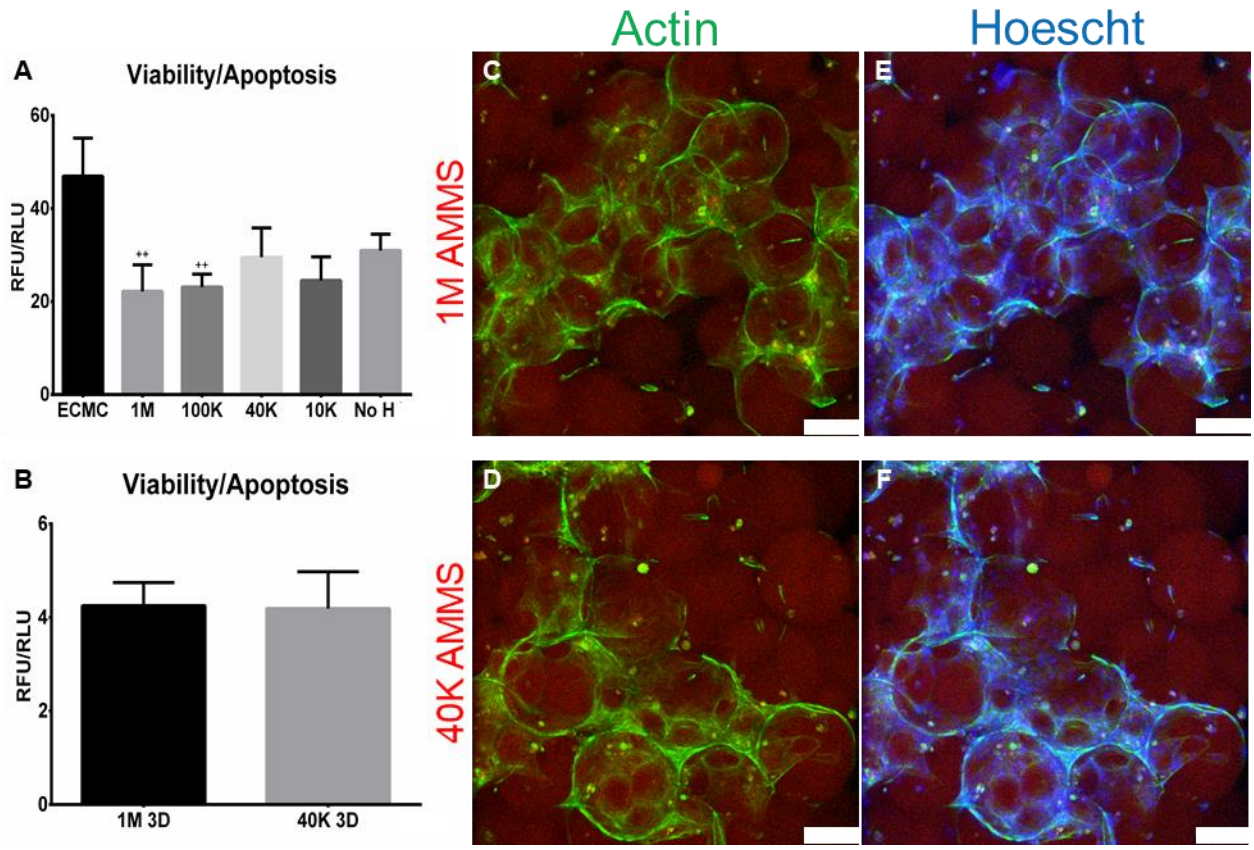

Figure 4-6 Antibody-mediated crosslinking of CD44 was performed on HCMVECs, Cultured in 2D and treated with solubilized 1mg/ml HA or in AMMS made with 1M HA (1M 3D) and AMMS made with 40K HA (40K 3D). The RVAC of 2D and 3D cultures was measured after 24 and 48 hours, respectively. A Kruskal-Wallis and Dunn's multiple comparisons test were used to measure statistical significance (++p<0.01). After 48 hours, cultures were fixed, permeabilized, and stained for actin. Hoescht was used as counter-stain to label nuclei. Images are max projections of z-stacks with slices 2 µm apart. Scale bar is 100 µm

4.3. Conclusion

The goal of this chapter was to evaluate the bioactivity of AMMS, fabricated from HA of varied MW to better understand how the MW-dependent bioactivity of HA is affected after chemical modification and subsequent crosslinking of HA into biomaterials. In the previous

chapter, we showed that HA was able to influence clustering of its main receptor, CD44, in a MW dependent manner. This trend persisted after crosslinking into biomaterials as AMMS made with 1M HA exhibited higher levels of CD44 clustering, measured using FRET, than AMMS made with 100K and 40K. Two-way ANOVA analysis showed no significant difference between the FRET efficiencies in 2D vs 3D cultures. Next, we aimed to determine how HA MW affected the ability of AMMS to promote proliferation, viability, and apoptosis in HCMVECs. The data reported are similar those reported in the previous chapter, as there were no differences in proliferation between conditions, but 1M HA AMMS was able to promote a significantly greater ratio of viable to apoptotic cells than 40K HA AMMS. The data was also consistent between 2D and 3D when analyzing ability of HCMVECs to form tube-like structures in response to HA MW. In AMMS made with 1M HA, HCMVECs were able to produce intricate vessel-like structures that grow through and in between AMMS particles, which is not seen in AMMS made with 40K HA. These data altogether highlight the need for considering HA MW in the design of HA-based biomaterials as HA exhibits a very complex MW-dependent bioactivity that is not universal across cell types.

4.4. Material and Methods

Microfluidics device fabrication

A flow focusing microfluidic device was used for manufacturing hydrogel spheres that were assembled. Microfluidic devices were fabricated using soft lithography. Briefly, master molds were fabricated on mechanical grade silicon wafers (University wafer) using KMPR 1050 photoresist (Microchem). Devices were molded from the masters using poly(dimethyl)siloxane (PDMS) Sylgard 184 kit (Dow Corning). The base and crosslinker were mixed at a 10:1 mass

ratio, poured over the mold, and degassed prior to curing for overnight at 65 °C. Channels were sealed by treating the PDMS mold and a glass microscope slide (VWR) with oxygen plasma at 500 mTorr and 80 W for 30 s. The channels were functionalized by injecting 100 μL of Aquapel (Aquapel) and reacting for 30 s until washed by Novec 7500 (3M). The channels were dried by air suction and kept in the oven at 65 °C until used.

Thiolated hyaluronic acid (HA-SH) synthesis and characterization

Sodium hyaluronate (10-20 kDa (10K, HA10K), 41-65 kDa (40K, HA40K), 100-150 kDa (100K, HA100K), 750-1000 kDa (1M, HA1M), Lifecore Biomedical) was dissolved at 10 mg/mL in distilled, deionized (Di) H2O and thiolated as previously described90,92,133,134. All steps in the thiolation reaction are performed at room temperature. Afterwards, the HA solution was adjusted to a pH of 5.5 using 1M HCl. Then, 1-Ethyl-3-[3-dimethylaminopropyl] carbodiimide (EDC, Sigma- Aldrich, 03450-5G) was dissolved in di H2O at the appropriate molar ratio (varies based on HA MW) immediately before addition to HA solution. N-hydroxysuccinimide (NHS, Sigma-Aldrich, 130672-5G) was then added at the appropriate molar ratio. The pH was then readjusted to 5.5 and the reaction was mixed for 45 min. Then, cystamine dihydrochloride (Thermo Fisher Scientific, AAB2287314) was added at the appropriate molar ratio. pH was adjusted to 6.25 using 1 M NaOH, and the reaction continued while stirring overnight. Dithiothreitol (DTT, Thermo Fisher Scientific, BP172-25) was added in excess at pH 8.5. The mixture was stirred for 2 hours at room temperature to cleave cystamine disulfides and yield HA-SH. The reaction was quenched by adjusting the pH to 4.5. HA-SH was purified using dialysis against acidic (pH 4) di H2O for 3 days in the dark. Purified, HA-SH was vacuum filtered through a 0.22 μm filter (EMD Millipore), frozen under liquid nitrogen, lyophilized, and

stored at – 20 °C until use. HA thiolation was confirmed using the colorimetric Ellman's test for free thiols.

Hydrogel microparticle formation

HA-SH was crosslinked with 20 kDa vinyl sulfone-terminated 4-arm polyethylene glycol (PEG-VS, JenKem Technology, A7025-1) modified with 300 μM thiolated RGD (RGD-SH, GenScript) and 10 μM thiolated fluorophore, Flamma 552 (AdipoGen, BCT-CWT1058-M001). These pre-gel solutions were sterile-filtered through a 0.2 μm polyethersulfone (PES) membrane in a luer lock syringe filter, injected into the microfluidic device and pinched off by oil phase (0.1% Pico-Surf in Novec 7500, SF-000149, Sphere Fluidics). The flow rate for aqueous solutions was 10 μL/min and for oil solutions was 50 μL/min. Gels were collected from the device into a tube in oil phase, incubated overnight at room temperature in the dark. Microgels in the oil phase were vortexed with 20% 1H,1H,2H,2H-Perfluoro-1-octanol (PFO) (Sigma-Aldrich) in Novec 7500 for 10 s. Micro-gels were then mixed with 1:1 mixture of HEPES buffer (100 × 10 mM HEPES, 40 × 10 mM NaCl pH 7.4) and hexane followed by centrifugation at 10000 rpm to separate microgels from oil for five times. Microgels were incubated in sterile filtered 70% ethanol solution at 4 °C at least overnight for sterilization. Before experiments, microgels were washed with HEPES buffer five times. For in vitro studies, microparticles were concentrated by centrifugation, and incubated in the designated culture dish overnight at 37 °C to allow the microparticles to anneal forming an annealed macroporous microparticle scaffold (AMMS).

Mechanical Characterization

Bulk gel solutions made of the same solutions used for microparticle fabrication were

swollen to equilibrium overnight in PBS before mechanical characterization. Rheological characterization was done using an AR2000 rheometer (TA Instruments) with crosshatched plate and 8 mm geometry to prevent slipping and a solvent trap to minimize evaporation. The testing stage was maintained at 37°C. Oscillatory stress sweeps at 1 Hz and 1% strain and frequency sweeps at 1% strain were performed on scaffolds swollen in PBS, pH 7.4

Cell Culture

SV40-immortalized human cerebral microvascular endothelial cells (HCMVEC, Applied Biological Materials (ABM), T0259) were used for all endothelial cell experiments. HCMVECs were cultured in ScienCell's complete Endothelial Cell Media (ECMC, 1001). All experiments were conducted using HCMVECs on passage 6 or 7. HCMVECs were cultured on PriCoat flasks (ABM, G299) or Applied Cell Extracellular Matrix (ACECM, ABM, G422) coated plates per manufacturers' instructions. The human embryonic kidney (HEK) cell line, Lenti-X™ 293T (Takara Bio, 632180) was used as a model cell line for CD44 clustering experiments. HEK cells were cultured in Dulbecco's Modified Eagle's Medium (DMEM, Corning, 10013CV) supplemented with 10% fetal bovine serum (FBS, GenClone, 25-550) and 1% antibiotic-antimycotic (ABAM, Gibco, 15240062) for expansion and for Western blot experiments. For fluorescent resonance energy transfer (FRET) experiments, the cell culture media was changed to Live Cell Imaging Solution (LCIS, Invitrogen, A14291DJ) supplemented with 10% FBS, 1% ABAM, and 2 drops/ml NucRed™ Live 647 ReadyProbes™ Reagent (Invitrogen, R37106) for nuclei counter staining. For 3D FRET experiments, HEKs were seeded on an AMMS and allowed to attach overnight before analysis.

EdU test for proliferation

HCMVECs were seeded in the appropriate media condition and allowed to proliferate for 24 hours before being pulsed with 2'-Deoxy-5-ethynyluridine (EdU, Abcam, ab146186) for 2 hours. Cells were then passaged and fixed using 4% paraformaldehyde for 15 minutes. After fixation, cells are permeabilized using 0.1% saponin and 1% BSA in PBS. EdU staining was performed using the Click-iT™ Plus Alexa Fluor™ 488 Picolyl Azide Toolkit (Thermo, C10641) per manufacturer's instructions. Flow cytometric analysis was performed using a Millipore Guava EasyCyte 5 HPL Benchtop Flow Cytometer and GuavaSoft.

Viability and apoptosis

HCMVECs were seeded in the appropriate media condition and cultured for 24 hours in a 96-well plate before viability and apoptosis were measured using the ApoLive-Glo™ Multiplex Assay (Promega, G6411). Viability is measured in this assay using glycyl-phenylalanyl-amino fluorocoumarin (GF-AFC), a cell permeant, peptide substrate that generates a fluorescent reading when cleaved by live-cell protease activity. Apoptosis is measured using a caspase 3/7 luminogenic substrate. Fluorescent and luminescent signals were measured using a BioTek Synergy H1 hybrid multimode plate reader.

Vector Design

All lentiviral vectors were developed using VectorBuilder's Vector Design tool and purchased from VectorBuilder. To perform all FRET studies, three vectors were developed: CD44-mTFP1 (VB210402-1113mts), CD44-Ypet (VB171201-1092vjt), and PMT-mTFP1-Ypet (VB210402-

1112gew). To perform all western blot studies, a CD44 overexpression vector (VB191002-1258ayx) was developed.

Lentivirus Production

Briefly, 80% confluent HEK cells were transfected with third generation packaging plasmids (pRSV-Rev and pMDLg/pRRE were gifts from Didier Trono (Addgene plasmids # 12253 and # 12251, respectively)), a plasmid encoding the lentiviral capsule (pCMV-VSV-G was a gift from Bob Weinberg, Addgene plasmid # 8454), and either a CD44-mTFP1, CD44-Ypet, PMTmTFP1-Ypet, or CD44 overexpression vector using jetPRIME transfection reagent (Polyplus 49 transfection). Lentiviral particles were recovered from media after 2 days of culture using PEGit ™ virus precipitation solution (SBI System Biosciences), resuspended in 1x PBS and stored at –80 °C.

Acceptor-photobleaching-based FRET

Measurement Confocal microscopy imaging and photobleaching experiments were performed at 37 °C using a Leica SP5 laser scanning confocal microscopy system and a 63x water immersion objective, HC APO L 63x/0,90 W U-V-I (Leica, 506148). If there are any interactions between mTFP1 (donor) and Ypet (acceptor) leading to energy transfer in the cells, photobleaching Ypet would lead to an increase in mTFP1 intensity since mTFP1 would no longer be quenched by the Ypet. In the photobleaching experiments, a high intensity laser (100% laser power at 514 nm beam) was applied to the region of interest for 500 frames to locally bleach the Ypet present. Data acquisition was gathered immediately after bleaching. The sample area was scanned at the resolution of 1024 × 1024 pixels. The mTFP1 and Ypet were excited at 458 and 514 nm,

respectively. Two frames of pre-bleach and post-bleach mTFP1 and Ypet fluorescence intensities were recorded. The FRET efficiency € was calculated using the following equation: $E = 1 – (Fpre/Fpost)·Fpre$ The variables Fpre and Fpost indicate the fluorescent intensity of mTFP1 before and after acceptor photobleaching, respectively. All FRET Efficiency measurements were made using the FRET AB Wizard in the Leica LAS AF software. Two-way ANOVA and Sidak's multiple comparisons test were used to determine statistical significance.

Chapter 5. Future Perspectives of Immunomodulatory MAP Gel for Complete Wound Healing Application

The healing of human skin wounds is designed for a rapid fibroproliferative response at the expense of tissue complexity and is therefore prone to scar formation. Moreover, wound healing often goes awry when excessive inflammation leads to chronic non-healing wounds or when excessive repair results in uncontrolled tissue fibrosis. The immune system plays a central role in orchestrating wound healing, and thus, controlling immune cell activities holds great potential for reducing scars and enhancing regeneration. Biomaterial dressings directly interact with immune cells in the wound and have been shown to improve the repair process. A few studies have even shown that biomaterials can induce complete regeneration through mechanisms involving immune cells. Here, we review the role of the immune system in skin repair and regeneration and describe how advances in biomaterial research may uncover immunomodulatory elements to enhance fully functional skin regeneration.

5.1. Perspective of immunomodulatory biomaterial for wound healing

Impaired wound healing in response to traumatic injury or surgery remains a challenge to healthcare systems around the globe. Wound healing is initiated by blood coagulation and local inflammation, which is followed by the resolution of inflammation and tissue repair. The healing process often goes awry upon excessive inflammatory activation leading to chronic non-healing wounds[141], or excessive reparative activation resulting in uncontrolled tissue fibrosis[142]. A successful response to injury eliminates the threat of infection locally, heals the affected tissue, and restores its structure and function. While human skin heals predominantly with a dense collagen rich scar that lacks functional hair follicles and fat glands, some species can completely

regenerate, whereby tissue fully re-establishes its original anatomy. Engineered biomaterials for wound treatment provide a toolbox of pro-healing features including mechanical support, protection from pathogens, hydration, and act as a scaffold for cellular recruitment or vehicle for cell and drug delivery. Importantly, biomaterials interact with host immune cells, modulating their biochemical and physical environment and downstream activation responses[143]. Moreover, a few studies have shown that biomaterials can stimulate complete regeneration through mechanisms involving immune modulation[11,144], suggesting that biomaterial-induced immunomodulation may be a key feature for inducing regenerative events.

Here, we will first review the role of the immune system in skin repair and regeneration, and then describe natural and synthetic biomaterials used clinically or under development as wound dressings, and their immunomodulatory properties. We will then highlight studies that have remarkably shown biomaterial-induced regeneration. Finally, we will describe approaches that utilize biomaterials to deliver cells or drugs that tune the immune response. A better understanding of biomaterial-induced immunomodulation will ultimately lead to the design of innovative biomaterials-based strategies that enhance healing, prevent scarring, and promote tissue regeneration.

5.1.1. The immune system in skin repair and regeneration

Wound healing in the skin is initiated by the release of soluble mediators from resident cells in the injured tissue, which promotes the exudation of damage signals and leads to an influx of leukocytes from the blood. The so-called damage-associated molecular patterns (DAMPs) – endogenous “danger” molecules that include various intracellular proteins, nucleic acids, and

degradation metabolites are major inflammatory mediators released by damaged host cells. DAMPs bind to pattern recognition receptors (PRRs) on inflammatory cells, such as Toll-like receptors (TLRs), and initiate immune responses[145]. Injury activates resident mast cells to release inflammatory cytokines such as tumor necrosis factor alpha (TNF-α) and interleukin-6 (IL-6) along with vascular permeability factors such as histamine that promote leukocyte recruitment[146]. The first leukocytes recruited to the wound, mostly neutrophils, function to phagocytose and eliminate damaged cells and foreign microorganisms introduced by the outside environment. Sites of neutrophil activity generate a cytotoxic environment through oxidative burst and release of proteases and neutrophil extracellular traps. A by-product of this exuberant killing is neutrophils undergoing programmed cell death, or apoptosis[147]. This occurs alongside monocyte influx and their maturation into inflammatory macrophages.

Macrophages are essential to wound healing and participating in both early inflammatory and later healing stages. Depletion of macrophages using clodronate liposomes or transgenic approaches causes delayed re-epithelialization, angiogenesis, and wound closure[148,149]. Inflammatory macrophages secrete a milieu of cytokines and chemokines including TNF-α, IL-6, IL-12, and CC-motif chemokine ligands such as CCL-2 (MCP-1) to facilitate inflammation and promote additional monocyte infiltration. Macrophages also engulf apoptotic neutrophils in a non-inflammatory process termed efferocytosis[150]. This clearance is a critical checkpoint to successful wound healing and triggers an anti-inflammatory and pro-resolution transition, which blocks excessive neutrophil recruitment and eliminates early inflammatory components[151]. Defects in this stage often give rise to non-healing wounds. During the resolution of inflammation, macrophages undergo a phenotype conversion to anti-inflammatory macrophages,

which are characterized by the production of anti-inflammatory cytokines such as IL-10 and interferon-beta (IFN-β)[152]. Macrophage anti-inflammatory activation is closely tied to pro-repair activation that is characterized by the production of reparative growth factors such as transforming growth factor-beta (TGF-β), vascular endothelial growth factor (VEGF), and platelet derived growth factor (PDGF)[153]. However, if not controlled in a timely fashion, these macrophages can also promote tissue fibrosis, either by persistent production of reparative growth factors that promote myofibroblast activation such as TGF-β or directly by excessive extracellular matrix (ECM) deposition[154]. A dysregulated and prolonged healing phase can result in the deleterious outcome of skin fibrosis[155,156]. Importantly, anti-inflammatory signals such as IL-10 and IFN-β in the skin were shown to also limit ECM deposition[157]. Hence, resolution of inflammation is an essential prerequisite for proper wound healing by limiting both inflammation and tissue repair short of exuberant fibrotic scarring.

Adaptive immunity also plays a vital part in inflammation and tissue remodeling after injury. T cells are chemo-attracted to wounds by DAMPs and cytokines which stimulate pro-inflammatory activities by type 1 T helper (Th1) cells. Th1 cells facilitate inflammation through signals such as IFN-γ, TNF-α, and IL-12. These signals are counterbalanced by type 2 T helper (Th2) cells that produce IL-4 and IL-13. In addition to suppressing the Th1 pro-inflammatory effect, Th2 cells facilitate repair and ECM production. Importantly, the Th2 activity is also known to be involved in dysregulated repair and fibrosis[158]. Hence, in parallel to macrophages, T cell activity must be tightly regulated for proper wound healing. Interestingly, transfer of T cells into mice that lack T cells resulted in less inflammation and scarring compared to control mice, suggesting an important role for the adaptive immune system in wound resolution. Upon injury,

regulatory T cells (Tregs) resident in the skin are reinforced by recruited Tregs, which can lead to a 30–60% increase in cell number. Tregs suppress inflammation and promote tissue repair by production of ARG1, IL-10, and TGF-β[159] and Treg-depletion in mice exhibits enhanced wound inflammation and impaired healing. Another important lymphocyte subset is the skin resident γδT cells. Their regulation of skin wound healing involves production of growth factors such as several fibroblast growths factors, and insulin-like growth factor-1[160], which promote myofibroblast activation, and proliferation of keratinocyte and hair follicle stem. Thus, γδT cells are drivers of repair and regeneration of skin appendages. Overall, proper innate and adaptive immune function is required for optimal repair Immune cells not only play roles in early stages of wound repair but also regulate later events of regeneration. Regeneration of skin restores the tissue anatomy and function, with the development of hair follicles and fat glands serving as hallmarks. Such 'complete regeneration' is often not achieved, and instead the "default" hairless and fatless scar results. Though small (~6 mm) full-thickness skin wounds typically heal with scar formation in adult mice, large wounds (1 cm 2 in 3-week-old mice or 2.25 cm2 in 7 week-old or older mice) heal with tissue regeneration, called wound-induced hair neogenesis (WIHN). This profound regenerative phenomenon involves sophisticated cellular and molecular mechanisms, among which modulation of the signaling environment by diverse immune cells plays an essential role.

Among the diverse immune cell types present in the wound, macrophages and γδT cells have been linked to the mechanism of hair neogenesis. Infiltration of nascent scar tissue in the WIHN model by CD11b+/CD206+ macrophages increases between 2 to 3 weeks post-wounding in the vicinity of newly forming hair follicles[161] and depletion of macrophages both with the

genetic strategy[161] or with clodronate liposomes in wounded mice attenuates efficiency of hair neogenesis. Macrophages can modulate hair neogenesis by signaling to other wound cell types via one or several cytokines or growth factors, including TNF-α. Interestingly, both genetic depletion, as well as transgenic overexpression of TNF-α in mice, decreases their ability to regenerate new hairs in large skin wounds, suggesting that the TNF-α effect in wound healing is likely fine-tuned and context-dependent[162]. In addition to direct secretion, macrophages can modulate the signaling milieu of wounds via molecule uptake. Specifically, in late-stage large wounds, macrophages phagocytose alternatively spliced domain A (EDA) of fibronectin and along with it WNT inhibitor SFRP4, which binds to EDA. Higher levels of phagocytic activity by macrophages result in a significant reduction in SFRP4 and de-inhibition of WNT signaling, which, when persistent, has a pro-fibrotic effect. Consistently, injection of wounds with hemin, which inhibits phagocytosis, directed wound healing response away from fibrosis, and promoted hair neogenesis[163]. In addition to macrophages, regenerative response in large wounds requires signaling by γδT cells, which serve as the early cellular source for FGF9 at the onset of hair neogenesis. Mice with a genetic defect in γδT cell formation or with T cell-specific Fgf9 deletion have reduced hair neogenesis levels, while mice over-expressing Fgf9 in wound epidermis have enhanced WIHN response.

Commensal and pathogenic bacteria from the skin surface and associated inflammatory stimuli tune the composition, activation status, and signaling outputs of immune cells, which in turn fight off the microbial invasion and direct repair of skin wounds. Intriguingly, in addition to triggering tissue inflammation, bacteria have been recently shown to function as regulators of regeneration[164]. In the WIHN model, the efficiency of new hair follicle regeneration correlates

with the status of the skin microbiome, being the lowest in germ-free mice, intermediate in mice housed under specific pathogen-free conditions, and the highest in wild-type mice with the intact microbiome. Surprisingly, WIHN efficiency also enhances in response to skin infection with pathogenic Staphylococcus aureus. Mechanistically, inflammatory cytokine IL-1β and keratinocyte-dependent IL-1R-MyD88 signaling were shown to be essential for this bacteria-stimulated hair neogenesis in large skin wounds[165]. Notably, this inflammatory reaction also links tissue damage sensing in response to wounding to the earliest molecular events in hair neogenesis. Double-stranded RNA (dsRNA) species, which are released in wounded skin, activate TLR3 and its downstream effectors IL-6 and STAT3 to promote more efficient hair neogenesis. In addition, dsRNA-TLR3 signaling induces intrinsic retinoic acid synthesis, which also promotes hair neogenesis. Prostaglandins are another group of endogenously produced inflammatory molecules with an essential role in wound healing. Levels of prostaglandin PGD2 and its synthase PTGDS inversely correlate with hair regeneration efficiency in the WIHN model. Topical application of PGD2 to wounds decreases hair neogenesis and mice mutant for PGD2 receptor Gpr44 show increased hair neogenesis.

Compared to Mus musculus, rodents in the genus of Acomys (spiny mice) show naturally enhanced efficiency of hair neogenesis after full-thickness skin wounding[166]. Though the mechanism of elevated regenerative ability in spiny mice remains only partially understood, immune cells appear to play an essential role. Brant et al. showed that enhanced regenerative healing in spiny mice might be related to the blunted inflammatory response in skin wounds in comparison to Mus musculus. Acomys wounds were found to have few if any F4/80+ macrophages and reduced levels of many pro-inflammatory cytokines[167]. Interestingly, in

another study, Simkin et al. demonstrated that macrophages are, in fact, necessary for the regenerative response in spiny mice, albeit in ear punch holes rather than excisional dorsal skin wound model[168]. Depletion of macrophages in Acomys with clodronate liposomes significantly delayed the closure of ear hole wounds. While the role of macrophages in enhanced regenerative healing in spiny mice requires further investigation, partially reconciling the above findings is the fact that in ear hole wounds pro-inflammatory macrophages do not invade the regenerating tissue and, instead, remain restricted to the edge of the original wound.

5.1.2. Biomaterials for repair and regeneration of skin

Biomaterials used as dressings to treat wounds include natural biopolymers derived from mammalian or non-mammalian sources, as well as synthetic materials. Materials derived from natural ECMs have the principal advantages of biocompatibility and structural and biochemical similarities to the host wound environment. These materials are prepared from decellularizing tissues or synthesized from natural ECM components such as fibrin, collagen, and hyaluronic acid. Other common natural components found in wound dressings are polymers of non-mammalian origins such as alginate, chitosan, and dextran. While natural biomaterials have been applied extensively to heal wounds, they also display inherent shortcomings, including high cost of manufacture and limited flexibility to adjust their biophysical and biochemical properties according to clinical demands. Many of these properties are essential for the successful integration of immunomodulatory biomaterials as a regenerative wound dressing[169]. Synthetic biomaterials offer enhanced flexibility for the engineering of biophysical and biochemical properties to precisely modulate host responses at the injury site. In addition, synthetic materials can be produced quickly, cost efficiently, and may also be used in combination with natural

materials. While there are already numerous biomaterial-based scaffolds used clinically, the effects of these materials on the immune cell mediators of healing and regeneration are still under investigation and will be discussed here. Tables 5 1-4 summarize the highlights of results described in the following sections.

Table 1. Effects of natural biomaterials on immunomodulation and healing of skin wounds

Biomaterial	Method	Immunomodulation	Healing	References
Acellular dermal substitute—OASIS	Human post-traumatic acute wound	Improved acute inflammation histological scores	Accelerated healing at day 33	Yeh et al. 2017
Acellular equine pericardial collagen matrix (sPCM)	Mouse full-thickness excisional wound	Reduced proinflammatory (IL-1 and TNF-α) and increased anti-inflammatory (IL-10 and VEGF) markers	Enhanced wound closure with complete epithelialization at day 14	El Masry et al. 2019
Fibrin hydrogel	Mouse full-thickness excisional wound	Reduced macrophage inflammatory markers (inducible nitric oxide synthase [iNOS]) and mechano-responsive activation (YAP)	Reduced scar size at day 30	Meli et al. 2020
Hyaluronic acid hydrogel	Diabetic mouse (streptozocin model) full-thickness excisional wound	Reduced inflammatory factors (TNF-α and IL-1) and up-regulate anti-inflammatory/pro-healing factors (IL-10 and TGF-β)	Accelerated diabetic wound healing at day 14	Yang et al. 2021
Human split-thickness skin xenograft	Mouse full-thickness excisional splinted wound	Increased infiltration of circulating immune cells including macrophage with pro-repair markers (CD206, CD163, etc.)	Improved collagen deposition (physiologic architecture) and increased angiogenesis at days 14 and 28	Henn et al. 2021

Table 5-1 Effects of natural biomaterials on immunomodulation and healing of skin wounds

Table 2. Effects of synthetic biomaterials on immunomodulation and healing of skin wounds

Biomaterial	Method	Immunomodulation	Healing	References
Synthetic PEG microspheres with RGD, KQ peptide	Mouse full-thickness excisional wounds	Microporous scaffolds elicit a significantly lower response of $CDllb^{+}$ cells as compared to nonporous controls	Accelerated wound closure mediated by the microporous scaffold	Griffin et al. 2015
Self-healing chitosan-g-polyaniline with PEGS-FA	Mouse full-thickness skin defect model	Induced higher expression of wound healing markers including EGF, TGF-β, and VEGF	Treated wound with Chitosan with PEGS-FA showed better healing compared to commercial products at day 15	Zhao et al. 2017
PEG-RPC hydrogels	Small cuts and full-thickness wounds in a skin defect model	PEG-RPC gel suppressed infiltration of inflammatory cells and accelerated angiogenesis	Accelerated wound healing compared to control conditions at day 14	Chen et al. 2013
Synthetic PEG microspheres with heparin micro islands	Diabetic mouse (db/db model) full-thickness excisional splinted wound	Polarizing macrophages to a pro-regenerative M2 over proinflammatory Ml phenotype	Improve epidermal regeneration and revascularization in a diabetic wound model	Pruett et al. 2021

Table 5-2 Effects of synthetic biomaterials on immunomodulation and healing of skin wounds

Table 3. Effects of immunomodulating biomaterials on regenerative healing of skin wounds

Biomaterial	Method	Immunomodulation	Healing	References
Dextran-allyl isocyanateethylamine and polyethylene glycol diacrylate	Mouse burned skin excision	Macrophages ($F4/80^+$) and neutrophils (MPO^+) infiltration	Skin appendages including mature epithelial structure with hair follicles and sebaceous glands at day 21	Sun et al. 2011
Granular microporous annealed particles (MAPs) of polyethylene glycol-vinyl sulfone	Mouse full-thickness excisional splinted wounds	myeloid cell recruitment ($CDllb^+$, $F4/80^+$) and IL-33	Treated wounds form numerous epidermal cysts and, prominently, regenerate de nova hair follicles at day 21	Griffin et al. 2021

Table 5-3 Effects of immunomodulating biomaterials on regenerative healing of skin wounds

Table 4. Effects of biomaterial delivery systems on immunomodulation and healing of skin wounds

Biomaterial	Method	Immunomodulation	Healing	References
Gelatin hydrogel supplemented with biosurfactant Surfactin A	Diabetic rat (streptozocin model) full-thickness excisional wound	Macrophage markers: reduced ratio of inflammation to repair markers (inducible nitric oxide synthase [iNOS]/ CD206)	Accelerated diabetic wound healing and increased angiogenic markers at day 11	Yan et al. 2021
Pullalan-collagen hydrogel with vitamin-D treated macrophages	Mouse full-thickness excisional splinted wound	Increased myeloid proliferation and enhanced expression of macrophage repair genes (*Mertk*, *Vegfa*, etc.)	Accelerated wound healing and increased angiogenesis at day 10	Henn et al. 2021
Hyaluronic acid hydrogel supplemented with Paeoniflorin	Diabetic mouse (streptozocin model) full-thickness excisional wound	Macrophage markers: reduced inflammation (iNOS) and increased repair (Arg-1)	Accelerated diabetic wound healing at day 14	Yang et al. 2021

Table 5-4 Effects of biomaterial delivery systems on immunomodulation and healing of skin wounds

While the precise mechanisms of biomaterial-induced regeneration are still being unraveled, modulation of the immune system has been implicated in all instances. Likely, dynamic activation and inhibition of both innate and adaptive immune cells are needed to elicit complete regeneration. Thus, leveraging the immunomodulatory effects of biomaterials remains an important strategy for developing novel wound dressings to encourage regeneration and reduce scarring. Natural biomaterials contain ligands that bind and regulate immune cells (Figure 5-1), whereas synthetic materials can be used to further tune the composition, structure, and mechanical properties (Figure 5-2) – all important factors in regulating immune cell activities. In addition, biomaterials may be used to controllably deliver immunomodulatory cells and drugs. This section will review biomaterial systems that have been shown to contribute positively to healing, and their known immunomodulatory effects and mechanisms.

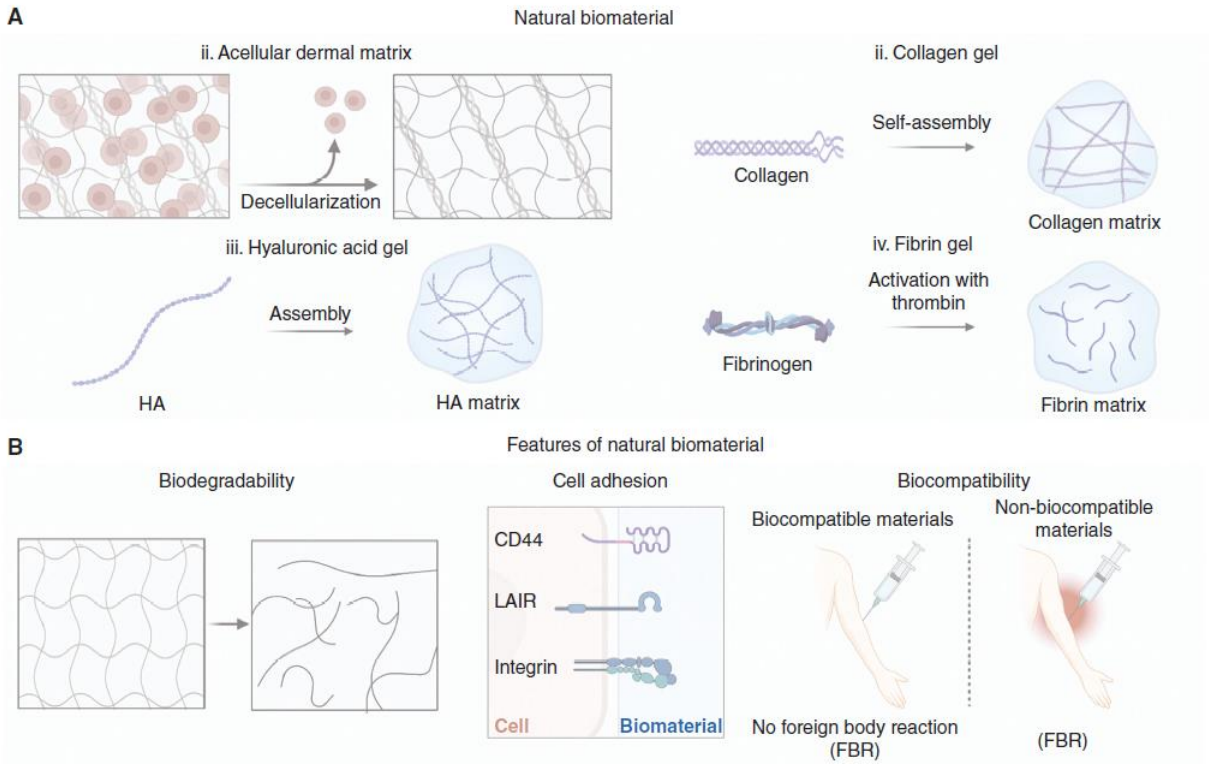

Figure 5-1 Effects of biomaterial delivery systems on immunomodulation and healing of skin wounds

Natural extracellular matrix (ECM)-based materials. (A) Schematic representations of natural biomaterial fabrication processes including (i) acellular dermal substitute production by removal of cells, (ii) collagen scaffold production by self-assembly, (iii) hyaluronic acid (HA) scaffold production, and (iv) fibrin matrix production from fibrinogen and thrombin. (B) Features of natural biomaterials beneficial for wound healing include its degradability, molecular interactions with cells, and biocompatibility.

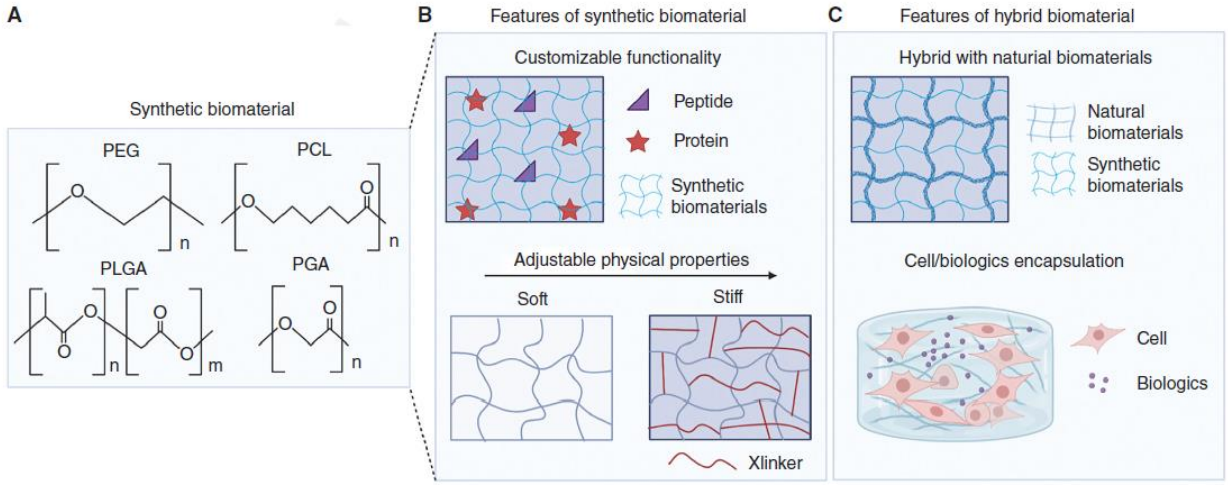

Figure 5-2 Effects of biomaterial delivery systems on immunomodulation and healing of skin wounds
Synthetic and hybrid biomaterials. (A) Chemistry of common synthetic biomaterial scaffolds including PEG (poly (ethylene glycol)), PLGA (poly (lactic-co-glycolic acid)), PCL (polycaprolactone), and PGA (polyglycolic acid). (B) Features of synthetic biomaterials beneficial for wound healing include the ability to conjugate peptides or proteins and control of physical properties. (C) Synthetic materials can be combined with natural biomaterials to create hybrid materials and used to deliver immunomodulatory cells or biological agents.

Collagen: Collagen is the most abundant scaffold protein in the dermal ECM and has therefore been widely explored as a biomaterial for skin wound healing, where it often serves as a dermal analog[170]. It is highly conserved evolutionarily and hence allogeneic and xenogeneic sources provide physical and biochemical properties analogous to host collagen. Recombinant collagen production systems are currently under development and could potentially provide safer and more consistent manufacturing[171]. Collagen has many desirable features such as biocompatibility and tunable fibrillar structure, and also acts as a scaffold that binds platelets and cells[172]. Additionally, collagen is degradable by native collagenases and provides a competitive substrate, which can reduce the degradation of host tissue. Gelatin, a denatured form of collagen, shares biocompatibility of collagen, mainly adhesiveness and degradability, but lacks the ability to form fibrils. Therefore, gelatin is a soluble material that can be modified to form a covalently

crosslinked scaffold[173]. The type of crosslinking can affect immune reaction. For example, crosslinking of gelatin with 1-ethyl-3-(3-dimethyl aminopropyl)-carbodiimide and N-hydroxysuccinimide (EDC/NHS) results in a porous structure and reduces macrophage expression of TNF-α and CCL-22 when compared to formaldehyde and glutaraldehyde crosslinking[174].

Collagen-based matrices have been shown to modulate immune cell activity through specific molecular interactions. A recent study using a murine full-thickness excisional wound model demonstrated that equine pericardial collagen matrix increased initial macrophage recruitment at day 3 and their efferocytic activity that removes apoptotic cell debris in the wound [175]. This effect promoted a pro-healing environment and led to decreased macrophage numbers at a later point - day 7 - along with a decrease in overall inflammatory cytokines, increase of the pro-healing factors IL-10 and VEGF and enhanced re-epithelialization. Immune cells express several receptors that bind directly to collagen, including integrins, discoidin domain receptors (DDR1 and DDR22), and leukocyte-associated immunoglobulin-like receptor-1 (LAIR-1)[176]. LAIR binding inhibits leukocyte activities such as T-cell activation and basophil degranulation and macrophage inflammatory activation[177]. In addition, integrin interactions are also thought to be involved in the inhibition of inflammation by macrophages cultured on gelatin. In sum, collagen appears to reduce inflammation and promote immune regenerative activities through specific interactions between cell surface receptors and ligands presented by collagen, but this response is highly dependent on processing methods that influence its structure and presentation of ligands.

Fibrin is produced during the coagulation cascade and is the major matrix component of blood clots. Hence, it is an essential component in wound healing, providing hemostasis and a provisional matrix for cell adhesion[178]. Fibrinogen is used as a precursor to polymerize into fibrin, forming an autologous scaffold with excellent biocompatibility. Fibrin-based hemostats, sealants, and adhesives are widely used in FDA-approved commercial products as surgical "glue" and for wound healing applications[179]. Fibrin has been shown to reduce bacterial infections and stimulate cell proliferation and angiogenesis while modulating inflammation in acute and chronic wound healing[180].

Macrophages cultured on fibrin hydrogels exhibit a reduced inflammatory response to LPS when compared to cells cultured on polystyrene[181]. However, when the hydrogel was crosslinked, increasing its stiffness and potentially reducing degradability, inflammatory responses were heightened. Mechanistically, stiffness has been shown to enhance YAP-mediated mechanotransduction and macrophage inflammatory responses[96]. Furthermore, fibrin hydrogels applied to a 5 mm murine wound reduced inflammatory marker inducible nitric oxide synthase (iNOS) and enhanced wound healing marker Arginase in macrophages early (5 days) after wounding, and reduced the scarring at 30 days, when compared to a stiff, Tegaderm treated control. Importantly, hydrogel stiffness alone is not responsible for inflammatory activation; instead, stiffness modulates the cellular responses to biochemical inflammatory agonists. In the context of a wound, it is likely that physical properties of biomaterials will act in concert with the milieu of cytokines present in the wound bed. Nonetheless, given the ease of procuring fibrin, and the beneficial effects on the immune response, this material remains an auspicious candidate for wound healing applications.

Hyaluronic acid (HA): HA is a major glycosaminoglycan component of the ECM, and another biocompatible and degradable material that has been explored for wound applications[182]. HA can be derived from animal tissues or produced enzymatically or through bacterial expression systems[183]. As a polysaccharide, it is highly hydrophilic, absorbing water and swelling, and thus provides hydration for the wound environment. HA is thought to promote wound healing by inhibiting bacterial growth and promoting re-epithelialization and dermal regeneration. For example, HA hydrogel promotes diabetic wound healing in mice when compared to non-treated wounds and this effect can be further augmented by immunomodulating agents. Furthermore, HA-containing topical gauze pads were found to improve the healing rate and reduce pain in patients with venous leg ulcers compared to plain gauze pads.

A deeper understanding of HA-mediated immunomodulatory effects can be gleaned from natural wound healing processes. Upon wounding, the release of reactive oxygen species and degradative enzymes cause HA fragmentation, and thus the breakdown of high molecular weight HA (HMW-HA) to low molecular weight HA (LMW-HA), which promotes inflammation. Inflammatory activation also causes upregulation of CD44, which binds to HA and enhances recruitment of various immune cells including neutrophils, monocytes, and T cells. CD44-mediated uptake of HA by macrophages clears HA fragments and initiates inflammation resolution, which is followed by restoration of HMW-HA during tissue repair. Culture of macrophages on LMW-HA induces pro-inflammatory activation including expression of iNOS, TNF, and IL-12, whereas HMW-HA induces anti-inflammatory and pro-resolving activation including expression of ARG1, IL-10, and CD206[184]. Consistent with this, a recent study

demonstrated that the addition of HMW-HA to a 3D collagen matrix induced expression of pro-healing macrophage markers including CD163, IL-10 and CCL-22, while decreasing inflammatory markers TNF, IL-6 and IL-1. Given the multi-functional role of HA on macrophage activation, it is possible that strategic engineering of this molecule into biomaterial scaffolds can elicit dynamic activation and inactivation of both inflammatory and pro-resolving immune phenotypes.

A wide variety of synthetic polymers have been used as biomaterials, including poly (α-hydroxy) esters such as polycaprolactone (PCL), polyglycolic acid (PGA), polylactic acid (PLA), and their copolymer poly(glycolic acid) (PLGA); poly(ethers) containing poly(ethylene oxide) (PEO) and poly(ethylene glycol) (PEG), polyvinyl alcohol (PVA), polyurethane (PU), among others[185] (Figure 5-2). In the context of immunomodulation for wound healing, a major advantage of synthetic polymers is that their chemical and physical properties can be precisely tuned. For example, polymer chemistry and processing will influence its glass transition temperature (Tg) and crystallinity, which will influence the ability of water to access the polymer chains and thus the rate of hydrolytic degradation[186,187]. Porosity can also be engineered to provide void space for cell infiltration or release of drugs or biological molecules. Approaches to introduce porosity include the use of porogens, solvent casting and particulate leaching, lyophilization, or freezing (cryogels)[188,189]. Injectability is another critical factor for tissue regeneration, delivered as a pre-gel solution that molds precisely to fill complex defects before gelling in situ[190,191]. In situ gelation can be achieved by designing a reaction between biomaterials and the solvent, salt concentration, pH, or temperature[192].

Another challenge for biomaterials includes insufficient mechanical strength and flexibility to cope with the movements of the human body. Self-healing hydrogels provide increased flexibility to accommodate changes in the mechanical environment. For example, chitosan-g-polyaniline (QCSP) with benzaldehyde functionalized poly(ethylene glycol)-co-poly(glycerol sebacate) (PEGS-FA) was developed as a healing biomaterial[193]. This polymer system crosslinks at 37 °C and, thus, is injectable but solidifies in the body. A QCSP-PEGS-FA-based wound dressing led to a higher expression of wound healing markers (EGF, TGF-β, and VEGF) compared to a commercial wound dressing in a mouse skin wound model[193]. In another example, polydopamine was investigated for its adhesiveness to native tissues, excellent biocompatibility, and the ability to endow hydrogels with self-healing properties due to their highly reactive catechol groups[194]. The combination of dopamine-modified four-armed PEG with phenylboronic acid-functionalized four-armed PEG could yield an injectable hydrogel with good adhesion to skin tissue and rapid self-healing to withstand strain. Similarly, when polydopamine nanoparticles were incorporated into a poly (N-isopropyl acrylamide) network, wound healing was accelerated[195].

Combinations of synthetic polymers and natural biomaterials exploit the intrinsic biocompatibility of natural biomaterials while simultaneously taking advantage of the physicochemical properties of synthetic biomaterials[196]. Furthermore, incorporating specific biological building blocks allows targeting of the immune responses by incorporating chemical moieties that elicit a desired immunologic effect[116,197]. For example, fibrin supports bioactivity, including natural cell adhesion and anti-inflammatory properties[181], while PEG can provide hydrogel structure and desirable physical properties. Taking advantage of both of these features,

PEG-fibrinogen gels have been successfully investigated in vitro and in vivo wound healing models[198–200]. Similarly, incorporating PEG into HA-based materials leverages the immunosuppressive effects of HA, while increasing its stability[201,202]. Another approach that showed improved tissue regeneration included modifying synthetic PEG microspheres with heparin microislands (μIslands) to spatially isolate hydrogel microspheres[103]. The heparin μIslands provided stores for natural heparin binding growth factors and chemokines within the microsphere-based hydrogels. This biomaterial improved diabetic wound healing compared to two clinically relevant control groups, Oasis and Aquaphor, while properly polarizing macrophages to a pro-regenerative M2 over pro-inflammatory M1 phenotype. Thus, combining synthetic with natural materials may be a means to enhance tissue integration and augment the regenerative potential of biomaterials.

Biomaterials for wound healing have traditionally aimed to accelerate wound closure, minimize infection, and replace lost tissue. While biomaterials have not been extensively studied in the context of regeneration, there are a few reports of biomaterial-induced regeneration. An earlier study used a dextran-based hydrogel combined with a synthetic material, polyethylene glycol diacrylate (PEGDA), to treat burn wounds in a mouse model. Compared to a commercially available skin substitute, Integra, the dextran hydrogel elicited more significant infiltration of neutrophils and macrophages at day five post wounding and was almost completely degraded by day seven. Additionally, improved angiogenesis was observed along with increased infiltration of endothelial progenitor cells and blood flow. By five weeks after wounding, the dextran hydrogel promoted mature epithelial structures with an increased number of hair follicles and sebaceous glands, which were not observed in the Integra-treated control.

This study suggests that biomaterials that influence the dynamics of the immune response and enhance angiogenesis may be important for inducing a regenerative response.

Fully synthetic biomaterials have also shown regenerative potential in the skin. A recent approach to elicit skin regeneration built upon PEG microparticle-based microporous annealed particle (MAP) hydrogels (Figure 5-3). These flowable microparticles can be applied or injected directly to an injury site and annealed in situ via enzyme-mediated annealing of adjacent peptides forming a three-dimensional porous scaffold that mimics the porosity of skin ECM[10]. By modifying the chirality of the annealing peptides from the natural L- to D-conformation within the MAP hydrogel (D-MAP), an adaptive immune response was elicited that resulted in the formation of new hair follicles and sebaceous glands within the healed tissue in a murine small wound model[11]. Healing in this model without D-MAP otherwise results in scar formation. The hair follicle neogenesis required an intact adaptive immune system and was associated with antigen specific immune responses and enhanced recruitment and retention of IL-33+ macrophages within hydrogel scaffolds. This was absent in mice that lacked T and B lymphocytes, suggesting that adaptive immunity is critical for the biomaterial-induced regeneration. While the exact signals are unknown, identifying the pro-regenerative immune to stromal cell pathways will allow the development of novel immunomodulatory and pro-regenerative biomaterials.

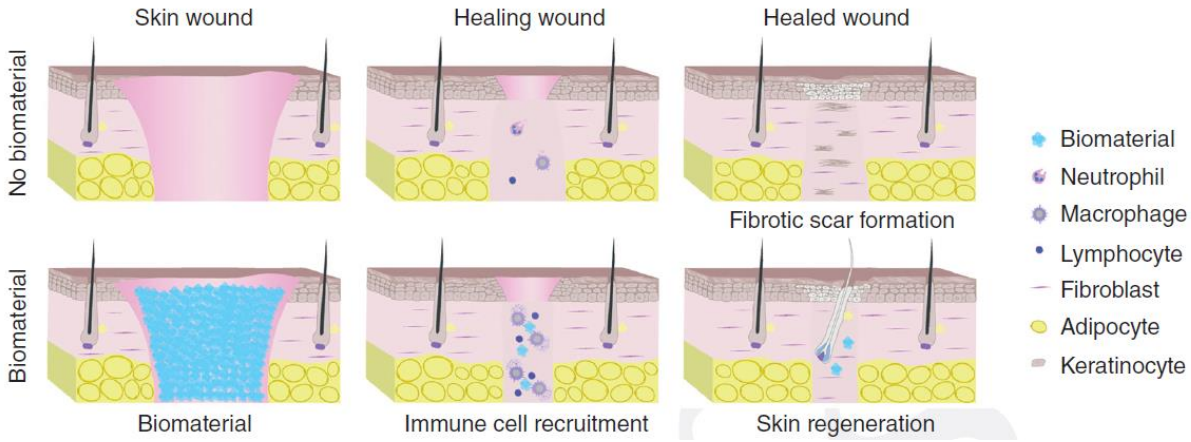

Figure 5-3 Biomaterials for skin regeneration.
Wounding of skin typically leads to scarring (top), but treatment with biomaterials such as microporous annealed particle (MAP) hydrogels that elicit immune cell activation leads to hair follicle regeneration (bottom).

Decellularized matrix materials have been shown to induce tissue regeneration, although in a muscle wound model and not yet in skin[203]. Decellularized materials are derived from allogeneic or xenogeneic tissues, which are treated with detergents to remove cells, and can be solubilized and reconstructed into ECM-based hydrogels[204]. These materials have been widely used clinically as wound dressing, including human cadaver-based Alloderm and dCELL, porcine-based Oasis and Permacol, and reconstructed ECMs. Many of these dressings have been found to decrease inflammation and expedite healing of wounds compared to standard of care controls. When applied to a murine muscle wound, a porcine urinary bladder matrix elicited a better regenerative response compared to synthetic PEG hydrogels that result in fibrous capsules. Of note, the synthetic hydrogels were bulk hydrogels that lacked porosity or biologic cues (i.e. integrin binding peptides) that can simulate natural ECM. The improved response to the matrix material was attributed to reduced myeloid infiltration and increased type-2 immune response, characterized by CD206-expressing macrophages and Th2-associated gene expression (e.g IL-4,

IL-13, Arg1). Importantly, the ECM scaffold pro-regenerative response, which is characterized by IL-4 macrophage polarization, depends on the mTOR/Rictor-dependent Th2 pathway. The presence of ECM breakdown products also shapes an antigen-presenting phenotype that suppresses inflammation. While commercially available acellular dermal substitutes are widely available, their ability to facilitate skin wound regeneration has not yet been demonstrated. Therefore, next generation immunomodulatory ECM-based biomaterials that can tune endogenous immune cells to facilitate regeneration will likely be needed to induce hair neogenesis and complete skin regeneration.

Despite early promise, cellular-based therapies have largely been unable to alter disease outcomes in regenerative medicine applications. Introducing cells with engineered biomaterials has fared better with modest improvement in wound healing outcomes in specific chronic wound conditions, but also with tremendous cost. While most approaches for skin wound healing have utilized fibroblast and keratinocytes to replenish damaged resident cells, as well as endothelial cells to enhance angiogenesis, delivery of immune cells or progenitor cells has shown promise for immunomodulation. Studies have shown that delivery of monocytes or anti-fibrotic Trem2+ macrophages via pullalan-collagen composite hydrogels could directly skew the immune response toward accelerated wound healing. Interestingly, when monocytes were delivered, they differentiated into macrophages thereby increasing the number of functional macrophage populations, which showed a mix of pro-inflammatory and pro-repair transcriptomic profiles, similar to the Trem2+ macrophages that were directly delivered.

Stem or progenitor cells have the proliferative capacity to expand within tissues, the ability to differentiate into many different cell types, and also broad immunomodulatory effects. These cells secrete cytokines, chemokines, growth factors, and hormones, including prostaglandins and IL-10, and lack major histocompatibility complex class II (MHC-II) and co-stimulatory molecules, leading to immunosuppressive and pro-healing effects. In one example of a biomaterial-based delivery system, in situ formed PEG-gelatin hydrogel significantly improved retention of adipose-derived stem cells, and enhanced angiogenesis and wound closure in a murine wound healing model. In another example, an injectable hydrogel was synthesized via the interaction between hyper-branched multi-acrylated PEG macromers and thiolated HA to deliver stem cells. The functionality of implanted cells within a tissue can be enhanced by microporous injectable synthetic scaffolds or implanted void forming hydrogels. These studies showed that microscale void spaces enhance retention or delivery of desired cells that have the potential to directly modify immune response intensity and/or polarization directly within a wound site. For instance, adipose tissue-derived progenitor cells injected in mice before skin transplantation prolonged transplant survival and was associated with an expansion of CD4+ Tregs, IL-10 production, and suppression of Th17 responses. Whether local delivery of these or other immunomodulatory cell populations from biomaterial scaffolds can further augment the immunomodulatory effects of delivered cells and whether the cells delivered via a pro-regenerative scaffold can alter wound fate from a scarring outcome to tissue regeneration requires further investigation.

In addition to providing physical scaffolding for attachment and proliferation of cells within the wound microenvironment, biomaterials can also serve as a delivery vehicle for

biologics and/or small molecule therapeutics, including molecules to boost the healing process, decrease inflammation, release anti-fibrotic, and/or prevent infection. Encapsulation within a material offers the ability to control release and maintain long-term functionality in vivo. For example, HA-hydrogel embedded with the anti-inflammatory drug paeoniflorin encouraged macrophage anti-inflammatory/pro-healing responses and improved diabetic wound healing in mice. Interestingly, the HA component alone showed a pro-healing effect, but when combined with the drug, synergized to achieve an even more significant effect. In another recent study, gelatin hydrogel supplemented with the anti-inflammatory and biosurfactant Surfactin A was shown to improve the healing in diabetic rat wounds by increasing CD31 angiogenic marker and skewing macrophage polarization by lowering the ratio of inflammatory to repair markers (iNOS/CD206) relative to control (Yan et al. 2021). Antibodies targeted against inflammatory cytokines to dampen inflammation have also shown positive effects, for example neutralizing antibodies against IL-1 and TNF-α. Importantly, conjugating an anti-TNF-α antibody to HA scaffold in treating rat burn model showed improved anti-inflammatory effect when compared to direct administration of non-conjugated antibodies, suggesting that the biomaterial was able to offer sustained local modulation whereas soluble delivery could not. Another strategy to enhance regenerative healing is the delivery of resolution of inflammation mediators. A recent example utilized dual delivery of IL-10 and the pro-resolving lipid mediator, resolving D1, along with PEG hydrogels containing RGD domains. Using a dorsal skinfold window chamber, the researchers were able to demonstrate enhanced immune cell recruitment to sites of injury and polarization of myeloid cells toward reparative activation that enhanced angiogenesis. Whether such delivery approaches can be used to further promote skin regeneration remains to be determined.

5.1.3. Concluding remarks and future perspectives

As sentinels against pathogens and regulators of healing, the immune system plays an undeniable role in repair and regeneration of injured skin. Engineering biomaterial wound dressings that target immune cells, and their activities, will be critical for the development of new strategies for wound healing to enhance regeneration (Figure. 5-4). Since successful tissue healing requires dynamic immune responses, with proper timing and duration of inflammatory and healing activities, temporal regulation of immunomodulatory agents will be critical. Moreover, smart responsive materials will enable sensing of the wound environment and release drugs in response to changes in the tissue. One recent example is a wound dressing that senses wound oxygen levels and releases vascular endothelial growth factor (VEGF) to enhance angiogenesis in response to low oxygen. Responsive materials that controllably release immunomodulatory agents in response to the immune status of the wound will be of great future interest. Advances in material fabrication technologies such as 3D printing may enable better control of material geometry provided by various biomaterials to enable delivery of multicellular microstructures, to provide precise placement of niches for regeneration of hair follicles, sweat glands, or adipose tissue to better promote regeneration of complex skin structures. These tools can also be adapted to include biological agents to promote healing.

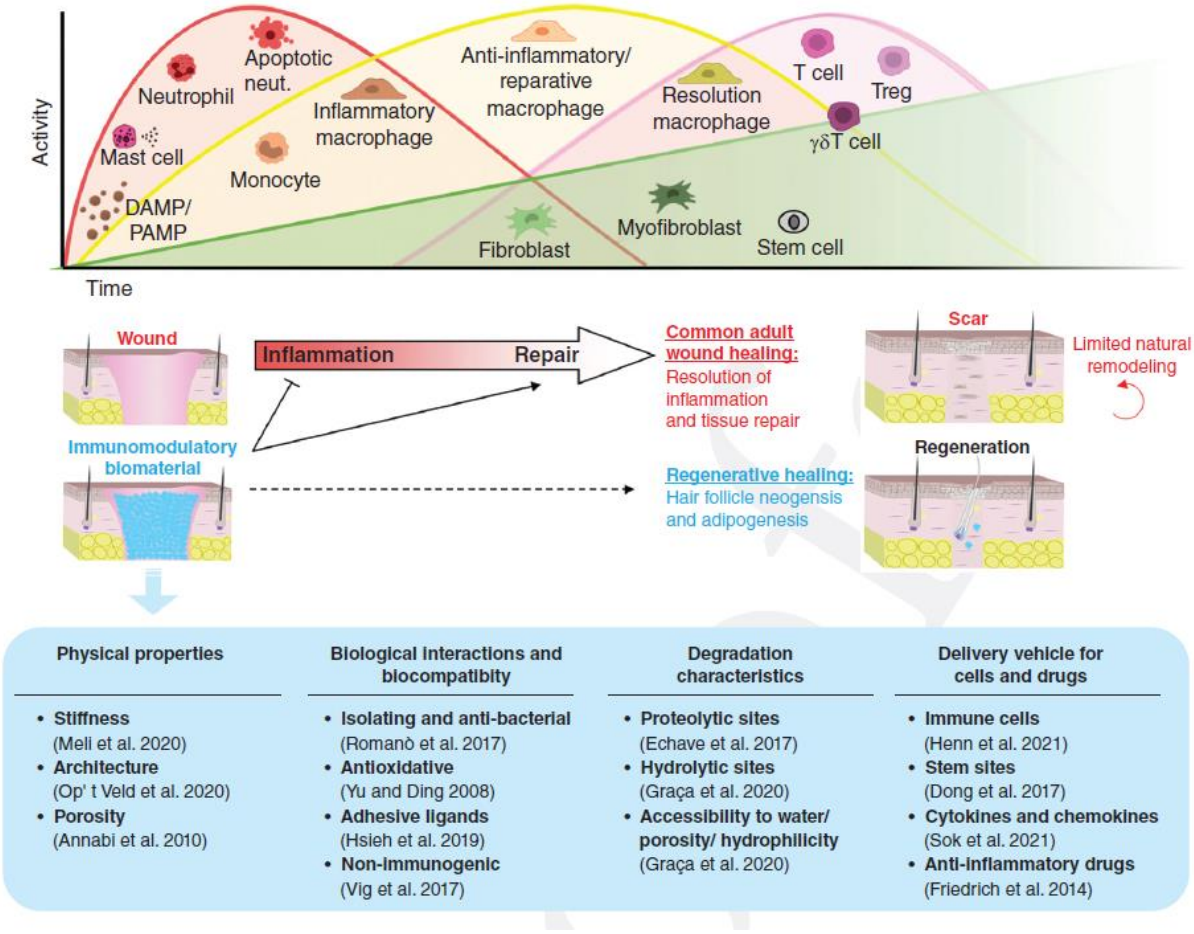

Figure 5-4 Engineering biomaterials to enhance skin regenerative wound healing.
(A) Key immune and repair cells in wound healing. Wounding initiates inflammation with the release of danger signals, mast cell degranulation, and influx of neutrophils and monocyte-derived inflammatory macrophages. Inflammation is resolved following apoptosis of neutrophils, their clearance by macrophages, and macrophage conversion into anti-inflammatory and reparative activation. T cells are also recruited and skew toward anti-inflammatory activation with time. Macrophages promote angiogenesis and a fibroproliferative process, but the reparative activity must be limited for wound resolution and regeneration of functional tissue. Macrophage and T-cell activities are essential for regenerative repair mechanisms including hair neogenesis. (B) Biomaterial properties that modulate wound inflammation and repair. Biomaterials contain biophysical and biochemical properties that modulate the immune response and may be leveraged to encourage regeneration. Biomaterial compatibility is key to avoiding inflammatory response with excess recruitment and activation of immune cells and instead, enhancing the resolution of inflammation and repair process. Biomaterial permeability and degradability facilitate the infiltration of host cells to promote reepithelialization, angiogenesis, and ECM deposition in a timely fashion to skew fibrosis toward the regeneration of functional skin.

Most immunomodulatory biomaterials have been evaluated in the context of duration and strength of inflammatory phase of wound healing, re-epithelialization and angiogenesis, or regulation of fibroblast activation to deposit new ECM while avoiding hyper-fibrosis. Regenerative events including the formation of hair follicles and fat glands are often not considered, even though they are hallmarks of functional tissue. Ultimately, a better understanding of the molecular players involved in immunomodulation during healing and regeneration will enable new approaches to target these molecules using biomaterials, to heal wounds faster, with less scar and more regeneration. Small molecules or gene editing agents delivered via biomaterials can be used to specifically activate or silence molecules that are involved in healing. For example, fibrin microspheres were used to deliver Rab18 and eNOS encoding plasmids and enhanced wound closure by reducing inflammation and increasing angiogenesis. In addition, HA/gelatin-based delivery of miR-223 miRNA enhanced wound closure by driving macrophage polarization toward anti-inflammatory and pro-regenerative profile. Moreover, genetically engineered animals can be used to produce naturally derived biomaterials with new and unique properties. Matrices derived from animals lacking thrombospondin-2 were softer and contained thinner fibrils, and when applied to diabetic wounds, led to enhanced healing compared to controls. The specific effects of this matrix on the immune response during healing have yet to be elucidated. Nonetheless, biomaterials-based approaches to modulate immune responses will become more powerful as the mechanisms underlying regeneration are elucidated.

5.2. Pathway of D-MAP gel for complete wound regeneration

Given those immunomodulatory biomaterial development history, we hypothesize that engineered MAP gels elicit specific immune signals to activate pro-regenerative Mφ directly or indirectly and induce fibroblast plasticity to transform normally fibrotic healing into a desirable regenerative response. In this interdisciplinary grant, spanning biomaterial science, immunology and skin biology, we will establish mechanisms for biomaterial-based wound regeneration:

Aim 1. Establish the role of Mφ and the molecular signals from immunomodulatory MAP gels required for wound regeneration in mice.

MAPs cross-linked with antigenic D-enantiomeric peptides (D-MAP)[11] and photo-annealed MAPs (new data) trigger HF regeneration in wounds. We hypothesize that direct or indirect activation of regenerative Mφ populations imparts wound regeneration by immunomodulatory MAPs. We will establish the role of Mφ populations and the molecular mechanisms employed using (a) single-cell RNAsequencing (scRNA-seq)[205,206], flow cytometry and multiplexed immunofluorescent analysis; (b) genetic and non-genetic cell depletion, and (c) small molecule inhibitors in wounds treated with D-MAP or photo-annealed MAP gels. Established regeneration readout – quantification of new HFs per wound on whole mount histology[205] will objectively determine the relative roles of Mφ subpopulations in MAP-triggered regeneration.

Aim 2. Optimize MAP gel formulations for enhanced Mφ signaling for wound regeneration.

We already know that two immunomodulatory MAP formulations can elicit hair regeneration in wounds: D-MAP and photo-annealed MAP gel. We hypothesize that we can further enhance MAP-induced wound regeneration by altering their specific material properties to directly

engage regenerative Mφ populations. We will: (a) Engineer new MAPs with optimized: (i) gel stiffness, (ii) integrin binding, (iii) annealing mechanism for regenerative Mφ in-growth and prevention of fibrotic signaling. (b) Test gene expression and phenotypic markers of cultured Mφ +/- T-cells to these MAP formulations in a high-throughput in vitro assay format. (c) Test three optimized MAP formulations predicted to maximize HF regeneration in small and large wound models in vivo.

Aim 3. Determine how MAP gel-induced immune signals enhance wound fibroblast plasticity. Our recent studies reveal expansion of plastic Crabp1+ fibroblasts is required to regenerate new HFs in skin wounds by giving rise to new hair-specific mesenchymal cells[206,207] and putative immune-to-fibroblasts signaling networks are enriched in naturally regenerating vs. fibrotic large skin wounds[205]. We hypothesize that specific MAP-triggered immune signals drive wound fibroblasts to acquire a regenerative Crabp1+ plastic state. To test this, we will use our established approach to: (a) perform scRNA-seq on the most regenerative MAP formulation identified in Aim 2, (b) infer immune-to-fibroblast signaling, (c) build gene regulatory network (GRN) models from scRNA-seq data of MAP-treated regenerating small wounds, and (d) Experimentally delete or overexpress candidate receptor genes used by fibroblasts to respond to the putative ligands produced by Mφ to confirm their roles in (i) small wounds and (ii) large wounds treated with optimized vs. control MAP formulations. Overall, our studies: (i) will fill critical knowledge gaps on the immune-driven mechanism of regenerative wound healing; and (ii) will drive the development of next-generation immunomodulating wound biomaterials.

Reference

1. Engler, A. J., Sen, S., Sweeney, H. L. & Discher, D. E. Matrix elasticity directs stem cell lineage specification. *Cell* **126**, 677–689 (2006).
2. Reilly, G. C. & Engler, A. J. Intrinsic extracellular matrix properties regulate stem cell differentiation. *J. Biomech.* **43**, 55–62 (2010).
3. Briquez, P. S., Clegg, L. E., Martino, M. M., Gabhann, F. M. & Hubbell, J. A. Design principles for therapeutic angiogenic materials. *Nat. Rev. Mater.* **1**, (2016).
4. Dawson, J. I., Kanczler, J. M., Yang, X. B., Attard, G. S. & Oreffo, R. O. C. Clay gels for the delivery of regenerative microenvironments. *Adv. Mater.* **23**, 3304–3308 (2011).
5. Nih, L. R., Gojgini, S., Carmichael, S. T. & Segura, T. Dual-function injectable angiogenic biomaterial for the repair of brain tissue following stroke. *Nat. Mater.* **17**, 642–651 (2018).
6. Hofer, A. M. & Brown, E. M. Extracellular calcium sensing and signalling. *Nat. Rev. Mol. Cell Biol.* **4**, 530–538 (2003).
7. Wang, C., Lin, K., Chang, J. & Sun, J. Osteogenesis and angiogenesis induced by porous β-CaSiO(3)/PDLGA composite scaffold via activation of AMPK/ERK1/2 and PI3K/Akt pathways. *Biomaterials* **34**, 64–77 (2013).
8. Wang, Y., Yu, X., Baker, C., Murphy, W. L. & McDevitt, T. C. Mineral particles modulate osteo-chondrogenic differentiation of embryonic stem cell aggregates. *Acta Biomater.* **29**, 42–51 (2016).
9. Highley, C. B., Song, K. H., Daly, A. C. & Burdick, J. A. Jammed microgel inks for 3D printing applications. *Adv. Sci. (Weinh.)* **6**, 1801076 (2019).

10. Griffin, D. R., Weaver, W. M., Scumpia, P. O., Di Carlo, D. & Segura, T. Accelerated wound healing by injectable microporous gel scaffolds assembled from annealed building blocks. *Nat. Mater.* **14**, 737–744 (2015).
11. Griffin, D. R. *et al.* Activating an adaptive immune response from a hydrogel scaffold imparts regenerative wound healing. *Nat. Mater.* **20**, 560–569 (2021).
12. Koh, J. *et al.* Enhanced In Vivo Delivery of Stem Cells using Microporous Annealed Particle Scaffolds. *Small* **15**, e1903147 (2019).
13. Cotero, V. *et al.* Noninvasive sub-organ ultrasound stimulation for targeted neuromodulation. *Nat. Commun.* **10**, 952 (2019).
14. Tay, A., Sohrabi, A., Poole, K., Seidlits, S. & Di Carlo, D. A 3D Magnetic Hyaluronic Acid Hydrogel for Magnetomechanical Neuromodulation of Primary Dorsal Root Ganglion Neurons. *Adv. Mater.* e1800927 (2018) doi:10.1002/adma.201800927.
15. Cotero, V. *et al.* Peripheral Focused Ultrasound Neuromodulation (pFUS). *J. Neurosci. Methods* **341**, 108721 (2020).
16. Pavlov, V. A. & Tracey, K. J. The vagus nerve and the inflammatory reflex--linking immunity and metabolism. *Nat. Rev. Endocrinol.* **8**, 743–754 (2012).
17. Tracey, K. J. Reflex control of immunity. *Nat. Rev. Immunol.* **9**, 418–428 (2009).
18. O'Hare, J. D. & Zsombok, A. Brain-liver connections: role of the preautonomic PVN neurons. *Am. J. Physiol. Endocrinol. Metab.* **310**, E183-9 (2016).
19. Roh, E., Song, D. K. & Kim, M.-S. Emerging role of the brain in the homeostatic regulation of energy and glucose metabolism. *Exp. Mol. Med.* **48**, e216 (2016).
20. Pocai, A., Obici, S., Schwartz, G. J. & Rossetti, L. A brain-liver circuit regulates glucose homeostasis. *Cell Metab.* **1**, 53–61 (2005).

21. Chakravarthy, K., Nava, A., Christo, P. J. & Williams, K. Review of recent advances in peripheral nerve stimulation (PNS). *Curr. Pain Headache Rep.* **20**, 60 (2016).
22. Patil, A. C. & Thakor, N. V. Implantable neurotechnologies: a review of micro- and nanoelectrodes for neural recording. *Med. Biol. Eng. Comput.* **54**, 23–44 (2016).
23. Cogan, S. F. Neural stimulation and recording electrodes. *Annu. Rev. Biomed. Eng.* **10**, 275–309 (2008).
24. Shemesh, O. A. *et al.* Temporally precise single-cell-resolution optogenetics. *Nat. Neurosci.* **20**, 1796–1806 (2017).
25. Deisseroth, K. Optogenetics: 10 years of microbial opsins in neuroscience. *Nat. Neurosci.* **18**, 1213–1225 (2015).
26. Olofsson, P. S. & Tracey, K. J. Bioelectronic medicine: technology targeting molecular mechanisms for therapy. *J. Intern. Med.* **282**, 3–4 (2017).
27. Birmingham, K. *et al.* Bioelectronic medicines: a research roadmap. *Nat. Rev. Drug Discov.* **13**, 399–400 (2014).
28. Ng, K. A., Greenwald, E., Xu, Y. P. & Thakor, N. V. Implantable neurotechnologies: a review of integrated circuit neural amplifiers. *Med. Biol. Eng. Comput.* **54**, 45–62 (2016).
29. Koopman, F. A. *et al.* Vagus nerve stimulation inhibits cytokine production and attenuates disease severity in rheumatoid arthritis. *Proc. Natl. Acad. Sci. U. S. A.* **113**, 8284–8289 (2016).
30. Wang, H. *et al.* Nicotinic acetylcholine receptor alpha7 subunit is an essential regulator of inflammation. *Nature* **421**, 384–388 (2003).

31. Yi, C.-X., la Fleur, S. E., Fliers, E. & Kalsbeek, A. The role of the autonomic nervous liver innervation in the control of energy metabolism. *Biochim. Biophys. Acta* **1802**, 416–431 (2010).
32. Stauss, H., Meyers, E., Glab, T. & Rahmouni, K. Modulation of blood glucose concentration by vagal nerve stimulation. *FASEB J.* **29**, (2015).
33. Karnani, M. & Burdakov, D. Multiple hypothalamic circuits sense and regulate glucose levels. *Am. J. Physiol. Regul. Integr. Comp. Physiol.* **300**, R47-55 (2011).
34. Routh, V. H., Hao, L., Santiago, A. M., Sheng, Z. & Zhou, C. Hypothalamic glucose sensing: making ends meet. *Front. Syst. Neurosci.* **8**, 236 (2014).
35. Marty, N., Dallaporta, M. & Thorens, B. Brain glucose sensing, counterregulation, and energy homeostasis. *Physiology (Bethesda)* **22**, 241–251 (2007).
36. Tracey, K. J. Reflexes in immunity. *Cell* vol. 164 343–344 (2016).
37. Zachs, D. P. *et al.* Noninvasive ultrasound stimulation of the spleen to treat inflammatory arthritis. *Nat. Commun.* **10**, 951 (2019).
38. Gigliotti, J. C. *et al.* Ultrasound prevents renal ischemia-reperfusion injury by stimulating the splenic cholinergic anti-inflammatory pathway. *J. Am. Soc. Nephrol.* **24**, 1451–1460 (2013).
39. Wright, C. J., Rothwell, J. & Saffari, N. Ultrasonic stimulation of peripheral nervous tissue: an investigation into mechanisms. *J. Phys. Conf. Ser.* **581**, 012003 (2015).
40. Colucci, V., Strichartz, G., Jolesz, F., Vykhodtseva, N. & Hynynen, K. Focused ultrasound effects on nerve action potential in vitro. *Ultrasound Med. Biol.* **35**, 1737–1747 (2009).

41. Juan, E. J., González, R., Albors, G., Ward, M. P. & Irazoqui, P. Vagus nerve modulation using focused pulsed ultrasound: Potential applications and preliminary observations in a rat. *Int. J. Imaging Syst. Technol.* **24**, 67–71 (2014).
42. Wright, C. J., Haqshenas, S. R., Rothwell, J. & Saffari, N. Unmyelinated peripheral nerves can be stimulated in vitro using pulsed ultrasound. *Ultrasound Med. Biol.* **43**, 2269–2283 (2017).
43. Tyler, W. J. *et al.* Remote excitation of neuronal circuits using low-intensity, low-frequency ultrasound. *PLoS One* **3**, e3511 (2008).
44. Tufail, Y., Yoshihiro, A., Pati, S., Li, M. M. & Tyler, W. J. Ultrasonic neuromodulation by brain stimulation with transcranial ultrasound. *Nat. Protoc.* **6**, 1453–1470 (2011).
45. Tracey, K. J. The inflammatory reflex. *Nature* **420**, 853–859 (2002).
46. Suarez Castellanos, I., Jeremic, A., Cohen, J. & Zderic, V. Ultrasound stimulation of insulin release from pancreatic beta cells as a potential novel treatment for type 2 diabetes. *Ultrasound Med. Biol.* **43**, 1210–1222 (2017).
47. Sandoval, D. & Sisley, S. R. Brain GLP-1 and insulin sensitivity. *Mol. Cell. Endocrinol.* **418 Pt 1**, 27–32 (2015).
48. Murray, K. & Reardon, C. The cholinergic anti-inflammatory pathway revisited. *Neurogastroenterol. Motil.* **30**, (2018).
49. Torres, A. J., Hill, A. S. & Love, J. C. Nanowell-based immunoassays for measuring single-cell secretion: characterization of transport and surface binding. *Anal. Chem.* **86**, 11562–11569 (2014).

50. Cotero, V. E., Zhang, B. B. & Routh, V. H. The response of glucose-excited neurones in the ventromedial hypothalamus to decreased glucose is enhanced in a murine model of type 2 diabetes mellitus. *J. Neuroendocrinol.* **22**, 65–74 (2010).
51. Cotero, V. E. & Routh, V. H. Insulin blunts the response of glucose-excited neurons in the ventrolateral-ventromedial hypothalamic nucleus to decreased glucose. *Am. J. Physiol. Endocrinol. Metab.* **296**, E1101-9 (2009).
52. Seoane-Collazo, P. *et al.* Hypothalamic-autonomic control of energy homeostasis. *Endocrine* **50**, 276–291 (2015).
53. Röder, P. V., Wu, B., Liu, Y. & Han, W. Pancreatic regulation of glucose homeostasis. *Exp. Mol. Med.* **48**, e219 (2016).
54. Li, S. & Chen, J. D. Z. Pulse width-dependent effects of intestinal electrical stimulation for obesity: Role of gastrointestinal motility and hormones. *Obes. Surg.* **27**, 70–77 (2017).
55. Hevener, A. L., Bergman, R. N. & Donovan, C. M. Novel glucosensor for hypoglycemic detection localized to the portal vein. *Diabetes* **46**, 1521–1525 (1997).
56. Chaudhry, S., Bernardes, M., Harris, P. E. & Maffei, A. Gastrointestinal dopamine as an anti-incretin and its possible role in bypass surgery as therapy for type 2 diabetes with associated obesity. *Minerva Endocrinol.* **41**, 43–56 (2016).
57. Puleo, C. & Cotero, V. Noninvasive Neuromodulation of Peripheral Nerve Pathways Using Ultrasound and Its Current Therapeutic Implications. *Cold Spring Harb. Perspect. Med.* **10**, (2020).
58. Cotero, V. *et al.* Peripheral Focused Ultrasound Stimulation (pFUS): New Competitor in Pharmaceutical Markets? *SLAS technology* vol. 24 448–452 (2019).

59. Huerta, T. S. *et al.* Targeted peripheral focused ultrasound stimulation attenuates obesity-induced metabolic and inflammatory dysfunctions. *Sci. Rep.* **11**, 5083 (2021).

60. Akhtar, K. *et al.* Non-invasive peripheral focused ultrasound neuromodulation of the celiac plexus ameliorates symptoms in a rat model of inflammatory bowel disease. *Exp. Physiol.* **106**, 1038–1060 (2021).

61. de Rutte, J. M., Koh, J. & Di Carlo, D. Scalable high‐throughput production of modular microgels for in situ assembly of microporous tissue scaffolds. *Adv. Funct. Mater.* **29**, 1900071 (2019).

62. Moparthi, L. & Zygmunt, P. M. Human TRPA1 is an inherently mechanosensitive bilayer-gated ion channel. *bioRxiv* (2020) doi:10.1101/2020.03.05.979252.

63. Bae, C., Sachs, F. & Gottlieb, P. A. The mechanosensitive ion channel Piezo1 is inhibited by the peptide GsMTx4. *Biochemistry* **50**, 6295–6300 (2011).

64. Motter, A. L. & Ahern, G. P. TRPA1 is a polyunsaturated fatty acid sensor in mammals. *PLoS One* **7**, e38439 (2012).

65. Kong, X. *et al.* Roux-en-Y gastric bypass enhances insulin secretion in type 2 diabetes via FXR-mediated TRPA1 expression. *Mol. Metab.* **29**, 1–11 (2019).

66. Derbenev, A. V. & Zsombok, A. Potential therapeutic value of TRPV1 and TRPA1 in diabetes mellitus and obesity. *Semin. Immunopathol.* **38**, 397–406 (2016).

67. Li, M. *et al.* Transient receptor potential V channels are essential for glucose sensing by aldolase and AMPK. *Cell Metab.* **30**, 508-524.e12 (2019).

68. Zsombok, A. & Derbenev, A. V. TRP channels as therapeutic targets in diabetes and obesity. *Pharmaceuticals (Basel)* **9**, 50 (2016).

69. Ahn, J., Lee, H., Im, S. W., Jung, C. H. & Ha, T. Y. Allyl isothiocyanate ameliorates insulin resistance through the regulation of mitochondrial function. *J. Nutr. Biochem.* **25**, 1026–1034 (2014).

70. Lee, E. *et al.* Transient receptor potential vanilloid type-1 channel regulates diet-induced obesity, insulin resistance, and leptin resistance. *FASEB J.* **29**, 3182–3192 (2015).

71. Ruckwardt, T. J., Morabito, K. M. & Graham, B. S. Immunological Lessons from Respiratory Syncytial Virus Vaccine Development. *Immunity* **51**, 429–442 (2019).

72. Conis, E. *Vaccine Nation*. (University of Chicago Press, 2021). doi:10.7208/9780226923772.

73. Saleh, A., Qamar, S., Tekin, A., Singh, R. & Kashyap, R. Vaccine Development Throughout History. *Cureus* **13**, e16635 (2021).

74. Kim, H., Webster, R. G. & Webby, R. J. Influenza Virus: Dealing with a Drifting and Shifting Pathogen. *Viral Immunol.* **31**, 174–183 (2018).

75. Harding, A. T. & Heaton, N. S. Efforts to Improve the Seasonal Influenza Vaccine. *Vaccines (Basel)* **6**, (2018).

76. Subbarao, K., Murphy, B. R. & Fauci, A. S. Development of effective vaccines against pandemic influenza. *Immunity* **24**, 5–9 (2006).

77. Song, J. Y. *et al.* Long-term immunogenicity of influenza vaccine among the elderly: Risk factors for poor immune response and persistence. *Vaccine* **28**, 3929–3935 (2010).

78. Young, B. *et al.* Do antibody responses to the influenza vaccine persist year-round in the elderly? A systematic review and meta-analysis. *Vaccine* **35**, 212–221 (2017).

79. Young, B., Sadarangani, S., Jiang, L., Wilder-Smith, A. & Chen, M. I.-C. Duration of Influenza Vaccine Effectiveness: A Systematic Review, Meta-analysis, and Meta-regression of Test-Negative Design Case-Control Studies. *J. Infect. Dis.* **217**, 731–741 (2018).

80. Ma, C. S., Deenick, E. K., Batten, M. & Tangye, S. G. The origins, function, and regulation of T follicular helper cells. *J. Exp. Med.* **209**, 1241–1253 (2012).

81. Krishnaswamy, J. K. *et al.* Migratory CD11b+ conventional dendritic cells induce T follicular helper cell-dependent antibody responses. *Sci Immunol* **2**, (2017).

82. Choi, Y. S. *et al.* ICOS receptor instructs T follicular helper cell versus effector cell differentiation via induction of the transcriptional repressor Bcl6. *Immunity* **34**, 932–946 (2011).

83. Franchi, L. & Núñez, G. The Nlrp3 inflammasome is critical for aluminium hydroxide-mediated IL-1beta secretion but dispensable for adjuvant activity. *Eur. J. Immunol.* **38**, 2085–2089 (2008).

84. Li, H., Willingham, S. B., Ting, J. P.-Y. & Re, F. Cutting edge: inflammasome activation by alum and alum's adjuvant effect are mediated by NLRP3. *J. Immunol.* **181**, 17–21 (2008).

85. Zhu, G., Yang, Y.-G. & Sun, T. Engineering optimal vaccination strategies: effects of physical properties of the delivery system on functions. *Biomater Sci* (2022) doi:10.1039/d2bm00011c.

86. Hem, S. L. & Hogenesch, H. Relationship between physical and chemical properties of aluminum-containing adjuvants and immunopotentiation. *Expert Rev. Vaccines* **6**, 685–698 (2007).

87. Bastola, R. & Lee, S. Physicochemical properties of particulate vaccine adjuvants: their pivotal role in modulating immune responses. *Int. J. Pharm. Investig.* **49**, 279–285 (2019).

88. Gray, L. T. *et al.* Generation of potent cellular and humoral immunity against SARS-CoV-2 antigens via conjugation to a polymeric glyco-adjuvant. *Biomaterials* **278**, 121159 (2021).

89. Silva, M. *et al.* A particulate saponin/TLR agonist vaccine adjuvant alters lymph flow and modulates adaptive immunity. *Sci. Immunol.* **6**, eabf1152 (2021).

90. Dane, E. L. *et al.* STING agonist delivery by tumour-penetrating PEG-lipid nanodiscs primes robust anticancer immunity. *Nat. Mater.* **21**, 710–720 (2022).

91. Ishii-Mizuno, Y. *et al.* Improved sustained release of antigen from immunostimulatory DNA hydrogel by electrostatic interaction with chitosan. *Int. J. Pharm.* **516**, 392–400 (2017).

92. Xi, X. *et al.* Self-healing microcapsules synergetically modulate immunization microenvironments for potent cancer vaccination. *Sci Adv* **6**, eaay7735 (2020).

93. Bobbala, S., Gibson, B., Gamble, A. B., McDowell, A. & Hook, S. Poloxamer 407-chitosan grafted thermoresponsive hydrogels achieve synchronous and sustained release of antigen and adjuvant from single-shot vaccines. *Immunology and Cell Biology* vol. 96 656–665 (2018).

94. Tam, H. H. *et al.* Sustained antigen availability during germinal center initiation enhances antibody responses to vaccination. *Proc. Natl. Acad. Sci. U. S. A.* **113**, E6639–E6648 (2016).

95. Atcha, H. *et al.* Mechanically activated ion channel Piezo1 modulates macrophage polarization and stiffness sensing. *Nature Communications* vol. 12 (2021).

96. Meli, V. S. *et al.* YAP-mediated mechanotransduction tunes the macrophage inflammatory response. *Sci Adv* **6**, (2020).

97. Abaricia, J. O. *et al.* Control of innate immune response by biomaterial surface topography, energy, and stiffness. *Acta Biomaterialia* vol. 133 58–73 (2021).

98. La Russa, F. *et al.* Disruption of the Sensory System Affects Sterile Cutaneous Inflammation In Vivo. *J. Invest. Dermatol.* **139**, 1936-1945.e3 (2019).

99. Grover, C. N. *et al.* Crosslinking and composition influence the surface properties, mechanical stiffness and cell reactivity of collagen-based films. *Acta Biomater.* **8**, 3080–3090 (2012).

100. Super, M. *et al.* Biomaterial vaccines capturing pathogen-associated molecular patterns protect against bacterial infections and septic shock. *Nat Biomed Eng* **6**, 8–18 (2022).

101. Langellotto, F. *et al.* A modular biomaterial scaffold-based vaccine elicits durable adaptive immunity to subunit SARS-CoV-2 antigens. *Adv. Healthc. Mater.* **10**, e2101370 (2021).

102. Tsoras, A. N., Wong, K. M., Paravastu, A. K. & Champion, J. A. Rational Design of Antigen Incorporation Into Subunit Vaccine Biomaterials Can Enhance Antigen-Specific Immune Responses. *Front. Immunol.* **11**, 1547 (2020).

103. Pruett, L. J., Jenkins, C. H., Singh, N. S., Catallo, K. J. & Griffin, D. R. Heparin Microislands in Microporous Annealed Particle Scaffolds for Accelerated Diabetic Wound Healing (Adv. Funct. Mater. 35/2021). *Advanced Functional Materials* vol. 31 2170259 (2021).

104. Veiseh, O. *et al.* Size- and shape-dependent foreign body immune response to materials implanted in rodents and non-human primates. *Nat. Mater.* **14**, 643–651 (2015).

105. Moore, E. M. *et al.* Biomaterials direct functional B cell response in a material-specific manner. *Sci. Adv.* **7**, eabj5830 (2021).

106. Weiss, U. & Rajewsky, K. The repertoire of somatic antibody mutants accumulating in the memory compartment after primary immunization is restricted through affinity maturation and mirrors that expressed in the secondary response. *J. Exp. Med.* **172**, 1681–1689 (1990).

107. Vidarsson, G., Dekkers, G. & Rispens, T. IgG subclasses and allotypes: from structure to effector functions. *Front. Immunol.* **5**, 520 (2014).

108. Jacob, J., Przylepa, J., Miller, C. & Kelsoe, G. In situ studies of the primary immune response to (4-hydroxy-3-nitrophenyl)acetyl. III. The kinetics of V region mutation and selection in germinal center B cells. *J. Exp. Med.* **178**, 1293–1307 (1993).

109. Arulanandam, B. P., Mittler, J. N., Lee, W. T., O'Toole, M. & Metzger, D. W. Neonatal administration of IL-12 enhances the protective efficacy of antiviral vaccines. *J. Immunol.* **164**, 3698–3704 (2000).

110. Huber, V. C. *et al.* Distinct contributions of vaccine-induced immunoglobulin G1 (IgG1) and IgG2a antibodies to protective immunity against influenza. *Clin. Vaccine Immunol.* **13**, 981–990 (2006).

111. Mozdzanowska, K., Furchner, M., Washko, G., Mozdzanowski, J. & Gerhard, W. A pulmonary influenza virus infection in SCID mice can be cured by treatment with hemagglutinin-specific antibodies that display very low virus-neutralizing activity in vitro. *J. Virol.* **71**, 4347–4355 (1997).

112. Pati, R., Shevtsov, M. & Sonawane, A. Nanoparticle vaccines against infectious diseases. *Front. Immunol.* **9**, 2224 (2018).

113. Navarro-Tovar, G., Palestino, G. & Rosales-Mendoza, S. An overview on the role of silica-based materials in vaccine development. *Expert Rev. Vaccines* **15**, 1449–1462 (2016).

114. Oliveira, C. L. P. *et al.* The development of new oral vaccines using porous silica. *J. Phys. Condens. Matter* **34**, (2022).

115. Moral, M. E. G. & Siahaan, T. J. Conjugates of cell adhesion peptides for therapeutics and diagnostics against cancer and autoimmune diseases. *Curr. Top. Med. Chem.* **17**, 3425–3443 (2017).

116. Rostam, H. M. *et al.* Immune-instructive polymers control macrophage phenotype and modulate the foreign body response in vivo. *Matter* **2**, 1564–1581 (2020).

117. Khaing, Z. Z. & Seidlits, S. K. Hyaluronic acid and neural stem cells: implications for biomaterial design. *J. Mater. Chem. B Mater. Biol. Med.* **3**, 7850–7866 (2015).

118. Khaing, Z. Z. *et al.* High molecular weight hyaluronic acid limits astrocyte activation and scar formation after spinal cord injury. *J. Neural Eng.* **8**, 046033 (2011).

119. Ehsanipour, A. *et al.* Injectable, Hyaluronic Acid-Based Scaffolds with Macroporous Architecture for Gene Delivery. *Cell. Mol. Bioeng.* **12**, 399–413 (2019).

120. Ehsanipour, A. *et al.* Injectable, macroporous scaffolds for delivery of therapeutic genes to the injured spinal cord. *APL Bioeng.* **5**, 016104 (2021).

121. Jensen, G., Holloway, J. L. & Stabenfeldt, S. E. Hyaluronic acid biomaterials for central nervous system regenerative medicine. *Cells* **9**, (2020).

122. Avenoso, A. *et al.* Hyaluronan fragmentation during inflammatory pathologies: A signal that empowers tissue damage. *Mini Rev. Med. Chem.* **20**, 54–65 (2020).

123. Ashammakhi, N. *et al.* Regenerative therapies for spinal cord injury. *Tissue Eng. Part B Rev.* **25**, 471–491 (2019).

124. Pakulska, M. M., Ballios, B. G. & Shoichet, M. S. Injectable hydrogels for central nervous system therapy. *Biomed. Mater.* **7**, 024101 (2012).

125. Lu, J. *et al.* Enhanced angiogenesis by the hyaluronic acid hydrogels immobilized with a VEGF mimetic peptide in a traumatic brain injury model in rats. *Regen. Biomater.* **6**, 325–334 (2019).

126. Wen, Y. *et al.* Spinal cord injury repair by implantation of structured hyaluronic acid scaffold with PLGA microspheres in the rat. *Cell Tissue Res.* **364**, 17–28 (2016).

127. Rocha, L. A., Sousa, R. A., Learmonth, D. A. & Salgado, A. J. The role of biomaterials as angiogenic modulators of spinal cord injury: Mimetics of the spinal cord, cell and angiogenic factor delivery agents. *Front. Pharmacol.* **9**, (2018).

128. Haggerty, A. E., Maldonado-Lasunción, I. & Oudega, M. Biomaterials for revascularization and immunomodulation after spinal cord injury. *Biomed. Mater.* **13**, 044105 (2018).

129. Yao, C., Cao, X. & Yu, B. Revascularization after traumatic spinal cord injury. *Front. Physiol.* **12**, (2021).

130. Haggerty, A. E., Maldonado-Lasunción, I. & Oudega, M. Biomaterials for revascularization and immunomodulation after spinal cord injury. *Biomedical Materials* **13**, (2018).

131. Graumann, U., Ritz, M.-F. & Hausmann, O. Necessity for Re-Vascularization after Spinal Cord Injury and the Search for Potential Therapeutic Options. *Current Neurovascular Research* **8**, 334–341 (2011).

132. Pardue, E. L., Ibrahim, S. & Ramamurthi, A. Role of hyaluronan in angiogenesis and its utility to angiogenic tissue engineering. *Organogenesis* **4**, 203 (2008).

133. Qazi, T. H. *et al.* Extrusion Printed Scaffolds with Varying Pore Size As Modulators of MSC Angiogenic Paracrine Effects. *ACS Biomaterials Science and Engineering* **5**, 5348–5358 (2019).

134. Oliviero, O., Ventre, M. & Netti, P. A. Functional porous hydrogels to study angiogenesis under the effect of controlled release of vascular endothelial growth factor. *Acta Biomaterialia* **8**, 3294–3301 (2012).

135. Litwiniuk, M., Krejner, A. & Grzela, T. Hyaluronic Acid in Inflammation and Tissue Regeneration. (2016).

136. Mo, W. *et al.* The influence of hyaluronic acid on vascular endothelial cell proliferation and the relationship with ezrin/merlin expression. *Acta Biochimica et Biophysica Sinica* **43**, 930–939 (2011).

137. Ibrahim, S. & Ramamurthi, A. Hyaluronic acid cues for functional endothelialization of vascular constructs. *Journal of Tissue Engineering and Regenerative Medicine* **2**, 22–32 (2008).

138. Yang, C. *et al.* The high and low molecular weight forms of hyaluronan have distinct effects on CD44 clustering. *Journal of Biological Chemistry* **287**, 43094–43107 (2012).

139. Ooki, T., Murata-Kamiya, N., Takahashi-Kanemitsu, A., Wu, W. & Hatakeyama, M. High-Molecular-Weight Hyaluronan Is a Hippo Pathway Ligand Directing Cell Density-Dependent Growth Inhibition via PAR1b. *Developmental Cell* **49**, 590-604.e9 (2019).

140. Wu, S. C. *et al.* Hyaluronan size alters chondrogenesis of adipose-derived stem cells via the CD44/ERK/SOX-9 pathway. *Acta Biomaterialia* **66**, 224–237 (2018).

141. Sindrilaru, A. *et al.* An unrestrained proinflammatory M1 macrophage population induced by iron impairs wound healing in humans and mice. *J. Clin. Invest.* **121**, 985–997 (2011).

142. Landén, N. X., Li, D. & Ståhle, M. Transition from inflammation to proliferation: a critical step during wound healing. *Cell. Mol. Life Sci.* **73**, 3861–3885 (2016).

143. Özkale, B., Sakar, M. S. & Mooney, D. J. Active biomaterials for mechanobiology. *Biomaterials* **267**, 120497 (2021).

144. Sun, G. *et al.* Dextran hydrogel scaffolds enhance angiogenic responses and promote complete skin regeneration during burn wound healing. *Proc. Natl. Acad. Sci. U. S. A.* **108**, 20976–20981 (2011).

145. Kobayashi, T., Naik, S. & Nagao, K. Choreographing immunity in the skin epithelial barrier. *Immunity* **50**, 552–565 (2019).

146. Komi, D. E. A., Khomtchouk, K. & Santa Maria, P. L. A review of the contribution of mast cells in wound healing: Involved molecular and cellular mechanisms. *Clin. Rev. Allergy Immunol.* **58**, 298–312 (2020).

147. Filep, J. G. & Ariel, A. Neutrophil heterogeneity and fate in inflamed tissues: implications for the resolution of inflammation. *Am. J. Physiol. Cell Physiol.* **319**, C510–C532 (2020).

148. Mirza, R., DiPietro, L. A. & Koh, T. J. Selective and specific macrophage ablation is detrimental to wound healing in mice. *Am. J. Pathol.* **175**, 2454–2462 (2009).

149. Lucas, T. *et al.* Differential roles of macrophages in diverse phases of skin repair. *J. Immunol.* **184**, 3964–3977 (2010).

150. deCathelineau, A. M. & Henson, P. M. The final step in programmed cell death: phagocytes carry apoptotic cells to the grave. *Essays Biochem.* **39**, 105–117 (2003).

151. Doran, A. C., Yurdagul, A., Jr & Tabas, I. Efferocytosis in health and disease. *Nat. Rev. Immunol.* **20**, 254–267 (2020).

152. Butenko, S. *et al.* Corrigendum: Transcriptomic analysis of monocyte-derived non-phagocytic macrophages favors a role in limiting tissue repair and fibrosis. *Front. Immunol.* **11**, 1003 (2020).

153. Wynn, T. A. & Vannella, K. M. Macrophages in tissue repair, regeneration, and fibrosis. *Immunity* **44**, 450–462 (2016).

154. Lech, M. & Anders, H.-J. Macrophages and fibrosis: How resident and infiltrating mononuclear phagocytes orchestrate all phases of tissue injury and repair. *Biochim. Biophys. Acta* **1832**, 989–997 (2013).

155. Wynn, T. A. & Ramalingam, T. R. Mechanisms of fibrosis: therapeutic translation for fibrotic disease. *Nat. Med.* **18**, 1028–1040 (2012).

156. Kania, G., Rudnik, M. & Distler, O. Involvement of the myeloid cell compartment in fibrogenesis and systemic sclerosis. *Nat. Rev. Rheumatol.* **15**, 288–302 (2019).

157. Singampalli, K. L. *et al.* The role of an IL-10/hyaluronan axis in dermal wound healing. *Front. Cell Dev. Biol.* **8**, 636 (2020).

158. Nguyen, J. K., Austin, E., Huang, A., Mamalis, A. & Jagdeo, J. The IL-4/IL-13 axis in skin fibrosis and scarring: mechanistic concepts and therapeutic targets. *Arch. Derm. Res.* **312**, 81–92 (2020).

159. Liu, G. *et al.* Phenotypic and functional switch of macrophages induced by regulatory CD4+CD25+ T cells in mice. *Immunol. Cell Biol.* **89**, 130–142 (2011).

160. Jameson, J. *et al.* A role for skin gammadelta T cells in wound repair. *Science* **296**, 747–749 (2002).

161. Kasuya, A., Ito, T. & Tokura, Y. M2 macrophages promote wound-induced hair neogenesis. *J. Dermatol. Sci.* (2018) doi:10.1016/j.jdermsci.2018.05.004.

162. Kim, D. *et al.* Noncoding dsRNA induces retinoic acid synthesis to stimulate hair follicle regeneration via TLR3. *Nat. Commun.* **10**, 2811 (2019).

163. Gay, D. *et al.* Fgf9 from dermal γδ T cells induces hair follicle neogenesis after wounding. *Nat. Med.* **19**, 916–923 (2013).

164. Abo, H. *et al.* Erythroid differentiation regulator-1 induced by microbiota in early life drives intestinal stem cell proliferation and regeneration. *Nat. Commun.* **11**, 513 (2020).

165. Wang, G. *et al.* Bacteria induce skin regeneration via IL-1β signaling. *Cell Host Microbe* **29**, 777-791.e6 (2021).

166. Seifert, A. W. *et al.* Skin shedding and tissue regeneration in African spiny mice (Acomys). *Nature* **489**, 561–565 (2012).

167. Brant, J. O., Yoon, J. H., Polvadore, T., Barbazuk, W. B. & Maden, M. Cellular events during scar-free skin regeneration in the spiny mouse, Acomys. *Wound Repair Regen.* **24**, 75–88 (2016).

168. Simkin, J., Gawriluk, T. R., Gensel, J. C. & Seifert, A. W. Macrophages are necessary for epimorphic regeneration in African spiny mice. *Elife* **6**, (2017).

169. Gaharwar, A. K., Singh, I. & Khademhosseini, A. Engineered biomaterials for in situ tissue regeneration. *Nat. Rev. Mater.* **5**, 686–705 (2020).

170. Shevchenko, R. V., James, S. L. & James, S. E. A review of tissue-engineered skin bioconstructs available for skin reconstruction. *J. R. Soc. Interface* **7**, 229–258 (2010).

171. Davison-Kotler, E., Marshall, W. S. & García-Gareta, E. Sources of collagen for biomaterials in skin wound healing. *Bioengineering (Basel)* **6**, 56 (2019).

172. Heemskerk, J. W. M., Kuijpers, M. J. E., Munnix, I. C. A. & Siljander, P. R. M. Platelet collagen receptors and coagulation. A characteristic platelet response as possible target for antithrombotic treatment. *Trends Cardiovasc. Med.* **15**, 86–92 (2005).

173. Echave, M. C., Saenz del Burgo, L., Pedraz, J. L. & Orive, G. Gelatin as biomaterial for tissue engineering. *Curr. Pharm. Des.* **23**, 3567–3584 (2017).

174. Witherel, C. E., Graney, P. L., Freytes, D. O., Weingarten, M. S. & Spiller, K. L. Response of human macrophages to wound matrices in vitro. *Wound Repair Regen.* **24**, 514–524 (2016).

175. El Masry, M. S. *et al.* Stabilized collagen matrix dressing improves wound macrophage function and epithelialization. *FASEB J.* **33**, 2144–2155 (2019).

176. Orgel, J. P. R. O., San Antonio, J. D. & Antipova, O. Molecular and structural mapping of collagen fibril interactions. *Connect. Tissue Res.* **52**, 2–17 (2011).

177. Lebbink, R. J. *et al.* Identification of multiple potent binding sites for human leukocyte associated Ig-like receptor LAIR on collagens II and III. *Matrix Biol.* **28**, 202–210 (2009).

178. Gailit, J. *et al.* Human fibroblasts bind directly to fibrinogen at RGD sites through integrin alpha(v)beta3. *Exp. Cell Res.* **232**, 118–126 (1997).

179. Spotnitz, W. D. Fibrin sealant: The only approved hemostat, sealant, and adhesive-a laboratory and clinical perspective. *ISRN Surg.* **2014**, 203943 (2014).

180. Heher, P., Mühleder, S., Mittermayr, R., Redl, H. & Slezak, P. Fibrin-based delivery strategies for acute and chronic wound healing. *Adv. Drug Deliv. Rev.* **129**, 134–147 (2018).

181. Hsieh, J. Y. *et al.* Differential regulation of macrophage inflammatory activation by fibrin and fibrinogen. *Acta Biomater.* **47**, 14–24 (2017).

182. Roberts, J. J., Elder, R. M., Neumann, A. J., Jayaraman, A. & Bryant, S. J. Interaction of hyaluronan binding peptides with glycosaminoglycans in poly(ethylene glycol) hydrogels. *Biomacromolecules* **15**, 1132–1141 (2014).

183. Sze, J. H., Brownlie, J. C. & Love, C. A. Biotechnological production of hyaluronic acid: a mini review. *3 Biotech* **6**, 67 (2016).

184. Rayahin, J. E., Buhrman, J. S., Zhang, Y., Koh, T. J. & Gemeinhart, R. A. High and low molecular weight hyaluronic acid differentially influence macrophage activation. *ACS Biomater. Sci. Eng.* **1**, 481–493 (2015).

185. Place, E. S., George, J. H., Williams, C. K. & Stevens, M. M. ChemInform abstract: Synthetic polymer scaffolds for tissue engineering. *ChemInform* **40**, (2009).

186. Young, R. J. & Chung, C. I. Introduction to polymers. *J. Eng. Mater. Technol.* **104**, 297–297 (1982).

187. Tsuji, H. Back cover: Macromol. Biosci. 7/2005. *Macromol. Biosci.* **5**, 680–680 (2005).

188. Annabi, N. *et al.* Controlling the porosity and microarchitecture of hydrogels for tissue engineering. *Tissue Eng. Part B Rev.* **16**, 371–383 (2010).

189. Woeller, C. F. *et al.* Evaluating a variable porosity wound dressing with anti-scar properties in a porcine model of wound healing. *Eplasty* **18**, e20 (2018).

190. Daly, A. C., Riley, L., Segura, T. & Burdick, J. A. Hydrogel microparticles for biomedical applications. *Nat. Rev. Mater.* **5**, 20–43 (2020).

191. Gao, Y., Li, Z., Huang, J., Zhao, M. & Wu, J. In situ formation of injectable hydrogels for chronic wound healing. *J. Mater. Chem. B Mater. Biol. Med.* **8**, 8768–8780 (2020).

192. Yu, L. & Ding, J. Injectable hydrogels as unique biomedical materials. *Chem. Soc. Rev.* **37**, 1473–1481 (2008).

193. Zhao, X. *et al.* Antibacterial anti-oxidant electroactive injectable hydrogel as self-healing wound dressing with hemostasis and adhesiveness for cutaneous wound healing. *Biomaterials* **122**, 34–47 (2017).

194. Huang, J. *et al.* An autonomous self-healing hydrogel with high polydopamine content for improved tensile strength. *J. Mater. Sci.* **55**, 17255–17265 (2020).

195. Han, L. *et al.* Polydopamine nanoparticles modulating stimuli-responsive PNIPAM hydrogels with cell/tissue adhesiveness. *ACS Appl. Mater. Interfaces* **8**, 29088–29100 (2016).

196. Aurand, E. R., Wagner, J. L., Shandas, R. & Bjugstad, K. B. Hydrogel formulation determines cell fate of fetal and adult neural progenitor cells. *Stem Cell Res.* **12**, 11–23 (2014).

197. Vishwakarma, A. *et al.* Engineering immunomodulatory biomaterials to tune the inflammatory response. *Trends Biotechnol.* **34**, 470–482 (2016).

198. Almany, L. & Seliktar, D. Biosynthetic hydrogel scaffolds made from fibrinogen and polyethylene glycol for 3D cell cultures. *Biomaterials* **26**, 2467–2477 (2005).

199. Fuoco, C. *et al.* Injectable polyethylene glycol-fibrinogen hydrogel adjuvant improves survival and differentiation of transplanted mesoangioblasts in acute and chronic skeletal-muscle degeneration. *Skelet. Muscle* **2**, 24 (2012).

200. Prüller, J., Mannhardt, I., Eschenhagen, T., Zammit, P. S. & Figeac, N. Satellite cells delivered in their niche efficiently generate functional myotubes in three-dimensional cell culture. *PLoS One* **13**, e0202574 (2018).

201. Mothe, A. J., Tam, R. Y., Zahir, T., Tator, C. H. & Shoichet, M. S. Repair of the injured spinal cord by transplantation of neural stem cells in a hyaluronan-based hydrogel. *Biomaterials* **34**, 3775–3783 (2013).

202. Wang, L. L. *et al.* Three-dimensional extrusion bioprinting of single- and double-network hydrogels containing dynamic covalent crosslinks. *J. Biomed. Mater. Res. A* **106**, 865–875 (2018).

203. Wolf, M. T. *et al.* A biologic scaffold-associated type 2 immune microenvironment inhibits tumor formation and synergizes with checkpoint immunotherapy. *Sci. Transl. Med.* **11**, (2019).

204. Urciuolo, F., Passariello, R., Imparato, G., Casale, C. & Netti, P. A. Bioengineered wound healing skin models: The role of immune response and endogenous ECM to fully replicate the dynamic of scar tissue formation in vitro. *Bioengineering (Basel)* **9**, 233 (2022).

205. Gay, D. *et al.* Phagocytosis of Wnt inhibitor SFRP4 by late wound macrophages drives chronic Wnt activity for fibrotic skin healing. *Sci. Adv.* **6**, eaay3704 (2020).

206. Guerrero-Juarez, C. F. *et al.* Single-cell analysis reveals fibroblast heterogeneity and myeloid-derived adipocyte progenitors in murine skin wounds. *Nat. Commun.* **10**, 650 (2019).

207. Abbasi, S. *et al.* Distinct regulatory programs control the latent regenerative potential of dermal fibroblasts during wound healing. *Cell Stem Cell* **28**, 581–583 (2021).